PhD-FSTC-2015-11
The Faculty of Sciences, Technology and Communication

DISSERTATION

Defense held on 11/03/2015 in Luxembourg

to obtain the degree of

DOCTEUR DE L'UNIVERSITÉ DU LUXEMBOURG

EN PHYSIQUE

by

Carlo Di Giambattista
Born on 28 January 1985 in Esch-sur-Alzette (Luxembourg)

Structural Relaxations in the Rotator Phase Of N-Eicosane

Dissertation defense committee

Dr. Tanja Schilling, Chairman
Professor, University of Luxembourg

Dr. Michael Wübbenhorst, Deputy Chairman
Professor, Katholieke Universiteit Leuven, Belgium

Dr. Roland Sanctuary, dissertation supervisor
Professor, University of Luxembourg

Dr. Rafael Jiménez Riobóo
Instituto de Ciencia de Materiales de Madrid, Spain

Dr. Jörg Baller
University of Luxembourg

The Thesis Committee for Carlo Di Giambattista
Certifies that this is the approved version of the following thesis:

Structural Relaxations in the Rotator Phase of n-Eicosane

APPROVED BY SUPERVISORS:

Supervisor:

Roland Sanctuary

Jörg Baller

Dedication

To my parents who taught me to follow my dreams and work properly.

To my teachers and professors which appeased my hunger for knowledge.

To the Luxembourgish people who allowed me to attend higher education through generous financial support.

To my wife who stands by my side and took care that I did not become too much of a slob.

Acknowledgements

I would like to express my gratitude to my supervisors Professor Dr. Roland Sanctuary and Dr. Jörg Baller. You have granted me the possibility to grow my scientific prowess and supported me all the way. Additionally I want to thank Professor Dr. Tanja Schilling for the insightful discussions and taking care of the organization of the joined research project. I would also like to thank Professor Michael Wübbenhorst, Dr Rafael Jiménez Riobóo for also serving as members of my PhD supervision committee. I would also like to thank my colleagues Professor Dr. Dr. h.c. Jan Kristian Krüger, Dr. Ulrich Müller, Dr. Èlio Périgo, Dr. Philipp Szary, Muhammad Anwar, Anna Dejmour, and Rick Dannert for the scientific discussions, Dr. Marlena Filimon for the "not so" scientific discussions, Robert Wagener, Vicente Reis-Adonis, Ernest Apel and Olga Astasheva for the technical support and last but not least Astrid Tobias and Fréderique Bertrand for administrative support. Additionally I want also thank Professor Antoine Kies, Professor Dr. Jan Lagerwall, Dr. Ralitsa Aleksandrova, Patrick Elens, Junghyun Noh, Catherine Reyes and Kevin Reguengo for the nice working environement. Finally I would like to thank the Fond National de la Recherche Luxembourg for funding the research project.

Abstract

Structural Relaxations in the Rotator Phase of n-Eicosane

Carlo Di Giambattista Dipl. Phys

The University of Luxembourg, 2015

Supervisor: Roland Sanctuary

We present relaxations of the heat capacity of the n-alkane n-eicosane ($C_{20}H_{42}$) in the metastable rotator phase. These relaxations are not connected to melting but rather to structural changes. A comparative study of the relaxation times with calorimetry in the time and frequency domain shows a slowing down of the dynamics on approaching the melting temperature of the rotator phase. Relaxation behaviour is also observed in the lattice structure by investigations with X-ray diffraction. It is shown that the angular position of the two most relevant X-ray lines relaxes on different time scales. One of these two relaxations can be related to the relaxations found in calorimetry. The relaxing behaviour is discussed in the framework of conformational defect formation and compared to known phenomena in literature.

Table of Contents

"Daß ich erkenne, was die Welt

im innersten zusammenhält"

Faust I, Johann Wolfgang von Goethe

I. Introduction

Since the first x-ray studies by Müller [1-3] in the first half of the 20th century, n-alkanes have remained in the focus of research until today [4]. Their rather simple setup of a carbon chain saturated with hydrogen (C_nH_{2n+2} , from now on referred to as Cn) makes them a model system for more complex systems like polymers [5] or lipids [6]. Depending conformational degrees of freedom they generate a multitude of stable and metastable crystalline structures [7].

Müller [2] observed the appearance of new types of phases, rotator phases, between the melt and the low temperature crystalline phase. The name rotator phase stems from an early concept which suggested that the molecules in the lattice structure have some rotational degrees of freedom [2]. Five different types of rotator phases (RI to RV) have been identified in the n-alkanes [7]. For n-alkanes with n<22, the RI phase adjoins the liquid phase [8,9]. For n≥22, the RII phase is observerd between the RI and the liquid phase. With rising carbon numbers n in the backbone, the number of different rotator phases (polymorphisms) increases [7,10,11]. With even higher carbon numbers n-alkanes approach the extended chain [12](orthorhombic, $n \gtrsim 43$) or folded chain[13] ($n \gtrsim 150$) structure of polyethylene. Strobl, Ewen et al. [14-16] used tritriacontane (C33) as an example to show how the various types of rotator phases are linked to different levels of conformational disorder. There are two kinds of conformational disorder which need to be addressed. First, disorder of molecules in the lattice structure can be induced by large oscillations of the whole molecule. As an example one can consider the 180° screw jump along one monomer length introduced by Andrew [17]. The second kind of disorder is the change in molecular chain conformation by gauche defects [18](here called defect because in the low temperature limit chains are in all trans configuration). Maroncelli et al. [19]showed that the gauche defects accumulate at the ends of the chains. Ryckaert et al. [20] confirmed these different types of conformational intra-chain defects by molecular dynamics (MD) simulations. Basson and Reynhardt [21] used NMR to identify jumps between chain configurations in the stable low temperature phase of several n-alkanes. They were able to relate these changes in configuration to a kink (gauche-trans-gauche-trans) formation at the end of the chain. This change between conformations is an activated process [21].

In summary, conformational disorder is a key feature of the crystalline phases of n-alkanes. In this work, the kinetics of defect formation as well as the phase transition behaviour from the rotator to the liquid phase is studied in detail on the example of eicosane (C20). One standard method to investigate phase transitions or more generally processes which exchange latent heat is calorimetry. Pak and Wunderlich [22] investigated the melting behaviour of n-alkanes with “Temperature Modulated Differential Scanning Calorimetry” (TMDSC). This experimental technique has the advantage that a separation of reversible and non-reversible behaviour close to a transition can be made [23,24]. Pak and Wunderlich [5] showed that close to the

melting transition, increased reversible heat flux could be observed. As the heat capacity in this region exceeds the value corresponding to skeletal motions of the molecule, it is referred to as apparent heat capacity [25]. Pak and Wunderlich argued that reversible melting and crystallization is occurring at the liquid/solid transition which is not driven by nucleation [5,22]. Furthermore they suggested that the reversible melting observed in polymers [24,26,27] corresponds to crystallisation without nucleation and melting of smaller polymer chains [5,28].

Eicosane exhibits a single metastable rotator phase (RI) which is only accessible upon cooling from the melt [29]. The structure is best described by a face centred orthorhombic (Fmmm) symmetry. In the RI phase the molecules are un-tilted relative to the *c*-axis, have a pseudo-hexagonal structure in the lateral direction (perpendicular to the *c*-axis) and assemble in a bilayer stacking sequence [30,31]. The structure is described as pseudo-hexagonal as in its limit (high temperatures), it is approaching the structure of the hexagonal RII phase found in other alkanes [32,33]. One very special feature of the RI phase is that the lattice parameters change considerably with temperature [2,30]. This special property of the RI phase of eicosane allows studying the kinetics of the rotator phase along with its transition to the liquid phase using time-resolved X-Ray diffraction. In combination with time-resolved calorimetry, these investigations allow to identify relaxation times of defect formation in the rotator phase as well as a clear separation between pre-melting and melting behaviour.

In this work we will present a comparative study of DSC, TMDSC and XRD investigations carried out on eicosane (C20) samples. The main objective is to characterize the relaxation behaviour of C20 in its rotator RI and triclinic phases for samples with two degrees of purity (99.0+% and 99.5+%). The TOPEM technique [34,35], a stochastically temperature modulated DSC technique, is employed to characterise the relaxing behaviour close to the transition to the liquid phase. Regular DSC measurement [36] as well as step-like experiments [37] are employed to check for the validity of the TOPEM measurements. XRD measurements with step-like temperature profiles show that the relaxation behaviour seen by DSC is also observable in the lattice structure in the rotator phase. These measurements also yield that in the temperature region where the apparent heat capacity increases (“melting range”) no coexistence of a metastable crystalline phase and liquid phase can be observed. The timescales of the relaxation (up to several minutes) give hints to the existence of cooperative processes in the rotator phase [38].

The structure of the present thesis is as follows: First, in chapter II, the theoretical background of the main experimental techniques (DSC,TOPEM,XRD) is established. Chapter III introduces the characteristics of the materials and describes the experimental setups. Additionally some general evaluations and data processing techniques are discussed. In chapter IV the main results are presented for the different experimental techniques. In chapter V we proceed to a synthesis of the different results. An interpretation is attempted with input from literature. The final

chapter VI summarizes the findings of this work and gives an outlook for further research.

II. Theory

II.1. Differential scanning calorimetry (DSC)

II.1.1. Instrument

Figure 1 shows a schematic representation of a disk type heat flux DSC. For this DSC the furnace temperature is controlled. The temperature difference between sample and reference is measured with a thermocouple. A cooling finger is attached to the furnace such that temperatures below room temperature are reachable. The furnace is flushed with an inert gas (like nitrogen) to avoid reaction or ice formation. This setup has a high sensitivity to measure the temperature difference but due to the limited contact to the crucibles and the size of the oven it has only a medium range in heating and cooling rates[36].

In figure 2 the disk type DSC is represented as equivalent heat conduction circuit. The resistances R correspond to thermal resistances. The capacitors C represent the heat capacities in the system. The current source ϕ_S corresponds to endo- or exothermic processes in the sample generating a heat flow. $\dot{Q}_\mu = \phi_\mu$ indicate the different heat flows in the system.

Zeroth approximation

The zeroth approximation corresponds to a simplified DSC system with the following properties:

- Steady state (constant heating or cooling rate β): $T(t) = T_0 + \beta t$
- no thermal resistance in the samples and crucibles $R_{MS} = R_{MR} = 0$
- thermal resistances to the crucibles are identical $R_{FMS} = R_{FMR} = R$

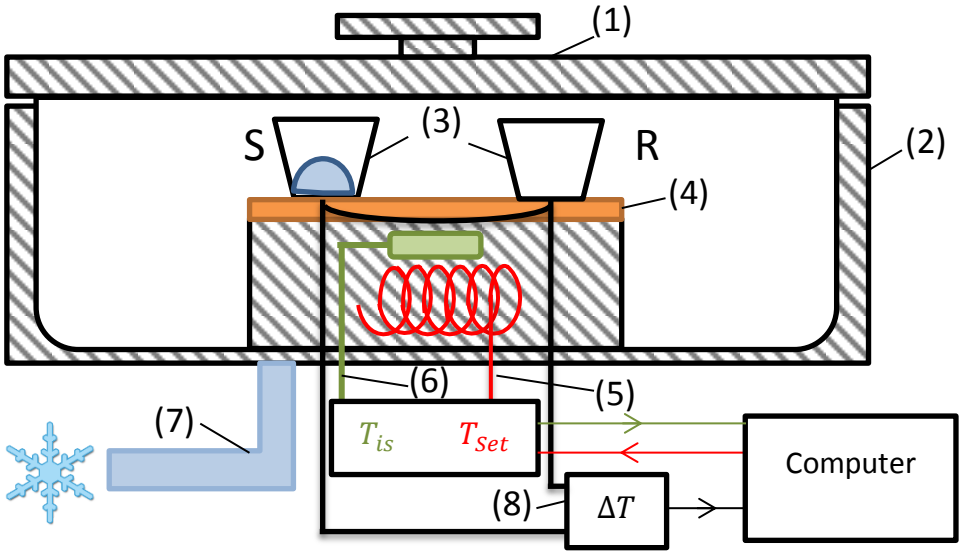

Figure 1: Sketch of a disc type heat flux DSC. (1) Lid; (2) Furnace; (3) Crucibles S: Sample R: Reference; (4) sensor disk; (5) Heater; (6) Temperature probe; (7) Cooling finger; (8) Thermocouple

- heat capacities related to the DSC negligible $C_{FMS} = C_{FMR} = 0$

- no heat flow between samples and reference: the thermal resistance of the disk is infinite $R_{MM} = \infty$
- no internal (latent) heat $\phi_S = 0$

For the steady state case the Biot-Fourier equation of the conduction of heat can be applied:

$$\frac{\phi}{A} = -\lambda \cdot \mathrm{grad}(T) \tag{II.1}$$

where ϕ/A is the heat flux density, A corresponds to the flow through area and λ the thermal conductivity. The Biot-Fourier law describes the flow of heat from a hot body to a cold one if they are in contact. With the assumption that the contact surface A of the crucibles are the same, the heat flow difference $\Delta\phi_{SR}$ between sample and reference is [36]:

$$\Delta\phi_{SR} = \dot{Q}_S - \dot{Q}_R = -\frac{A \cdot \lambda}{\Delta l}(T_S - T_R) = -K \cdot \Delta T_{M,st} \tag{II.2}$$

where is Δl is the distance between furnace and sample or reference with the thermal conductivity λ. $K = 1/R$is then the inverse thermal resistance. Resolving the circuit in figure 2 in this case yields for the steady state:

$$\Delta\phi_{SR} = \beta \cdot (C_S - C_R) = \beta \cdot \Delta C = -K \cdot \Delta T_{M,st} \tag{II.3}$$

where β is the heating or cooling rate.

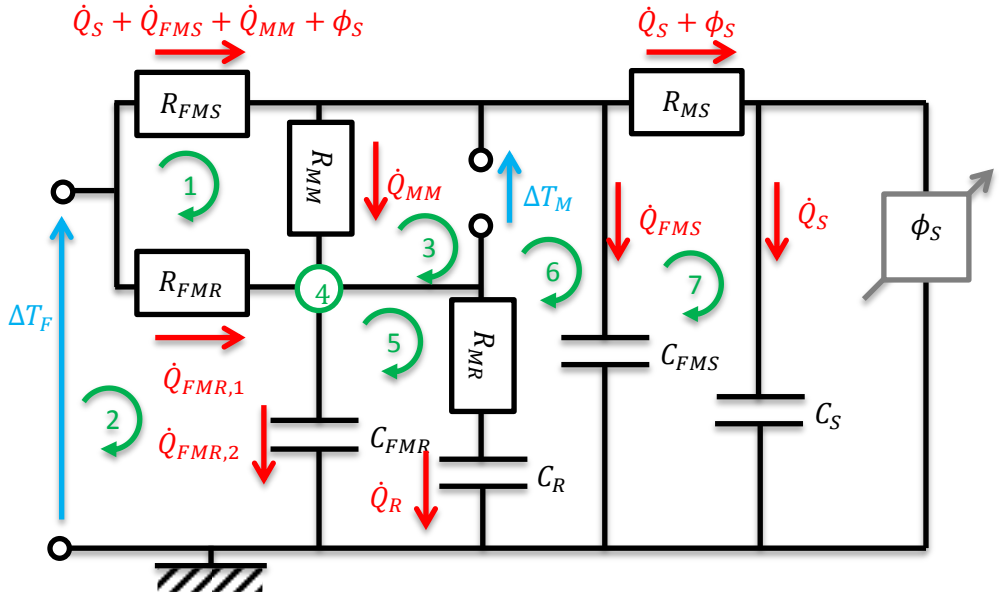

Figure 2: Model for disk type DSC. Quantities: ΔT_F variation of furnace temperature; ΔT_M measured temperature difference between measuring points; ϕ_S heat flow generated by the sample (latent heat); $\dot{Q}$ heat flow rates; R thermal resistances; C heat capacities. Indices: FMS from furnace to measuring point of the sample; MS from measuring point of the sample to sample; S sample itself; FMR from furnace to measuring point of the reference; MR from measuring point of the reference to reference, R reference itself, MM between measuring points of sample and reference.

1. The investigation of an unknown sample includes the following steps:Experiment with empty crucibles (on the reference and sample side) to assess intrinsic asymmetries of the DSC;
2. Experiment using a sample with known heat capacity and reference. After subtraction of data provided by step 1, the latter measurement allows for determining the proportionality factor *K* (which possibly is slightly temperature dependent)
3. Experiment with unknown sample and reference. C_S can be determined taking the asymmetry and proportionality factor *K* from the previous steps into account.

It is important to stress that in this type of measurement steady state conditions are achieved at times $t \gg C_S/K$ for the sample and at times $t \gg C_R/K$ on the reference side. The heat capacities of the sample and the reference should thus not be too different from each other (use of samples with small enough masses). Moreover one should note that not the temperature difference ΔT_M is measured but the voltage of the thermocouple. This nevertheless only brings another proportionality factor into play which is simultaneously calibrated with the thermal resistance.

First approximation

In the first approximation transient (non-steady- state) processes $\phi_S \neq 0$ (phase transitions) are added to the zeroth. Generally such transitions manifest themselves by peaks in the $\Delta T_M(t)$ curves (see figure 3). The heat flow difference is in this case[36]:

$$\phi_S(t) = -\frac{\Delta T_M(t)}{R} - \beta \cdot \Delta C - \frac{\tau}{R} \cdot \frac{\mathrm{d}\Delta T_M(t)}{\mathrm{d}t} \tag{II.4}$$

where *R* is the thermal resistance of both crucibles $R_{FMS} = R_{FMR} = R = 1/K$, $\Delta T_M(t)$ the non-steady measured temperature difference and the relaxation time $\tau = C_S \cdot R$. Simplified one can state that at a first order transition a sample crucible stays at the transition temperature T_{trans} while the reference crucible still adjust to the furnace temperature. Therefore the temperature difference between sample and reference $\Delta T_M(t)$ changes linearly with time as long the transition is ongoing:

$$\Delta T_M(t) = T_{trans} - T_R(t) \sim \beta \cdot t \tag{II.5}$$

Integration of $\phi_S(t)$ yields the latent heat for the transition:

$$\Delta H_{trans} = \int_{t_1}^{t_2} \phi_S(t)\,\mathrm{d}t \tag{II.6}$$

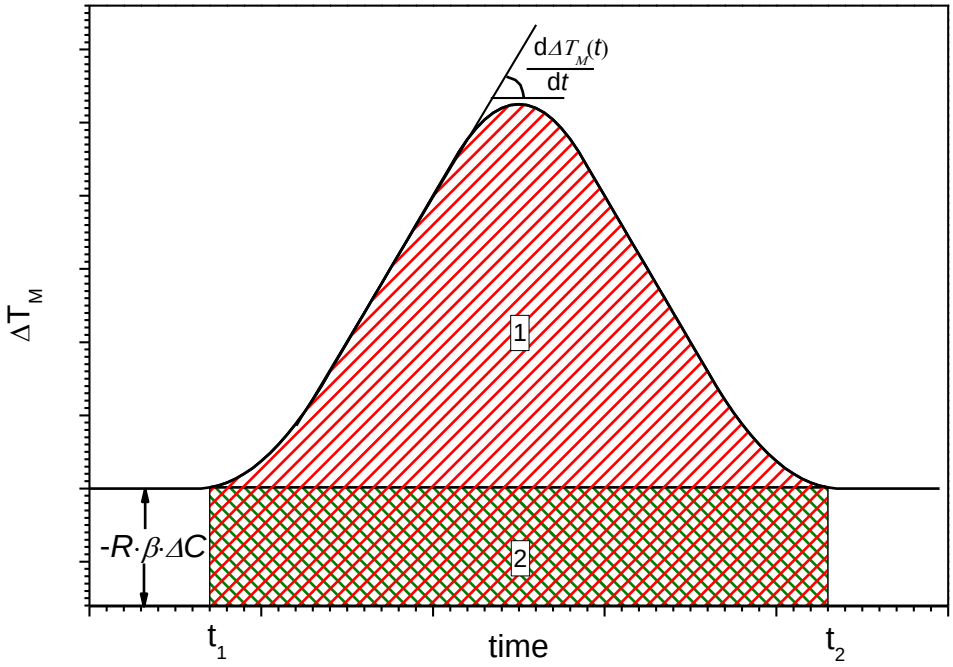

Figure 3: Schematic of a phase transition peak. Red shaded area corresponds to the latent heat related to the transition and a contribution by the heat capacity difference. Green shaded area corresponds to the difference of the heat which goes into the heat capacity of the sample and reference.

with equation (II.4) we find then:

$$=> \quad \Delta H_{trans} = -\frac{1}{R}\left[\underbrace{\int_{t_1}^{t_2} \Delta T_M(t)\,\mathrm{d}t}_{1} - \underbrace{\int_{t_1}^{t_2} (-R\cdot\Delta C\cdot\beta)\,\mathrm{d}t}_{2}\right] - \int_{t_1}^{t_2} \frac{\tau}{R}\cdot\frac{\mathrm{d}\Delta T_M(t)}{\mathrm{d}t}\,\mathrm{d}t \tag{II.7}$$

The first term corresponds to the whole area below the peak. The second term is the area which is dependent on the difference of the heat capacities of the sample and the reference. In case of a time-independent (temperature-independent) product $\tau = R\cdot\Delta C$ the third term in equation (II.7)becomes zero:

$$\int_{t_1}^{t_2} \frac{\mathrm{d}\Delta T_M(t)}{\mathrm{d}t}\,\mathrm{d}t = \Delta T_M(t_2) - \Delta T_M(t_1) = 0 \tag{II.8}$$

as long as t_1 and t_2 describe the limits of the transition peaks.

The difference between the first and second integral corresponds to the area below the peak subtracted by a baseline (line drawn between the curve values of the start end of the transition peak). This integration has the advantage that a measurement to correct for instrument asymmetry is not necessary. Furthermore if the heat

capacity of the sample is not constant during the transition, extrapolations from both side can be used to better assert the transition enthalpy. Similar as for the heat capacity enthalpy peaks can be used to calibrate the DSC with samples with well-defined transition enthalpies.

Higher order approximation

For the disk type DSC there is a finite thermal resistance $R_{MM} \neq \infty$ between the measuring points for the temperature difference between sample and reference. Additionally the disk itself has a heat capacity $C_{FMS} = C_{FMR} = C$. Finally sample and reference can have their own thermal resistances R_{MS} and R_{MR} respectively. Taking all these features into account (see figure 2) yields the following equation for the heat flow generated by the sample [36]:

$$\begin{aligned}\phi_S(t) = & -\left(\frac{1}{R}+\frac{2}{R_{MM}}\right)\Delta T_M(t) \\ & -\left[C + C_S\left(1 + R_{MS}\left(\frac{1}{R} + \frac{2}{R_{MM}}\right)\right)\right]\frac{\mathrm{d}\Delta T_M(t)}{\mathrm{d}t} \\ & - R_{MS}\cdot C\cdot C_S\frac{\mathrm{d}^2\Delta T_M(t)}{\mathrm{d}t^2} + (C_R - C_S)\frac{\mathrm{d}T_R(t)}{\mathrm{d}t} \\ & + C_S\cdot C_R(R_{MS} - R_{MR})\frac{\mathrm{d}^2 T_R(t)}{\mathrm{d}t^2}\end{aligned} \tag{II.9}$$

Taking into account the additional thermal resistances and heat capacities yields supplementary terms in $\frac{\mathrm{d}^2\Delta T_M(t)}{\mathrm{d}t^2}$ and $\frac{\mathrm{d}^2 T_R(t)}{\mathrm{d}t^2}$. In the steady-state case $\left(\phi_S(t) = 0;\ \frac{\mathrm{d}T_R(t)}{\mathrm{d}t} \approx \beta;\ \frac{\mathrm{d}\Delta T_M(t)}{\mathrm{d}t} = \frac{\mathrm{d}^2\Delta T_M(t)}{\mathrm{d}t^2} = 0\right)$ equation (II.9) reduces to:

$$\Delta T_{M.st} = -\frac{(C_S - C_R)}{\left(\frac{1}{R}+\frac{2}{R_{MM}}\right)}\beta \tag{II.10}$$

which corresponds to a slight modification of equation (II.3). Similar for the non-steady case with constant heating rate the integral of equation (II.9) becomes:

$$\begin{aligned}\Delta H_{trans} &= \int_{t_1}^{t_2}\phi_S(t)\,\mathrm{d}t \\ &= -\left(\frac{1}{R}+\frac{2}{R_{MM}}\right)\int_{t_1}^{t_2}(\Delta T_M - \Delta T_{M.st})\mathrm{d}t\end{aligned} \tag{II.11}$$

Again the integration limits t_1 and t_2 need to be in the steady state regime with $\Delta T_M(t_1) \approx \Delta T_M(t_2)$.

In the case where sample and reference have similar capacities ($C_S \approx C_R$) and thermal resistances ($R_{MS} \approx R_{MR}$) equation (II.9) can be represented by:

$$\phi_S(t) = -K\Delta T_M(t) - K_1\frac{\mathrm{d}\Delta T_M(t)}{\mathrm{d}t} - K_2\frac{\mathrm{d}^2\Delta T_M(t)}{\mathrm{d}t^2} \tag{II.12}$$

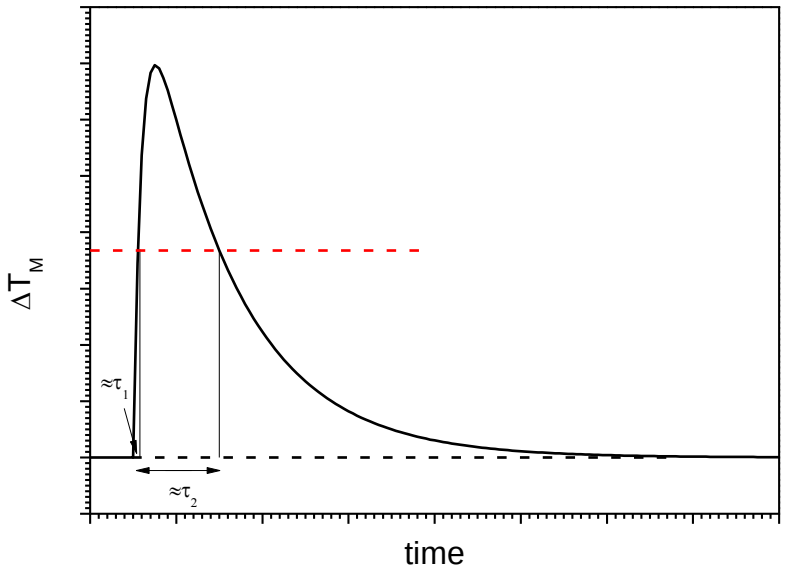

Figure 4: Sketch of the calorimeter's response ΔT_M to a heat pulse.

For a pulse like $\phi_S(t) = \phi_0\delta(t)$ where $\delta(t)$ is the Dirac delta function, equation (II.12) yields a double exponential response function [36]:

$$\Delta T_M(t) = a_1 \cdot \exp\left(-\frac{t}{\tau_1}\right) + a_2 \cdot \exp\left(-\frac{t}{\tau_2}\right) \qquad \text{(II.13)}$$

where τ_2 is mainly determined by $C \cdot R$ and τ_1 by $C_S \cdot R_{MS}$. The solution (II.13) is sketched in figure 4. Generally such a peak is introduced by a heat pulse produce by a heating wire e.g.. The evaluation of the calorimeter's response to a heat pulse allows determining the heat capacity *C* of the DSC when the resistance *R* is known from other calibrations.

II.1.2. Temperature modulated DSC (TMDSC)

Temperature modulated DSC was introduced by Reading and Gill in 1993[23,39]. So far only DSC experiments with constant heating rate were discussed. The introduction of a periodic variation in the temperature profile allows an expansion of detectable and quantifiable phenomena[23]. In a TMDSC experiment the temperature profile has the form:

$$T(t) = T_0 + \beta_u \cdot t + \Delta T_{mod} \cdot f_{mod}(t) \qquad \text{(II.14)}$$

where T_0 is the initial temperature at $t = 0$, β_u the underlying (constant) heating or cooling rate, ΔT_{mod} the modulation amplitude and $f_{mod}(t) \in [-1,1]$ a general periodic function.

Standard TMDSC is done with a sinusoidal modulation. To ease calculations the temperature is written as a complex number:

$$\begin{aligned} T^*(t) &= T_{ST}(t) + \Delta T_F^*(\omega, t) \\ &= T_0 + \beta_u \cdot t + \Delta T_{mod} \cdot \exp(i\omega t) \end{aligned} \tag{II.15}$$

In the quasi-stationary limit the response can be separated into a modulated and a stationary parts [40]:

$$\Delta\phi_{SR,tot}^*(\omega, t) = \Delta\phi_{SR,ST}(t) + \Delta\phi_{SR,mod}^*(\omega, t) \tag{II.16}$$

where $\Delta\phi_{SR,tot}^*$ is called the total, $\Delta\phi_{SR,stat}$ the stationary and $\Delta\phi_{SR,mod}^*$ the modulated heat flux. The modulated heat flux is the response to the modulated part of the temperature profile, wheras the stationary heat flux is the response to the underlying heating rate. To separate the stationary part of the response one can either take a gliding integral average of the total heat flow over one period or the mean value of the maximal and minimal values of the total heat flux for a single modulation period. If the instrument is zero-line corrected the result (stationary term) would then correspond to equation (II.4). Finally the stationary part can be subtracted from the total signal to yield the modulated heat flow. In the zeroth approximation the latter can be written as (see (A.17) in appendix A):

$$\Delta\phi_{SR,mod}^* = \frac{\Delta T_M^*}{R} = \left[\frac{1}{(1 + i\omega C_S R)} - \frac{1}{(1 + i\omega C_R R)}\right]\frac{\Delta T_F^*}{R} \tag{II.17}$$

The amplitudes of the modulated signal as well as that of the furnace temperature modulation can be attained by gliding Fourier analysis. In the case where the sample and reference crucibles have comparable heat capacity $\tilde{C}$, the sample heat capacity is mc_p, m representing the mass of the sample. If there is a slight asymmetry $\delta C \ll \tilde{C}$ between the crucibles, the sample heat capacity obeys to (see equation (A.18)):

$$mc_p = \left|\frac{\Delta\phi_{SR,mod}^*}{\Delta T_F^*}\right| \frac{\left(1 + i\omega^2\tilde{C}^2R^2\right)}{\omega} \sqrt{1 + \frac{1 + i\omega^2\left(mc_p\right)^2R^2}{1 + i\omega^2\tilde{C}^2R^2}} - \delta C \tag{II.18}$$

where $|\ldots|$ indicates the modulus of a complex quantity. To measure the heat capacity with high precision, three experiments with identical temperature profile need to be done:

1. Experiment with sample to be investigated;
2. Experiment with empty crucible with heat capacity $\tilde{C}$;
3. Calibration with a sample of known heat capacity $\hat{C}$ comparable to mc_p

With these three measurements the correction terms can be assess. From equation (II.18) one can see that this correction($\tilde{C}R$, $\hat{C}R$) become less important with smaller ω. Another relevant aspect is that underlying heating rate β_u and the modulation period should be chosen so that the heat capacity as well as the whole thermal properties of the DSC should not change considerably during a few periods. As in the

zeroth approximation the stationary part is only a response dictated by the heat capacity. A subtraction by the one of the modulated part should yield:

$$\frac{\Delta\phi_{SR,ST}(t)}{\beta_u} - \frac{1}{\omega}\left|\frac{\Delta\phi^*_{SR,mod}}{\Delta T^*_F}\right|_{Corrected} = 0 \tag{II.19}$$

assuming the modulated signal ratio is properly corrected. Leaving the quasi-stationary regime results in higher order terms in the modulation which introduce non-linearities in the measuring signal and therefore equation (II.19) will not hold anymore.

Next we consider the contribution of additional processes like transitions. This processes can to some extend couple to the modulation (for example reversible melting in polymers [41]). Therefore the heat production of the sample needs to be separated into a non-modulated and modulated contribution:

$$\phi^*_S(t) = \phi_{S,non-mod}(t) + \phi^*_{S,mod}(t, \omega, \Delta T_{mod}) \tag{II.20}$$

Equations (A.12) to (A.14) in appendix A are repeated below. They describe the response of the sample and DSC to the modulated part of the temperature profile:

(A.12)
$$\frac{\Delta T^*_M}{\Delta T^*_F} = \frac{[W^*_R - W^*_S] - W^*_R \dfrac{R_{FMS}\cdot\phi^*_{S,mod}}{\Delta T^*_F}}{W^*_R \cdot W^*_S + \dfrac{R_{FMR}}{R_{MM}} W^*_S + \dfrac{R_{FMS}}{R_{MM}} W^*_R} \tag{II.21}$$

(A.13)
$$W^*_S = \left(\frac{i\omega\tau_{S,FMS}}{1+i\omega\tau_S} + i\omega\tau_{FMS} + 1\right) \tag{II.22}$$

(A.14)
$$W^*_R = \left(\frac{i\omega\tau_{R,FMR}}{1+i\omega\tau_R} + i\omega\tau_{FMR} + 1\right) \tag{II.23}$$

Here it is important to note that the modulated part of the heat production $\phi^*_{S,mod}$ can be itself a function of temperature, modulation amplitude and angular frequency. Generally one investigates the linear regime of the heat production:

$$\Delta T_{mod} \leq \Delta T_{\text{linear limit}} \Rightarrow \frac{\phi^*_{S,mod}}{\dfrac{\Delta T^*_F}{R_{FMS}}} = \text{const.} \tag{II.24}$$

where $\Delta T_{\text{linear limit}}$ is the largest amplitude for which the response does not change with amplitude. For small amplitudes on the other side noise can hinder the separation of the modulated from the non-modulated part.

In the case of non-reversible processes we have also a contribution in the non-modulated heat production $\phi_{S,non-mod}(t)$. The measuring signal is then typically separated into two parts the reversing and non-reversing heat flux [23].

$$\Delta\phi_{SR,rev} = \left|\frac{\Delta\phi^*_{SR,mod}}{\Delta T^*_F}\right| = K' \left|\frac{\Delta T^*_M}{\Delta T^*_F}\right| \tag{II.25}$$

$$\Delta\phi_{SR,non-rev} = \langle\Delta\phi^*_{SR,tot}(\omega,t)\rangle_{t=T_\omega} - \Delta\phi_{SR,rev} \tag{II.26}$$

where K' corresponds to the calibration factor determined by melting peak integration of known samples and $\langle x^*(\omega)\rangle_{t=T_\omega}$ a gliding average over one period T_ω. In the ideal case, where there are no contributions by the DSC in the relaxing behaviour and where the system is in a quasi-stationary state, the reversing heat flux would correspond to the reversible quantities, the non-reversing heat flux to the non-reversible ones.

TOPEM

The many different characteristic times in equation (II.21) poses a problem as many of them are similar and there are many cross terms. Additionally the overall properties of the DSC change between measurements due to the drift in the system [36]. Especially when the properties of interest are to be analysed over a broad frequency range this poses a problem. An alternative method to the single frequency modulation is the stochastic step like modulation. As long as the system is exited in the linear regime a superposition of several modulated excitation results in a response in those different modulation frequencies [42]. This then allows from a single measurement to assess the response over a broad frequency range.

The other property of the system which is used is the linear response characteristic. The measured heat flux $\Delta\phi_m(t)$ is in a linear response relation with the heat flux of the sample system $\Delta\phi(t)$ (for the sake of facilitating the reading of the equations the subscript SR indicating the difference between sample and reference has been dropped) [34]:

$$\Delta\phi_m(t) = \int_{-\infty}^{t} G_S(t-t')\cdot\Delta\phi(t')\mathrm{d}t' = G_S(t)\otimes\Delta\phi(t) \tag{II.27}$$

where G_S is the Green's function or response function and can be understood as smearing function for the heat flux signal. $\otimes$ indicates the convolution product. With a non-reversing contribution in the heat production $\phi_{S,non-mod}(t) = m\cdot\Delta h_r\cdot\dot{\alpha}$ where Δh_r is the specific enthalpy and $\dot{\alpha}$ a reaction coordinate the measured heat flux can be described as [34]:

$$\Delta\phi_m(t) = \left[G_S(t)\otimes m\left(c_f\delta(t)+\dot{c}_s(t)\right)\right]\otimes\frac{\mathrm{d}\,T^*(t)}{\mathrm{d}t} + \left[G_S(t)\otimes m\cdot\Delta h_r\cdot\dot{\alpha}\right] \tag{II.28}$$

where c_f is the part of the heat capacity which is given by the fast changing internal degrees of freedom (i.e. modes of oscillations of single molecules) and $\dot{c}_s(t)$ the part of coupling to long time changes of internal degree of structure such as structural relaxations in meta stable equilibrium [34]. The measured heat flux can therefore be separated into a smeared sensible heat flux

$$\Delta\phi_{sens,s}(t) = G(t)\otimes\frac{\mathrm{d}\,T^*(t)}{\mathrm{d}t} \tag{II.29}$$

with the instrument sample pulse response function:

$$G(t) = G_S(t)\otimes m\left(c_f\delta(t)+\dot{c}_s(t)\right) \tag{II.30}$$

and latent heat flux

$$\Delta\phi_{lat}(t) = m \cdot \Delta h_r \cdot \dot{\alpha} \tag{II.31}$$

where the smearing contribution $G_S(t)$ was neglected as for very low underlying heating or cooling rates β_u the process are much slower than the instrumental timescales.

The integration of the pulse response function yields [34]:

$$\begin{aligned}\int_0^\infty G(t)\mathrm{d}t &= m\left(c_f \int_0^\infty G_S(t)\mathrm{d}t + \int_0^\infty \int_{-\infty}^{t'} G_S(t'-t'')\dot{c}_s(t'')\mathrm{d}t''\,\mathrm{d}t'\right) \\ &= m\big(c_f + c_s(t\to\infty)\big) = mc_{p,0}\end{aligned} \tag{II.32}$$

with a normalized device response function $\int_0^\infty G_S(t)\mathrm{d}t = 1$. To check if the device response function is really normalized a sample of known heat capacity can be measured. The deviation from the normalisation can then be taken as calibration factor.

To get the static heat capacity $c_{p,0}$, the pulse response function of the system needs to be obtained. A discrete z-transformation is applied to the measure signal [34]:

$$\Delta\phi_m(z^*) = \sum_{n=0}^{\infty} \Delta\phi_m(n\cdot\Delta t)\cdot(z^*)^{-n} \tag{II.33}$$

where z^* is a complex variable. It is important to note that the heat flux signal is described by the measuring interval Δt and measuring point n. To change the discrete z-transformation to a discrete Fourier transformation one substitutes $z^* = e^{i\omega\cdot\Delta t}$. The advantage of this transformation is that the convolution product $\otimes$ reduces in z^*-space to an algebraic product.

$$\Delta\phi_m(z^*) = g^*(z^*)\cdot\beta(z^*) + \Delta\phi_{lat}(z^*) \tag{II.34}$$

with

$$g^*(z^*) = \sum_{n=0}^{\infty} G(n\cdot\Delta t)\cdot(z^*)^{-n} \tag{II.35}$$

$$\beta(z^*) = \sum_{n=0}^{\infty} \frac{\mathrm{d}\,T^*(t)}{\mathrm{d}t}(n\cdot\Delta t)\cdot(z^*)^{-n} \tag{II.36}$$

The response function in z^*-space is then estimated with a fraction of polynomials :

$$g^*(z^*) = \left(\sum_{n=0}^{p} b_n\cdot(z^*)^{-n}\right)\cdot\left(\sum_{n=0}^{q} a_n\cdot(z^*)^{-n}\right)^{-1} \tag{II.37}$$

with the translation identity in z^*-space

$$\Delta\phi_m(n\cdot\Delta t)\cdot(z^*)^{-k}=\Delta\phi_m\big((n-k)\cdot\Delta t\big) \tag{II.38}$$

equations (II.34) with (II.37) can be rewritten as [34]:

$$\begin{aligned}\Delta\phi_m(k\cdot\Delta t)=&\sum_{n=0}^{p}b_n\cdot\beta\big((k-n)\cdot\Delta t\big)\\&-\sum_{n=1}^{q}a_n\cdot\Delta\phi_m\big((n-k)\cdot\Delta t\big)+\Delta\phi_{lat}\sum_{n=0}^{q}a_n\end{aligned} \tag{II.39}$$

where $\Delta\phi_{lat}(z^*)=\Delta\phi_{lat}$ was assumed to be constant in the range of interest. Equation (II.39) describes the heat flux signal at the point *k* by the prior temperature and heat flux. In this case *p* is a limiting factor for the influence of the temperature history and *q* is related to the heat history of the system. For the evaluation equation (II.39) is set up for each data point in the interval of interest. a_n, b_n and $\Delta\phi_{lat}$ can then be found by resolving the linear system of those equations. For example with an evaluation window of 180 seconds and a measuring interval of 0.1s one can use the first 90 seconds as initiation time and establish a linear system of 900(=90s/0.1s) equations which would allow the same amount of free parameters. When a_n and b_n are established the pulse response function for the system can be calculated in Fourier space $g^*(\omega)=g^*\big(z^*=e^{i\omega\cdot\Delta t}\big)$. The static heat capacity is then given in the limiting case $\omega\to 0$ [43]:

$$g^*(\omega\to 0)=\int_0^\infty G(t)\mathrm{d}t=mc_{p,0} \tag{II.40}$$

As soon as the linear parameters a_n and b_n are established the static heat capacity can be calculated. The responses to temperature change are only exact in the range defined by *p.* Outside of this range the found heat capacity corresponds to an extrapolation related to these parameters. To check the correctness of this extrapolation, the pulse length and the evaluation window are normally increased. If $g^*(\omega)$ does not change with pulse length one can conclude that the complex heat capacity is completely assessed.

The last step is the separation of the frequency dependency of the DSC and the investigated sample. As the convolution product is a simple product in Fourier space, equation (II.30) can be transformed to:

$$g^*(\omega)=g_s^*(\omega)\cdot m\cdot c_{p,app}^*(\omega) \tag{II.41}$$

where $g_s^*(\omega)$ is the one sided Fourier transform of $G_S(t)$ and the apparent heat capacity $c_{p,app}^*(\omega)$ describes the instantaneous and long-time behaviour of the samples heat absorption to a temperature change. $g_s^*(\omega)$ is then estimated in

regions where one can expect the heat capacity to be time independent on the timescale of the modulation $c^*_{p,app} = c_{p,0} \neq c^*_{p,app}(\omega)$:

$$g^*_s(\omega) = \frac{g^*(\omega)}{mc_{p,0}} \tag{II.42}$$

$g^*_s(\omega)$ is generally defined on both sides of a transition area and interpolated to the transition area. For the glass transition i.e. $g^*_s(\omega)$ is established in the glassy and the liquid phase.

Debye Relaxator

To describe the Fourier transform of the step response function a Debye relaxator is taken as model:

$$g^*(\omega) = C_{p,\infty} + \frac{\Delta C_p}{1 + i \cdot \omega \cdot \tau} \tag{II.43}$$

where $c_{p,\infty}$ is the response for $\omega \to \infty$, Δc_p corresponds to the relaxing part and τ is a relaxation time. In the limit $\omega = 0$ $g^*(\omega)$ becomes $g^*(\omega = 0) = C_{p,\infty} + \Delta C_p = mc_{p,0}$. The Debye model corresponds to the Fourier transform of an exponential decay after a heavy-side step. Figure 5 shows the example of a Debye fit of the response function.

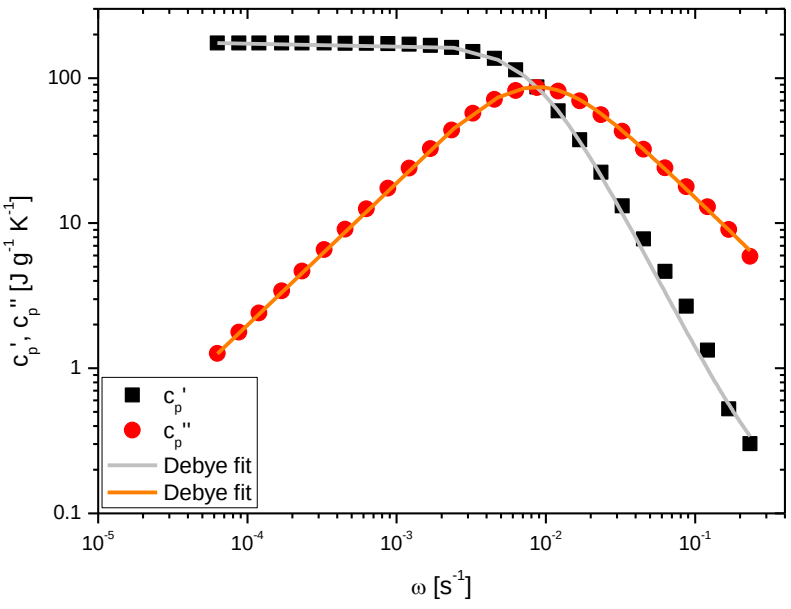

Figure 5: Real and imaginary part of the step response function gained by the TOPEM measurement of a C20 sample in the rotator phase. Lines indicate the Debye fit of the data.

II.2. X-ray diffraction

The wave length of x-rays are in the range of ~ 0.1 to ~ 100Å. For the investigation of crystalline structure a copper k-α source is commonly used, as the resulting x-rays have an average wavelength of λ=1.54187 Å [44]. This wavelength is close to the distance between atoms or molecules in crystalline structure and therefore useful for scattering experiments. For x-ray diffraction only the elastic scattering on the atoms is considered. In an ordered state we have then layers which are described by translational symmetry. In general this symmetry can be described by a lattice structure with 3 lattice parameters (*a, b, c)* and 3 angles (α, β, γ). The layers can then be described by Miller indices (h k l) (see Figure 6). For the beams depicted in figure 6 the constructive interference criteria is:

$$2\Delta = n \cdot \lambda \tag{II.44}$$

one can derive Bragg's law:

$$2d_{hkl} \cdot \sin(\theta_{hkl}) = n \cdot \lambda \tag{II.45}$$

where d_{hkl} is the lattice spacing and θ_{hkl} the angle at which in a $2\,\theta$ experiment constructive interference is observed. A useful relation to asses the relation between peaks in the difractogram is:

$$d_{nh,nk,nl} = \frac{1}{n} d_{hkl} \tag{II.46}$$

When the actual scattering sites in the lattice structure and the type of atom is known one can even deduce the relative intensity of the scattering peaks in the difractogram [44].

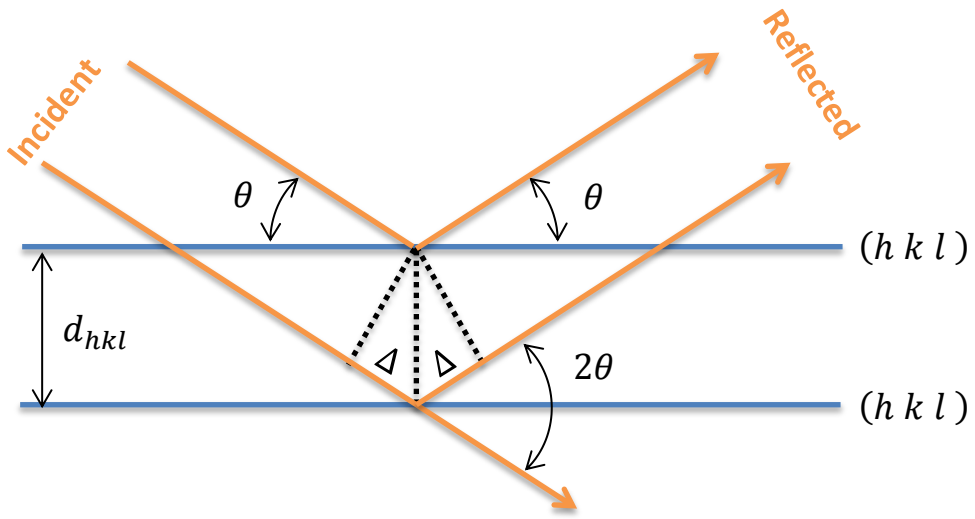

Figure 6:Sketch of Braggs law

III. Experimental

III.1. Material

In this work we investigate n-eicosane ($C_{20}H_{42}$, C20) which, is a simple hydro-carbon chain. Two batches of C20 were acquired from Sigma-Aldrich. According to indications by the manufacturer the first batch has a purity of 99.0+% and the second batch one of 99.5+%. Gas chromatography and mass spectroscopy measurements yielded that 3-methyl-nonadecane is the main impurity for the 99.0+% batch.

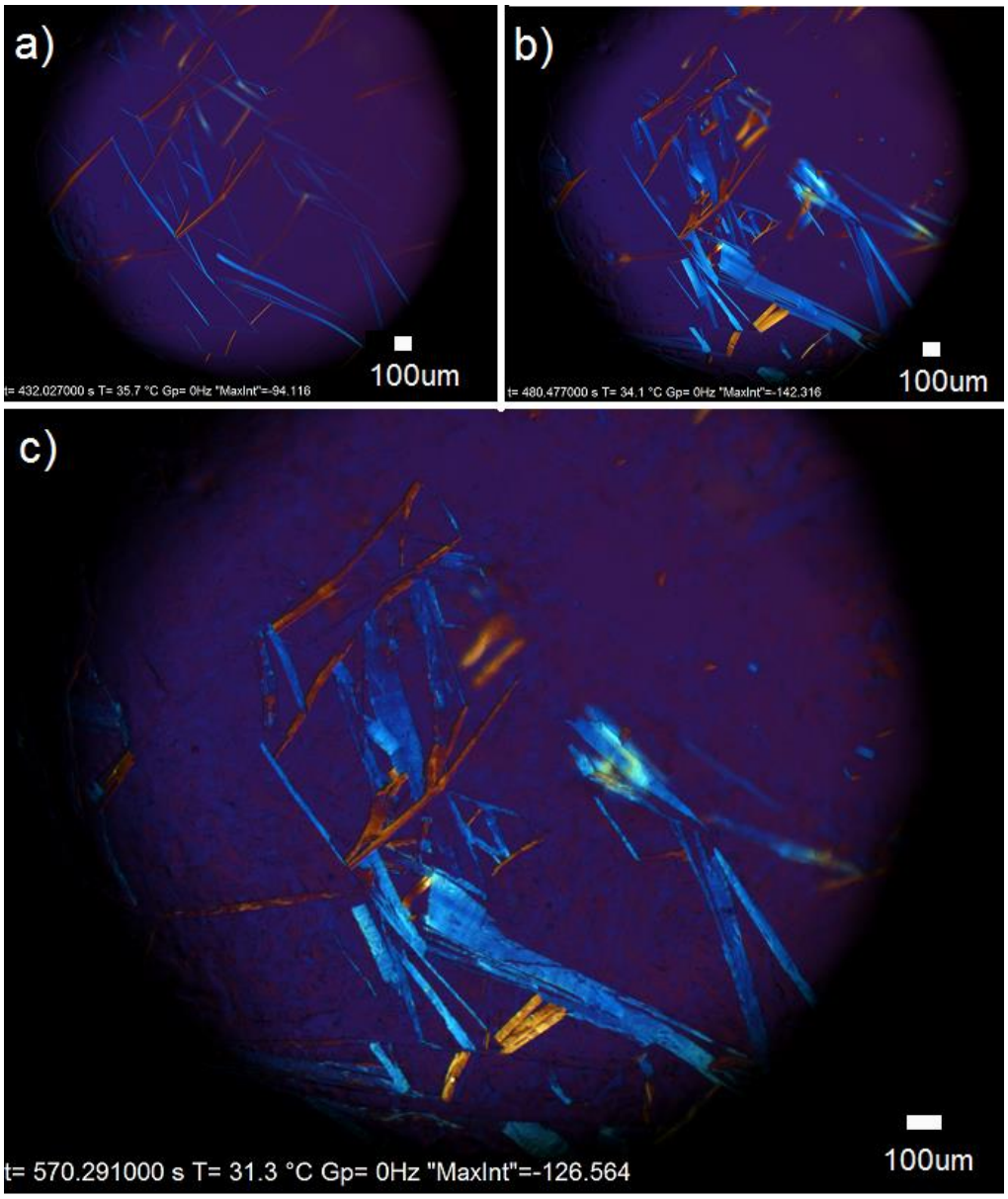

Figure 7: Polarisation optical micrographs(POM) with λ-plate and crossed polarisers of a thin C20 sample with 99.0+% purity. a) Rotator phase at 308.75 K b) Rotator phase at 307.25 K and c) triclinic phase at 304.45 K

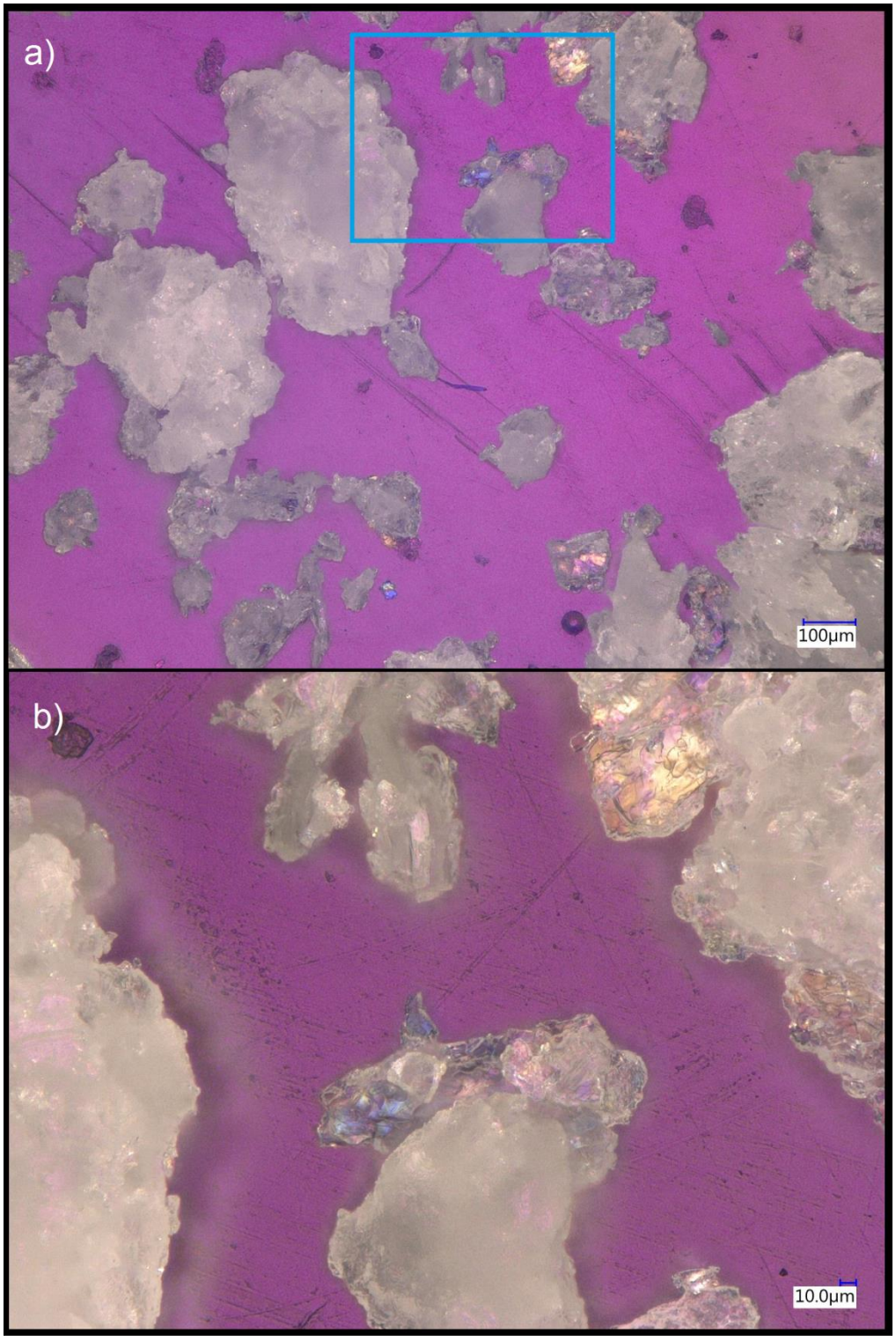

Figure 8: POM of a C20 sample of 99.0+% purity in the triclinic phase in powder form.

Figure 7 shows polarisation optical micrographs of a thin layer of a C20 sample with purity 99.0+% for the rotator phase and triclinic phase. In figure 8 polarisation optical micrographs of a powder is depicted.

III.2. Calorimetry

Calorimetric measurements were performed with a DSC822e from Mettler-Toledo. This disc type heat flux calorimeter is shown in figure 9. It consists of a silver block furnace with a HSS8 sensor disc ceramic. The disc has 120 thermocouples to achieve a high precision in the temperature differences between sample and crucible. Nitrogen was used as purge gas with a flow rate between 30 and 35 mL/min. The calibration of temperature and heat flow was done with adamantine, naphthalene, benzoic acid and indium. Additionally a lag time correction was acquired by these calibration-measurements which is used for the standard DSC runs.

The weights of the C20 samples examined by calorimetry ranged between 2 and 28 mg. Samples were filled into aluminium pans closed with a lid (volume: 40 µL; weight: around 50 mg). Reference pans were chosen with weights deviations below 0.05 mg from those of the respective sample crucible. Before adding the samples the pans were cleaned consecutively in an acetone bath and two ethanol baths and then dried at 60-80°C in an oven with or without vacuum.

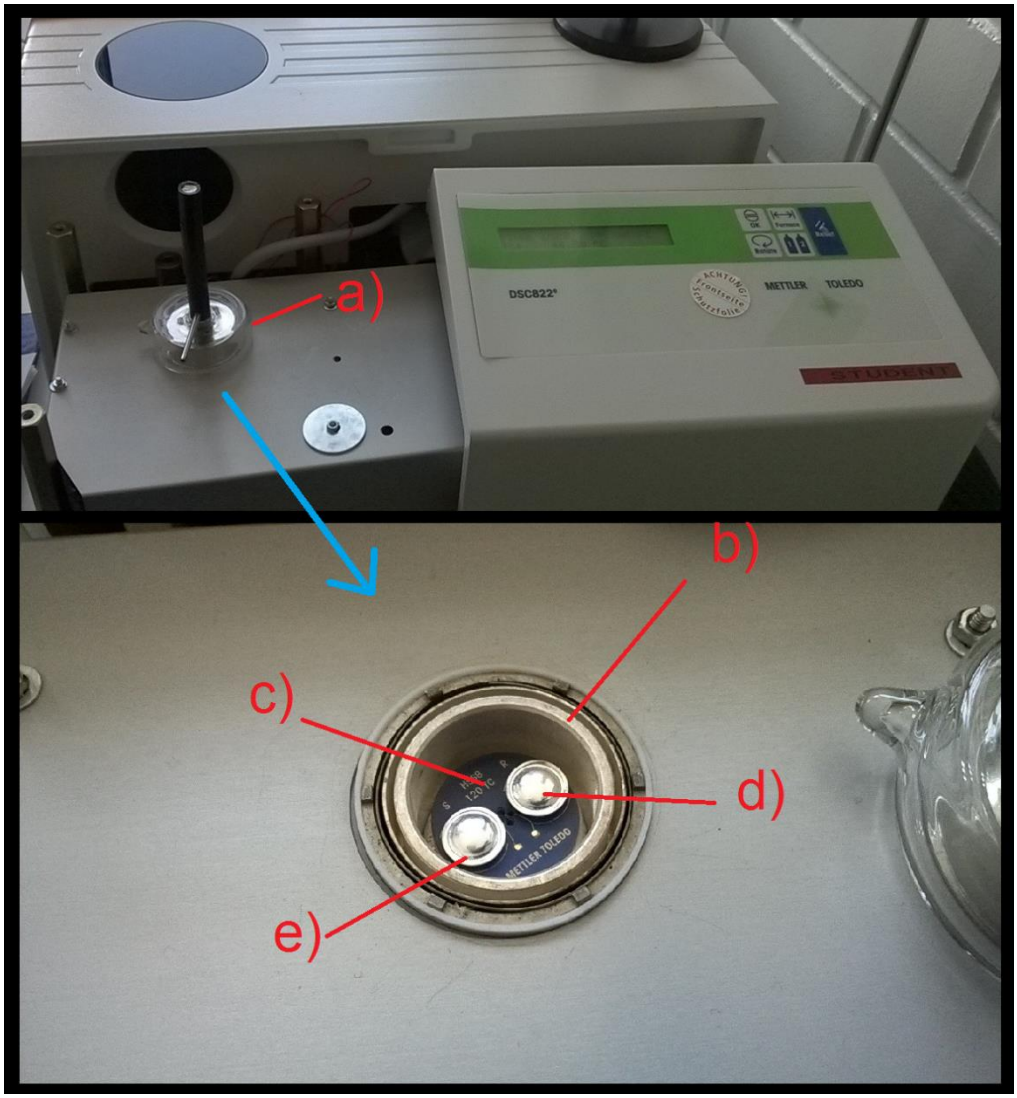

Figure 9: Setup of disk type calorimeter DSC822e a) lid, b) silver furnace, c) HSS8 measuruing disc, d) reference crucibles, e) sample crucibles.

Classical DSC runs with constant heating rates ranging between 0.25 K/min and 1 K/min were performed to acquire onset temperature as well as heat of fusion ΔH_f of C20 in its rotator and triclinic phases. The evaluation of the heat of fusion ΔH_f was done with the STARe software by Mettler TOLEDO. First a base line is defined. We took as baseline the extrapolation of the heat flow of the liquid phase. Then the difference between the heat flux signal and the base line is integrated over time while the starting point and end points are defined by the intersections of those two curves like described in section II.1.1. Melting peaks of naphthalene were used as calibration the peak area.

TOPEM measurements were done with the same samples and crucibles. The impact of different measuring parameters is shown in appendix B. In figure 10 the modulated part of temperature profile is depicted for measurements with different pulse length Δt_p. The dashed lines indicate the set amplitude. The actual measured furnace temperature is slightly outside these margins. This nevertheless does not impact the findings as the furnace temperature is used for the TOPEM algorithm. The measuring parameters mostly used in this work are listed in section IV.3.1. The evaluation algorithm in the STARe software was used to evaluate the TOPEM measurements. A sapphire sample was investigated in the same temperature range as the C20 to calibrate the quasi-static heat capacity.

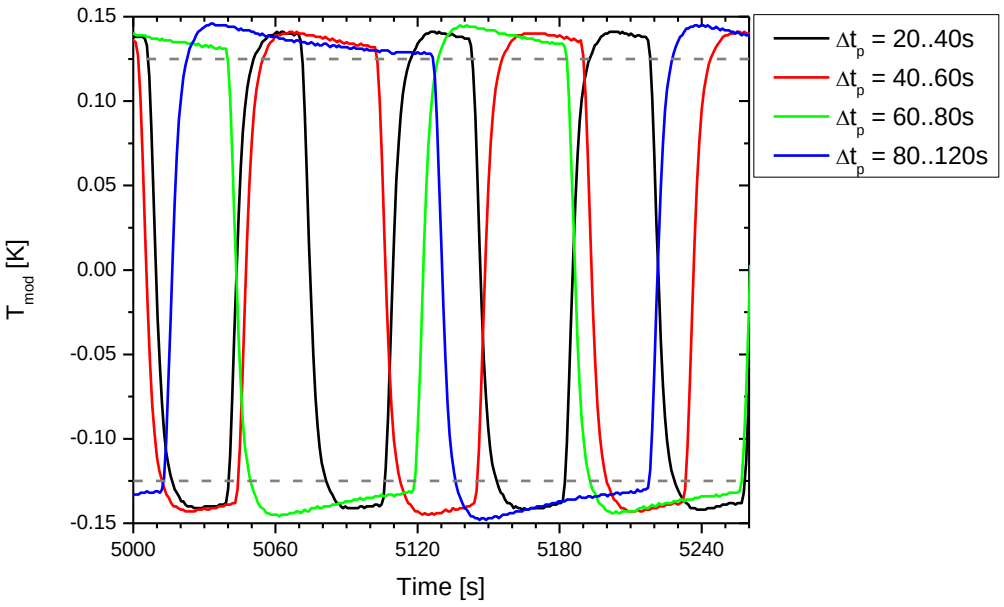

Figure 10: Measured modulation part of the temperature T_{mod} for different pulse lengths Δt_p over time for a TOPEM measurement.

III.3. X-Ray diffraction

The XRD measurements were realized using a D8 Discovery diffractometer from Bruker. A CuKα-tube ($\bar{\lambda}$=1.5418 Å) equipped with a Kβ-absorber was used in combination with a LYNXEYE XE 1D line detector to allow for fast scan rates. Scans were performed using with Bragg-Brentano diffraction geometry and a θ-2θ mode. The sample was kept in a furnace (see figure 11). The sample holder consists of a nickel coated cupper block with an indentation volume of 12x15x1 mm^3 (WxLxH) to house samples. A heating ribbon is positioned in the middle of the sample holder to regulate temperature. A thermocouple for temperature measuring and controlling is mounted directly on the sample holder at a distance of 4 mm to the sample. A cooling finger is positioned below the sample. The whole furnace can be positioned vertically to adjust the sample position. To do so the tube and detector were aligned and the total intensity hitting the detector was measured while raising the furnace. The position where the intensity becomes half of the maximal intensity was taken as zero height.

Measurement programs were established with temperature profiles and scan schedule. For this scans with moving tube and detector were chosen as they delivere better diffractogram with less artefacts then measurements with fixed detector position.

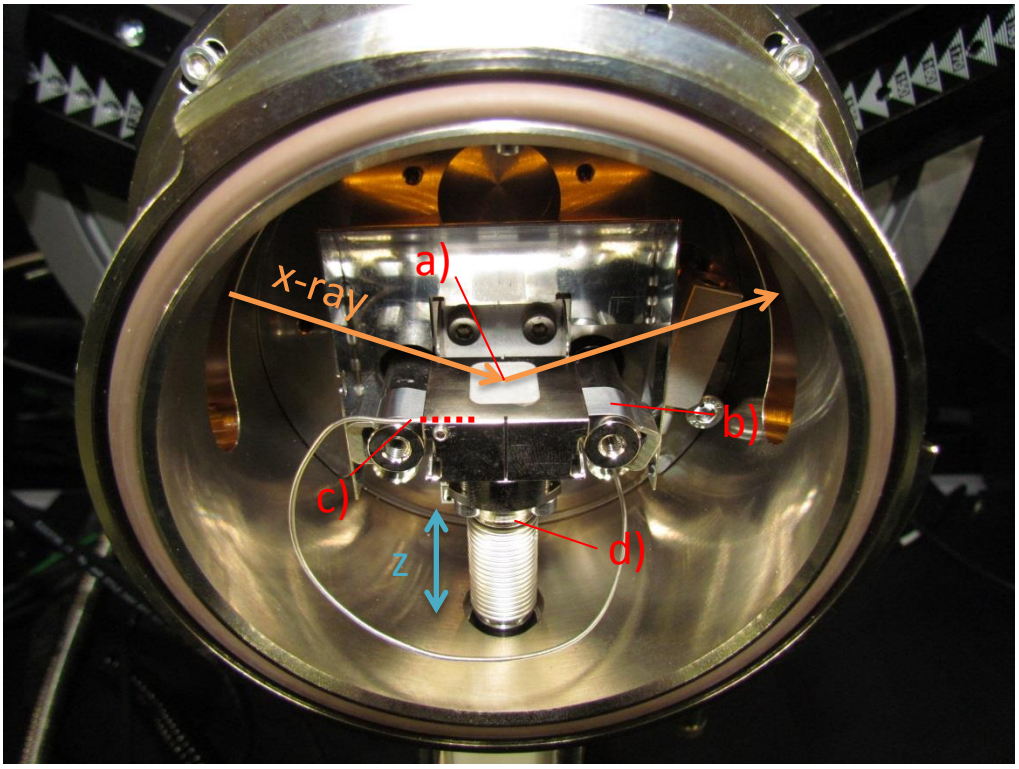

Figure 11: XRD furnace with a) sample, b) heating ribbon, c) thermocouple and d) cooling finger.

IV. Results

IV.1. Basic results from calorimetry

IV.1.1. Characteristic temperatures

Normally the melting temperature is defined as the onset temperature corresponding to the intersection of the extrapolation of the linear regime of a melting peak with the DSC signal of the crystalline phase[36]. For a material undergoing a 1st order phase transition with a sharply defined melting temperature, the oven is still heating, while the sample stays at the melting temperature as long as coexistence of crystalline and liquid phase exists [36]. This explains why at a constant heating rate we observe a linear increase of the heat flow which results from the temperature difference between sample and reference.

For a material showing an extended melting range, the latter criterion does not hold anymore. Here one can observe a linear regime pointing to an onset temperature which is below the temperature at which the whole material is melted for sure. Therefore we made an experiment with a stepwise increase of the temperature, starting at a temperature well below the melting range. As long as the sample is in the extended melting range, the step-wise increase of temperature results in latent heat flow. The length of the isothermal segments between the temperatures steps were chosen so that the measured heat flow relaxed to the baseline. The last temperature step which results in latent heat flow is then looked upon being the step to the final melting temperature. These two characteristic temperatures – onset and final melting temperature - shall help as frame of reference for the following investigations.

Onset temperatures

The onset temperatures have been derived for the rotator (RI) and triclinic (T) phases of samples with different purities and masses. To check the reproducibility several measurements were done for each sample. In figure 12 the onset temperatures have been determined for the RI and T phases of a C20 sample with a purity of $99+\%$ and a mass of $m = 2.31\mathrm{mg}$. Obviously the onset temperature is lower for the RI phase than for the T phase. This observation explains why the rotator phase cannot be attained by heating a sample which is in the triclinic phase [8,29]. This also proves the metastability of the RI phase. Before reaching the linear region of the melting peak, the DSC signal already shows a significant increase below the onset temperatures. This could be explained by an increase of defects created by conformational changes in the C20 molecules [5,28,45]. The experimental finding that the slopes of the two lines, used to determine the onset temperatures, are very similar leads to the conclusion that they mainly relate to the heating rate β.

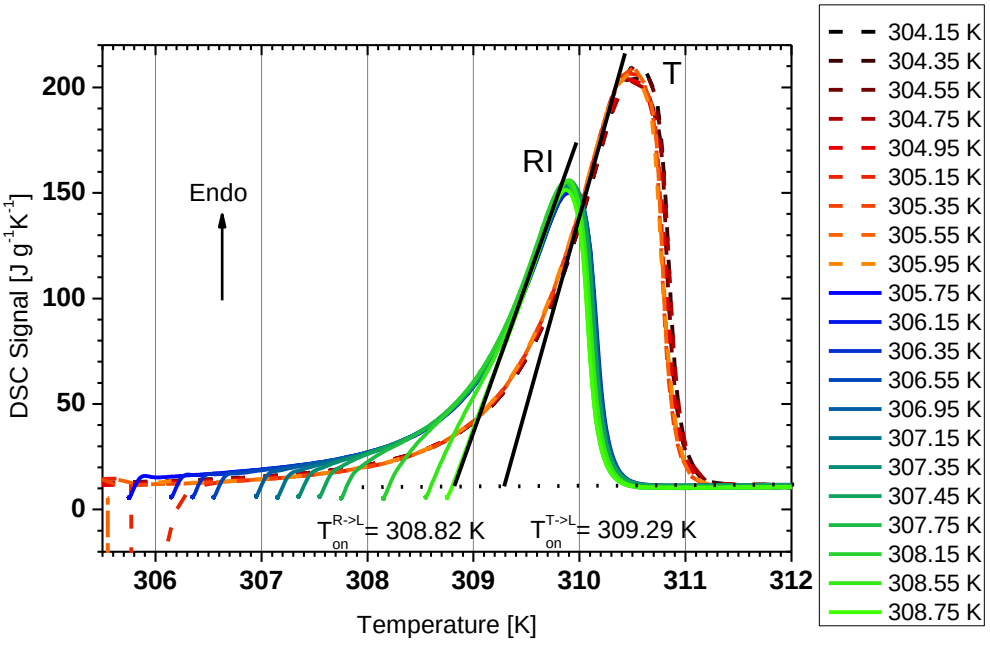

Figure 12: DSC runs for a C20 with a mass of m=2.31mg and purity 99+%. Sample was cooled from the melt with a rate of β=1K/min to an isotherm (temperature indicated in the legend). After staying for 30min in the isotherm the sample was heated with a rate of β=1K/min. The DSC signals in the graph show the behaviour of RI (solid) and T (dashed) of close to the liquid transition while heating.

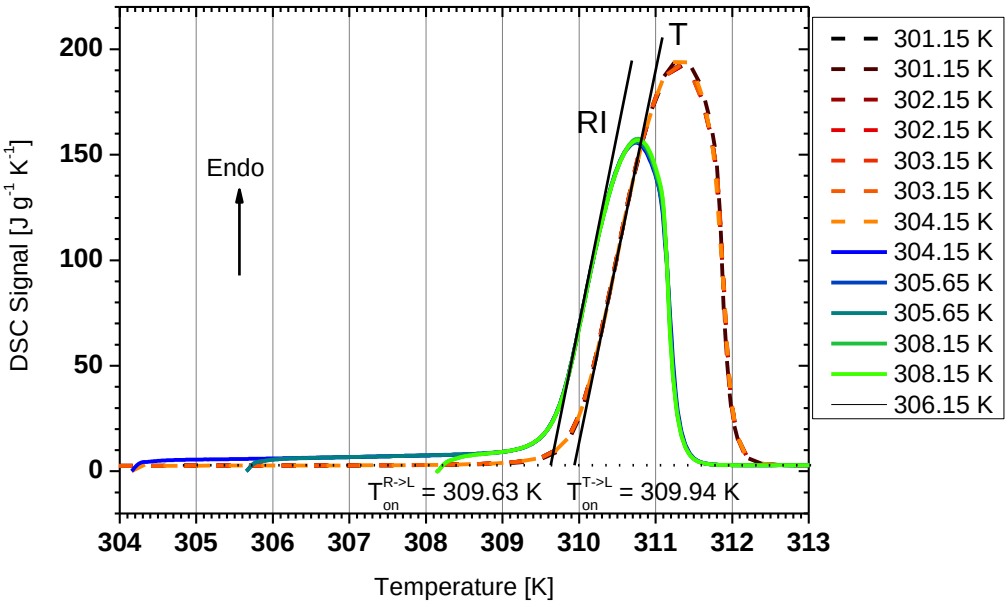

Figure 13: DSC runs for a C20 with a mass of m=4.24mg and purity 99.5+%. Sample was cooled from the melt with different rates to an isotherm (temperature indicated in the legend). After staying for 10min in the isotherm the sample was heated with a rate of β=1K/min. The DSC signals in the graph show the behaviour of RI (solid) and T (dashed) close to the liquid transition while heating.

Figure 13 reveals same investigation of a C20 sample with a higher purity (99.5+%) and a mass of $m = 4.42\text{mg}$. Still the onset temperature of the RI phase is below the one of the T phase. However, compared to the results obtained for the 99.0+% sample (see figure 12), the behaviour of the DSC signal preceding the linear increase of the melting peak is different for both phases. This deviating behaviour between both samples can be explained by a larger amount of defects introduced by chain length mismatch [46]. It should also be noted that the increased purity shifts the onset temperatures by about 0.8 K for the RI and by 0.7 K for the triclinic phase. The melting temperature suppression by impurities is a known phenomenon for other materials [47,48].

Figure 14 and figure 15 allow for comparing the evolution of the onset temperatures as a function of the heating rate for a low purity (99.0+%) – and a high purity (99.5+%)-sample. Obviously the heating rates only marginally influence the onset temperatures. Irrespective of the phase (RI or T) the deviation between the obtained values of the onset temperature is lower than the error regularly associated to the experimental method $\Delta T = \pm 0.1\ K$ [36]. Almost two years have passed between the measurements represented in figure 12 and figure 14. During this period the DSC was calibrated twice. This clearly demonstrates the reproducibility of the data.

Another effect which has to be considered is the influence of the sample surface on the melting behaviour. N-alkanes are known for having a very thin crystalline surface above the melting temperature of the bulk crystal [49,50]. Therefore it is important to check if there is an influence of the volume to surface ratio on the melting behaviour. Figure 16 illustrates the evolution of the onset temperature as a function of the sample (purity 99.0+%) mass. We observe that the samples with masses 2.31mg, 8.22mg and 23.67mg have approximately the same onset temperatures $T_{on}^{R\to L} = (308.79 \pm 0.05)\text{K}$ for the RI phase and $T_{on}^{T\to L} = (309.23 \pm 0.14)\text{K}$. The deviation of the onset temperature of the 13.43mg sample is related to the crucible positioning and will be further discussed in section IV.2.1.

In figure 17 the onset temperatures of the melting peak samples with a purity of 99.5+% and different masses are determined. The data yields for each mass (4.24mg, 15.82mg and 23.12mg) similar onset temperatures. We obtain $T_{on}^{R\to L} = (309.73 \pm 0.10)\text{K}$ for the RI phase and $T_{on}^{T\to L} = (310.06 \pm 0.12)\text{K}$ for the T phase.

In figure 18 all of the results obtained for the melting onset temperatures are summarized. In case of samples with lower purity (99.0+%) the difference between the onset temperatures of the RI and T phases scatter between 0.3 K and 0.6 K. For samples of higher purity (99.5+%) the difference between $T_{on}^{R\to L}$ and $T_{on}^{T\to L}$ seems to be better defined. Comparing the differences between the onset temperatures for the two degrees of purity we receive an offset of 1.0 K for the RI phase and around 0.8 K for the T phase.

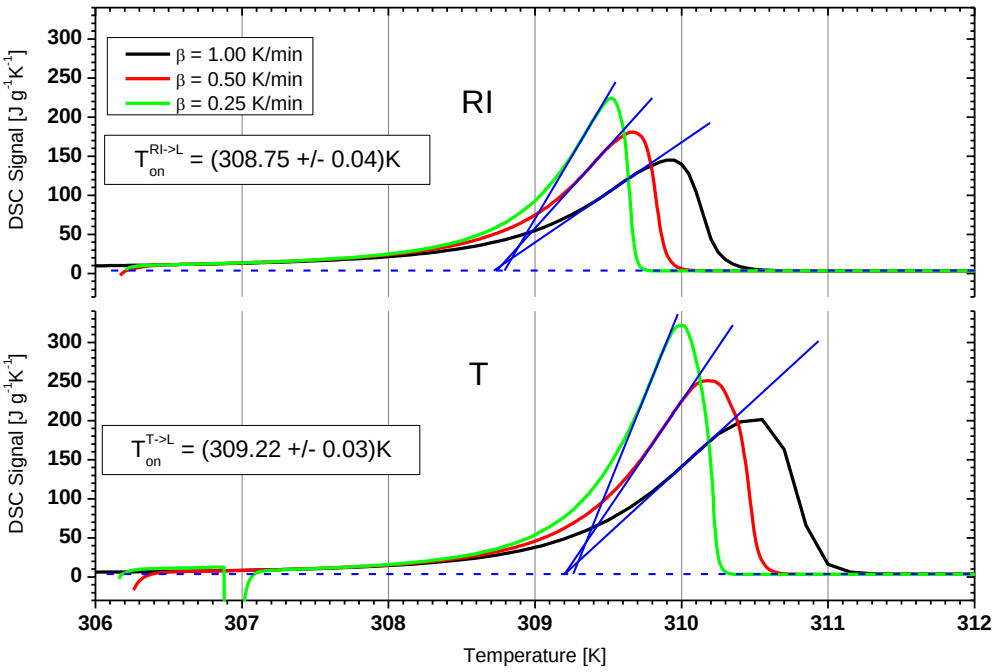

Figure 14: DSC runs for a C20 sample with a mass of m=2.31mg and purity 99+%. DSC signals for different heating rates β = 1; 0.5; 0.25 K/min shown in black; red and green respectively. Top: the melting of the RI phase is shown. Bottom: the melting of the T phase is shown. For both the onset temperature are displayed by the intersections of the extrapolated lines and the baseline of the liquid phase.

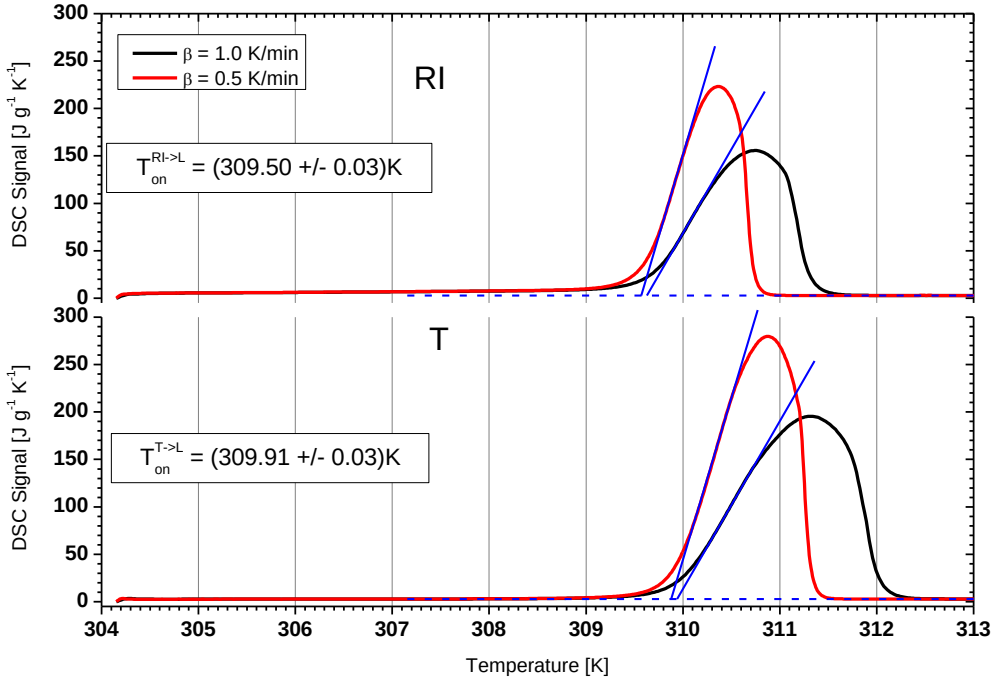

Figure 15: DSC runs for a C20 sample with a mass of m=4.24mg and purity 99.5+%. DSC signals for different heating rates β = 1; 0.5 K/min shown in black and red respectively. Top: the melting of the RI phase is shown. . Bottom: the melting of the T phase is shown. For both the onset temperature are displayed by the intersections of the extrapolated lines and the baseline of the liquid phase.

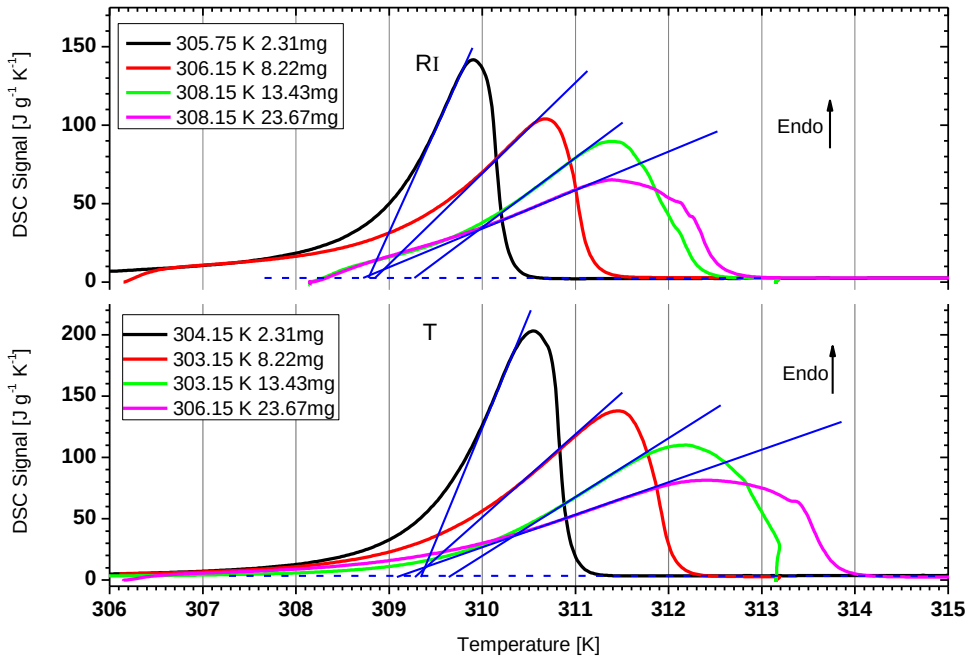

Figure 16: DSC runs for severalC20 samples a purity of 99+%. DSC signals for different masses 2.31; 8.22; 13.43; 23.67 mg shown in black; red, green and magenta respectively. All measurements were done with a heating rate of β = 1 K/min. Top: the melting of the RI phase is shown. Bottom: the melting of the T phase is shown. For both the onset temperature are displayed by the intersections of the extrapolated lines and the baseline of the liquid phase.

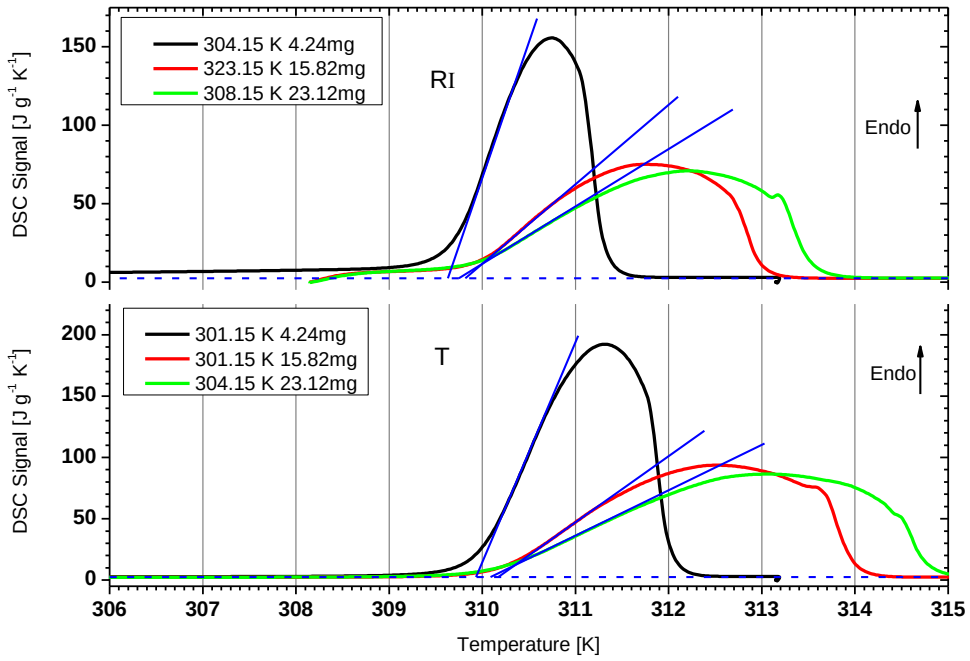

Figure 17: DSC runs for severalC20 samples a purity of 99.5+%. DSC signals for different masses 4.24; 15.82; 23.12 mg shown in black; red and green respectively. All measurements were done with a heating rate of β = 1 K/min. Top: the melting of the RI phase is shown. Bottom: the melting of the T phase is shown. For both the onset temperature are displayed by the intersections of the extrapolated lines and the baseline of the liquid phase.

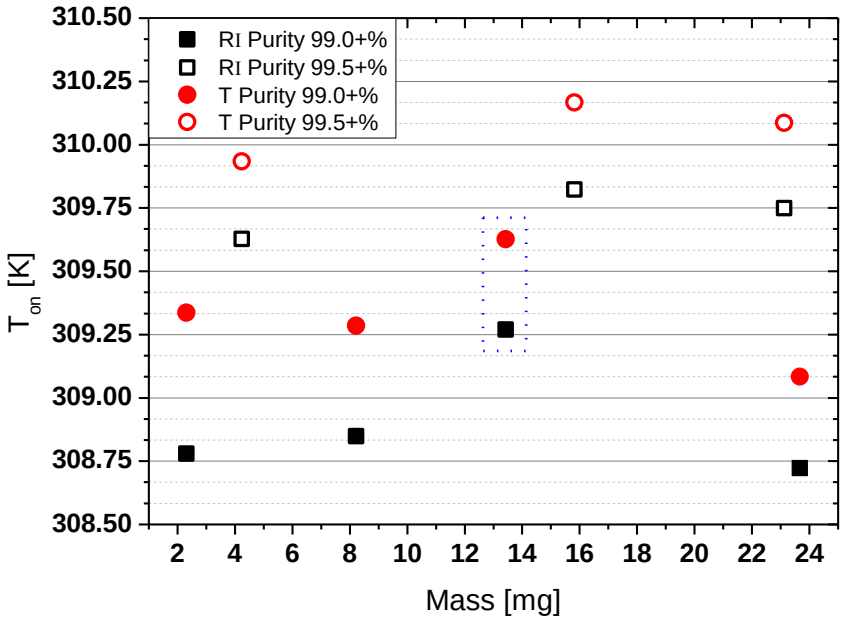

Figure 18: Onset temperatures for C20 samples with different masses and purities. Solid symbols are the onset temperatures for the samples taken from a batch with 99+% purity. Hollow symbols are the onset temperatures for the samples taken from a batch with 99.5+% purity. Blue dotted square indicates measurements of as sample with a typical behaviour.

Final melting temperatures

Final melting temperatures were determined for samples with both degrees of purity (99.0+% and 99.5+%). To see the impact of different masses to the final melting temperature see sub-chapter IV.2. Figure 19 and figure 20 depict the heat flux and temperature as a function of time for melting of the rotator and the triclinic phase respectively. The purity of the investigated sample was 99+%. Temperature steps close to the transition yield an increased and broader heat flux response. Examination of figure 19 and figure 20 reveal that after some time the two first peaks relax to the respective baselines of the heat flux. The last two steps show different heat flow behaviour: the response peaks show no long time relaxation and depict an overshoot. Responses of such a kind can be associated to the heat capacity of the liquid phase. These final heat flow peaks are very fast [23]. They are able to mimic the unavoidable temperature overshoots. As the final melting can start at any temperature between two successive isotherms the mid-value between both is taken as equilibrium melting temperature. Thus we get $T_m^{R\to L} = (309.3 \pm 0.05)\mathrm{K}$ and $T_m^{T\to L} = (309.7 \pm 0.05)\mathrm{K}$ for the low purity (99+%) sample.

For the sample with higher purity (99.5+%) we chose smaller temperature steps ($\Delta T = 0.05\mathrm{K}$) and isotherms with a longer duration of 60 minutes. This time span was still not sufficient to let the heat flux fully relax to the baseline. As the steps are smaller we still get the same accuracy as for the low purity samples. We obtain $T_m^{R\to L} = (309.55 \pm 0.05)\mathrm{K}$ and $T_m^{T\to L} = (309.9 \pm 0.05)\mathrm{K}$

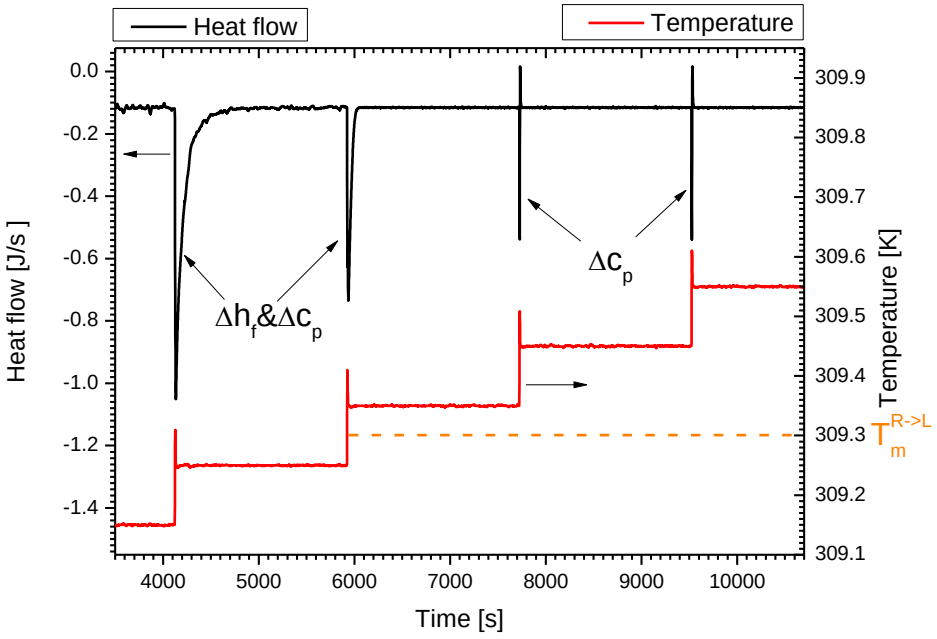

Figure 19: Determination of equilibrium melting temperature rotator phase by stepwise increase of temperature for a C20 sample with a mass of m=2.31mg and a purity of 99+%. 0.1K steps were chosen with a time at the isotherm of 30 minutes. One-sided broad peaks in the heat flow indicate a latent heat contribution. Sharper two-sided response indicates a fast response by the heat capacity.

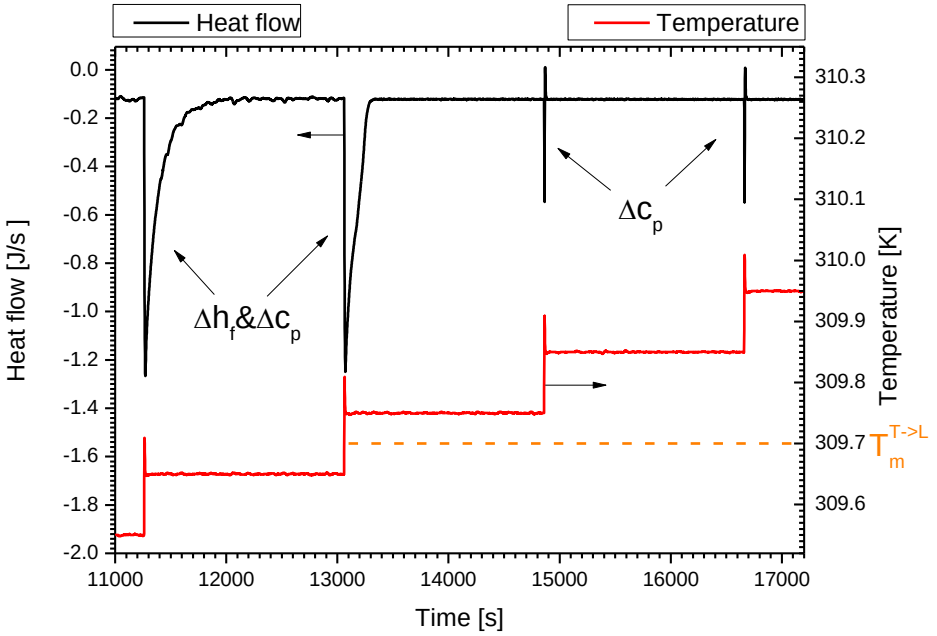

Figure 20: Determination of equilibrium melting temperature of the triclinic phase by stepwise increase of temperature for a C20 sample with a mass of m=2.31mg and a purity of 99+%. 0.1K steps were chosen with a time at the isotherm of 30 minutes. One-sided broad peaks in the heat flow indicate a latent heat contribution. Sharper two-sided response indicates a fast response by the heat capacity.

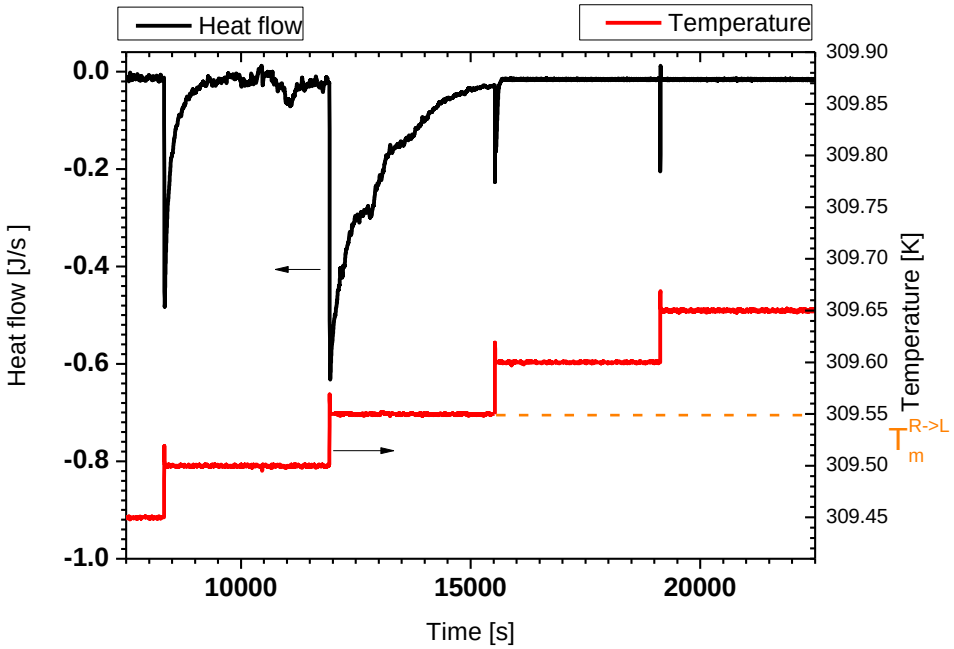

Figure 21: Determination of equilibrium melting temperature of the rotator phase by stepwise increase of temperature for a C20 sample with a mass of m=4.24mg and a purity of 99.5+%. 0.05K steps were chosen with a time at the isotherm of 60 minutes. One-sided broad peaks in the heat flow indicate a latent heat contribution. Sharper two-sided response indicates a fast response by the heat capacity.

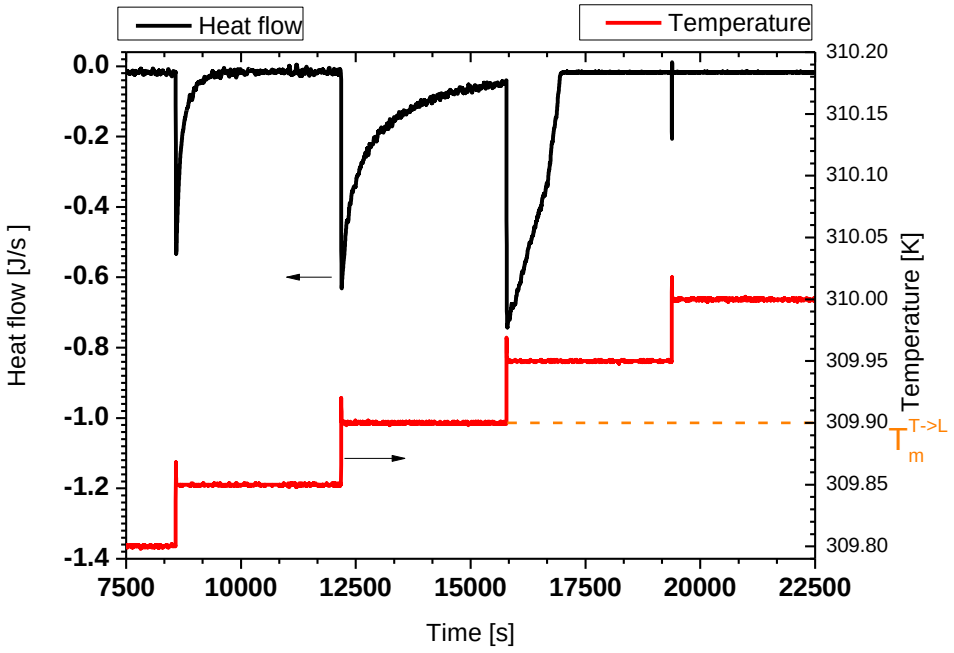

Figure 22: Determination of equilibrium melting temperature of the triclinic phase by stepwise increase of temperature for a C20 sample with a mass of m=4.24mg and a purity of 99.5+%. 0.05K steps were chosen with a time at the isotherm of 60 minutes. One-sided broad peaks in the heat flow indicate a latent heat contribution. Sharper two-sided response indicates a fast response by the heat capacity.

Table 1: Summary of characteristic temperatures for C20 samples with different purities

Temperature / Purity	Onset temperature in K		Final melting temperature in K	
	RI	T	RI	T
99.0+%	308.79±0.05	309.23±0.14	309.3±0.05	309.7±0.05
99.5+%	309.73±0.10	310.06±0.12	309.55±0.05	309.9±0.05

In table 1 the characteristic temperatures determined as described above are summarized. For the sample with lower purity we observe a clear separation of the onset and final melting temperatures. For the sample with higher purity the onset temperatures are slightly larger than the final melting temperatures but in the range of the experimental inaccuracy. From this it follows that the melting range seems to be influenced by the impurity of the samples.

IV.1.2. Heat of fusion

The measurement of latent heat represents an adequate tool for the investigation of mass related effects affecting the overall crystallinity of the samples.

The peak integration described in sub-chapter III.2 is depicted in figure 23 for the melting and crystallisation peaks. They correspond to the heat of fusion. The two step crystallisation into first the rotator phase (first broader peak) and then into the triclinic phase (second sharper peak) can be seperated. The specific heat of fusion is then calculated by dividing the heat of fusion by the samples masses m

$$\Delta h_f = \frac{\Delta H_f}{m} \qquad \text{(IV.1)}$$

In figure 24 the specific heat of fusion as a function of mass is shown for different C20 samples with a purity of 99.0+%. Melting and crystallization yield differences between the respective specific heat of fusion values lower than 1%. The average values are $\Delta h_{f,melt} = (255.4 \pm 1.0)\,\mathrm{J\,g^{-1}}$ for melting and $\Delta h_{f,cryst.} = (256.4 \pm 1.0)\,\mathrm{J\,g^{-1}}$ for crystallisation. The mean value of the latter is $\Delta h_f = (255.9 \pm 1.5)\,\mathrm{J\,g^{-1}}$. Figure 25 depicts the mass dependency of the specific heat of fusion for samples with a purity of 99.5+%. Again latent heats determined upon melting and crystallising deviate less than 1% from each other. As a mean value we obtain $\Delta h_f = (263.6 \pm 1.1)\,\mathrm{J\,g^{-1}}$.

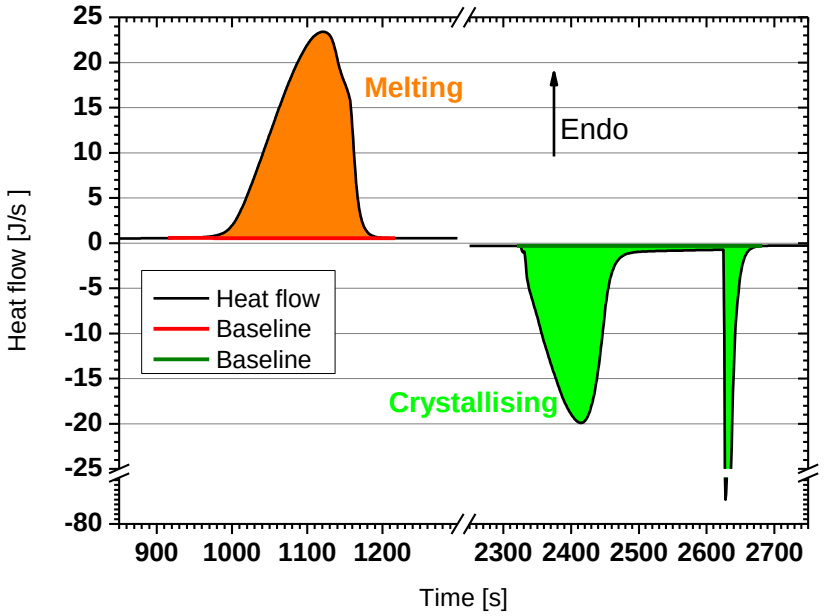

Figure 23: Melting in orange and crystallising in green of a C20 sample with a mass of m=9.19mg and purity of 99.5+%. For both peaks the underlying heating or cooling rate is 1K/min. The black line indicates the measured heat flow. The integrated surface is indicated by the colored area, the base lines (red and dark green) are chosen to be an extrapolation of the liquid phase.

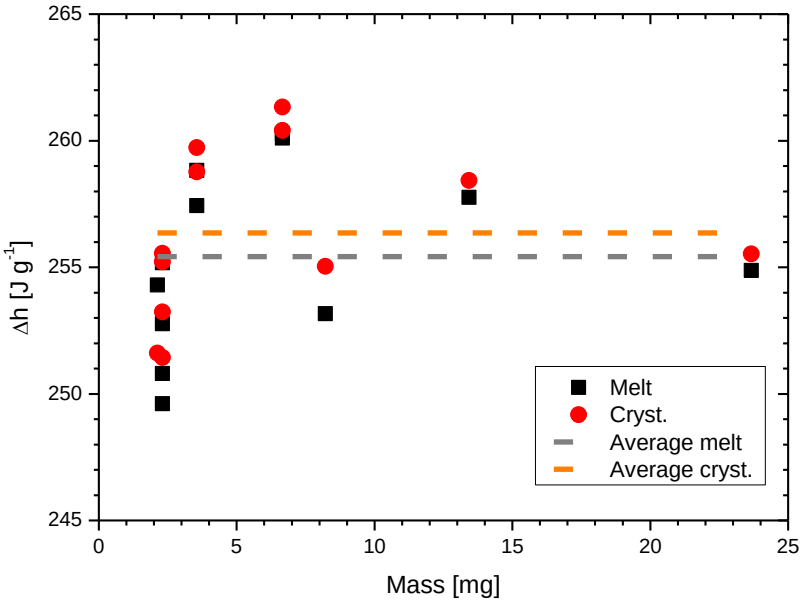

Figure 24: Specific melting and crystallisation enthalpies for different samples of C20 with purity of 99.0+%.

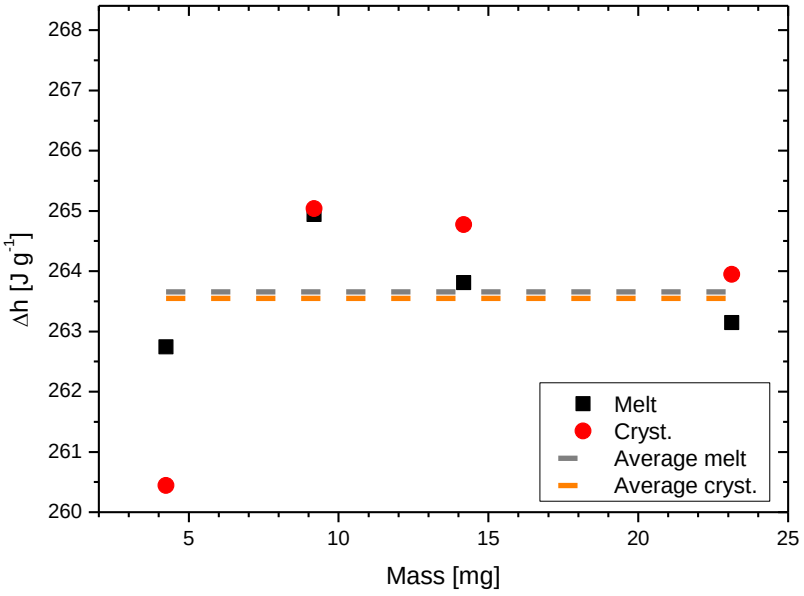

Figure 25: Specific melting and crystallisation enthalpies for different samples of C20 with purity of 99.5+%.

Table 2: Literature values for heat of fusion of C20

Heat of fusion Δh_f in J g^{-1}	Reference
245.2	Schaerer et al. [51]
245.8	Small [6]
247.5	Van Miltenburg et al. [52]
246.2 ± 1.0	Average

Table 2 allows for comparing literature values for the specific heat of fusion of C20 to those determined in the present work. While Δh_f obtained for the 99.0+% samples is 4% above the literature values, the specific heat of fusion determined for the 99.5+% samples is 7% higher. These deviations range in the interval of inaccuracy extending from ±5% to ±8% for a heat flux DSC[53,54]. This on the other side allows no final conclusion regarding trends imposed on the specific heat of fusion by increasing mass or sample purity. To have more reliable data adiabatic calorimetry should be employed.

IV.2. Isothermal step experiments (DSC)

Isothermal step experiments as those described in section IV.1.1 for the investigation of the final melting temperature were performed in the rotator phase.. First an experiment with one sided steps is considered. In a second part a triple step sequence is used to check for reversibility. Last the relaxing part of the heat flux is described by an exponential decay and the corresponding relaxation time is investigated.

IV.2.1. One sided steps

Figure 26 shows he temperature profile for the first series of experiments. The temperature is first reduced from 313.15 K to 308.15 K. Then it is stepwise increased every 30 minutes by 0.1 K to finally reach 309.75 K. The experiment finishes with two additional isotherms at 313.15 K and 293.15 K. The measured temperature shows slight overshoots at the steps.

In figure 27 the corresponding heat flux response is shown. With rising temperature the amplitude of the heat flux peaks (identified by red arrows) increases. Moreover it can easily be observed, that the time until the baseline is reached gets larger. The dark blue arrow indicates the last heat flux peak which shows higher amplitude than a regular peak in the liquid phase (light blue arrow). To assess the enthalpy (not to confuse with enthalpy of fusion) of C20 in the rotator phase, the baseline of the heat flux must be subtracted from the total signal. Our approach to determine the baseline of the heat flux in the rotator phase consists in linearly extrapolate the baselines corresponding to the liquid and triclinic phases. The enthalpy could then be calculated by an appropriate time integral over the “net” heat flux. The specific

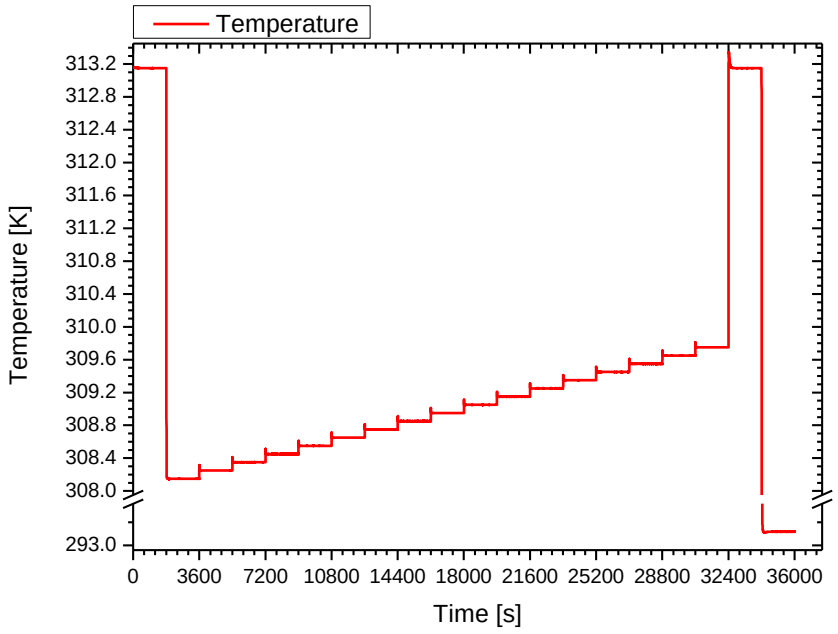

Figure 26: Temperature profile for one sided isothermal step experiment.

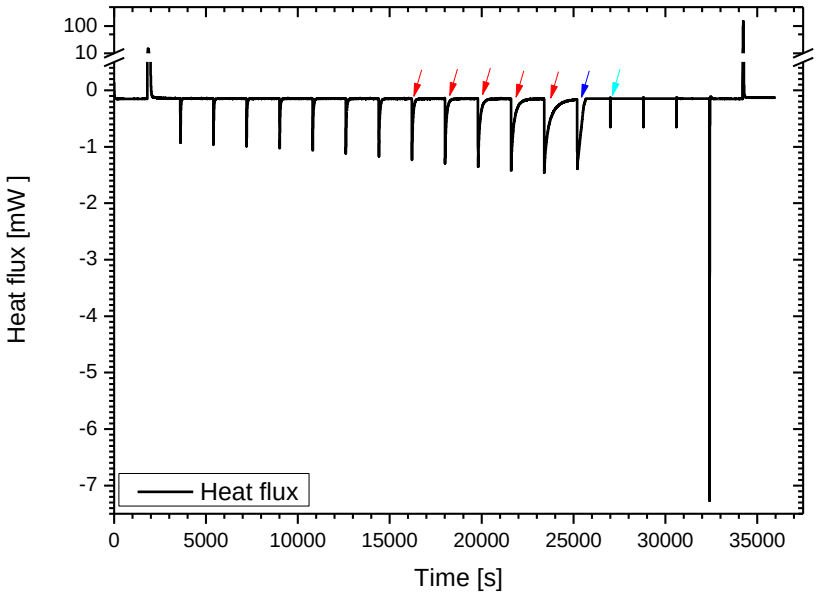

Figure 27: Heat flux over time for a step experiment (temperature profile see Figure 26). A C20 sample with mass m = 8.5mg and purity 99.0+% was used.

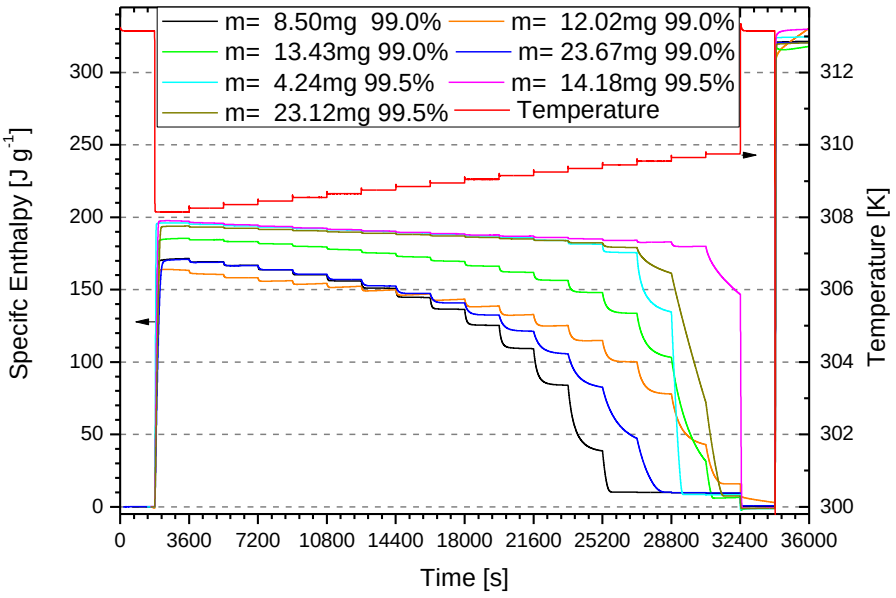

Figure 28: Specific enthalpy over time for a step experiment for samples of different mass and purity (indicated in the legend)

enthalpy is obtained by subsequent division of the enthalpy by the sample's mass.

Figure 28 shows the time evolution of the specific enthalpy of C20 samples with different masses and purities. It has to be stressed that the represented specific enthalpy comprises heat capacity and latent heat contributions. First we note that the samples of higher purity show larger values for the enthalpy and tend to melt at higher temperatures than the majority of the low purity samples. The high purity samples exhibit fewer specific enthalpy-steps with long relaxation times. The melting steps are clearly visible as they show a constant slope in the specific enthalpy which means that their heat flux (or temperature difference to the reference) does not relax to zero. For both purities there seems to be no trend with mass. The overall deviation of the final melting isotherm can rather be associated with the placement of the crucible in the DSC and will be further discussed later in this section. To corroborate this argument in figure 29 shifted curves of figure 28 is presented so that the final melting isotherms for each measurement coincide. Except the sample with mass m=13.43mg and purity 99.0+%, all of the investigated samples exhibit purity-specific behaviour.

Another aspect which can be noted is that for the last few isotherms in the rotator phase the baseline corresponding to a fully relaxed state of the sample is not necessarily reached (see for example figure 30). This is nevertheless uncertain as a drift like the one between two measurements as the one depicted in figure 30 could yield similar results. In this case the construction of the baseline is ambiguous. Nevertheless as the enthalpy measured between the different temperature steps is considerable, the drift influences the overall specific enthalpy only marginally. This can be seen in figure 31 where the same step experiment was performed in a row. Only close to the last isotherms within the rotator phase deviations appear.

Figure 32 depicts two measurements with different crystallization histories. For the first run, crystallization is realized by means of successive temperature steps yielding a fast rate around $\beta = -28$ K/min. The second temperature program is linear with a slow rate around $\beta = -0.1\bar{6}$ K/min. As the growth of the crystallites is not instantaneous one could expect different nucleation scenarios for these two measurements. The nucleation should still be heterogeneous as homogeneous nucleation would appear at much lower temperatures [55,56]. From an inspection of figure 32 we learn that obviously the kinetics controlling the approach of the first isothermal in the rotator phase seem to have no impact on the evolution of the specific enthalpy for the rest of the experiment.

Figure 33 shows the time evolution of the specific enthalpy obtained from two measurements using the same C20 sample with mass m = 12.02mg and purity 99.0+%. Between the two measurements other samples were investigated so that the crucible with the 12.02 mg sample is positioned in another way in the DSC. We observe that the final melting isotherm is shifted by 0.2K when switching from the first position of the sample to the second. This suggests that the real temperature of the sample might depend on the position of the crucible. This finding is especially

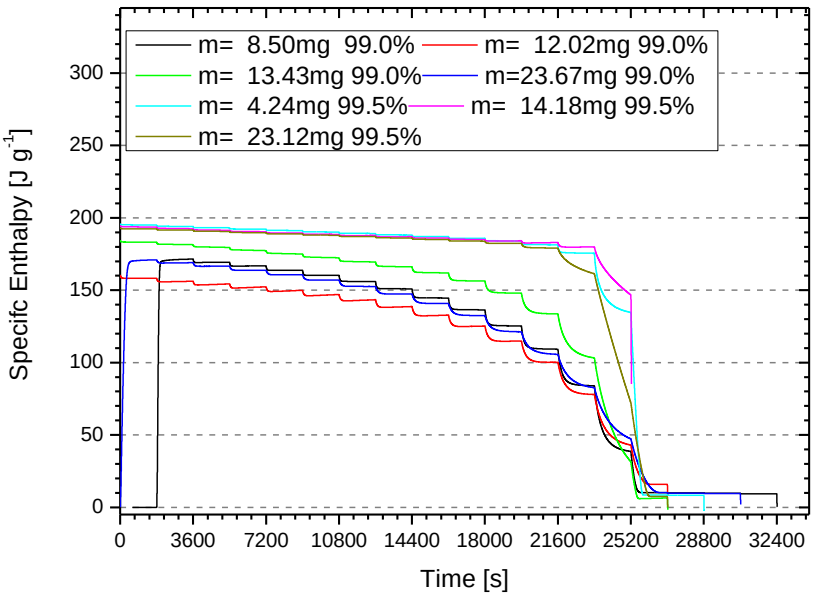

Figure 29: Time shifted data of figure 28 so that the final melting isotherms coincide.

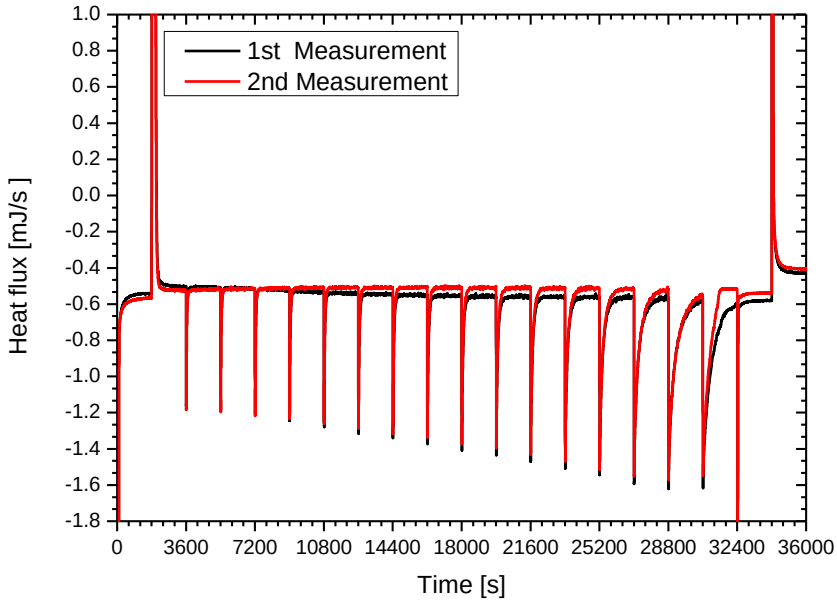

Figure 30: Heat flux over time for two identical measurements . Baseline-shift related to drift.

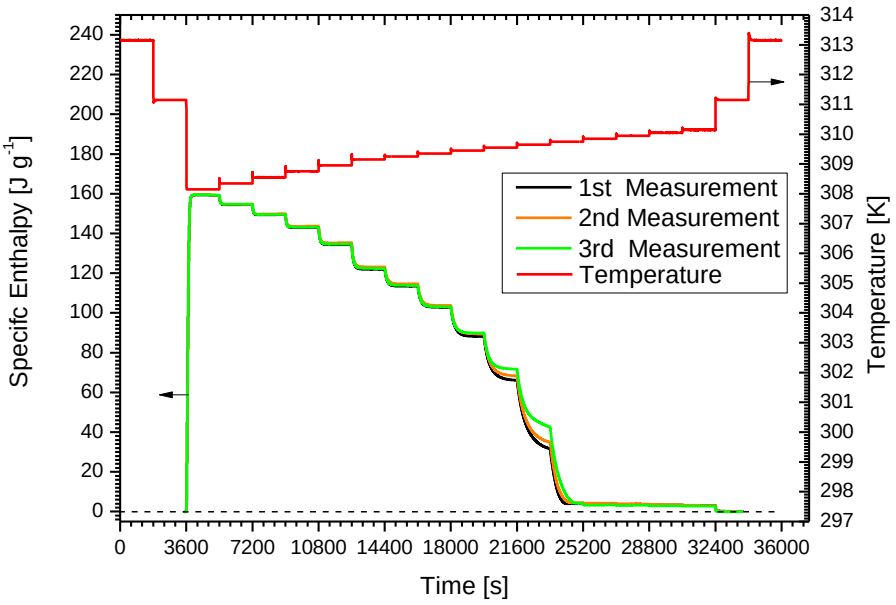

Figure 31: Specific enthalpy for step measurements for a C20 sample with a mass of m=12.02mg and purity 99.0%.

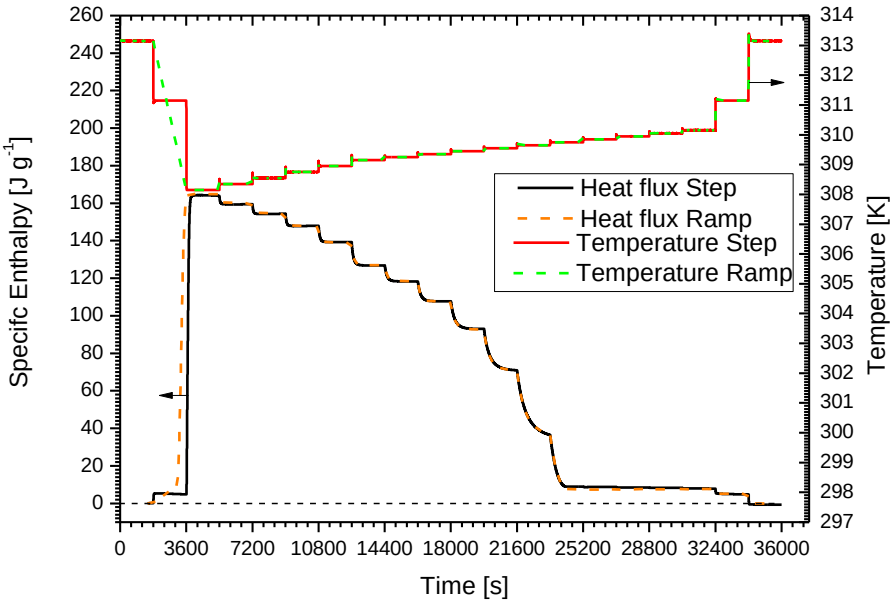

Figure 32: Specific enthalpy for two step experiment with a C20 sample with mass m=12.02mg and purity of 99.0+%. First experiment goes step like into the rotator phase. The second experiment goes with a ramp of 0.16 K/min into the rotator phase.

relevant for the comparison of measurements realized on samples with different masses: the temperature range, where pronounced relaxation and enthalpy can be observed, possibly shifts.

Figure 34 allows for comparing the specific enthalpy evolution when the sample is heated to the liquid state from the rotator phase and from the triclinic phase respectively. At 308.15 K the specific enthalpy of the rotator phase corresponds to around 60% of the specific heat of fusion measured for the triclinic phase. With increasing temperature this ratio then monotonically decreases. When approaching the final isotherm the triclinic phase shows relaxation behaviour subsequent to temperature discontinuities applied before the final isotherm corresponding to the rotator phase. This suggests that the observed relaxation mechanism is not solely related to the rotator phase.

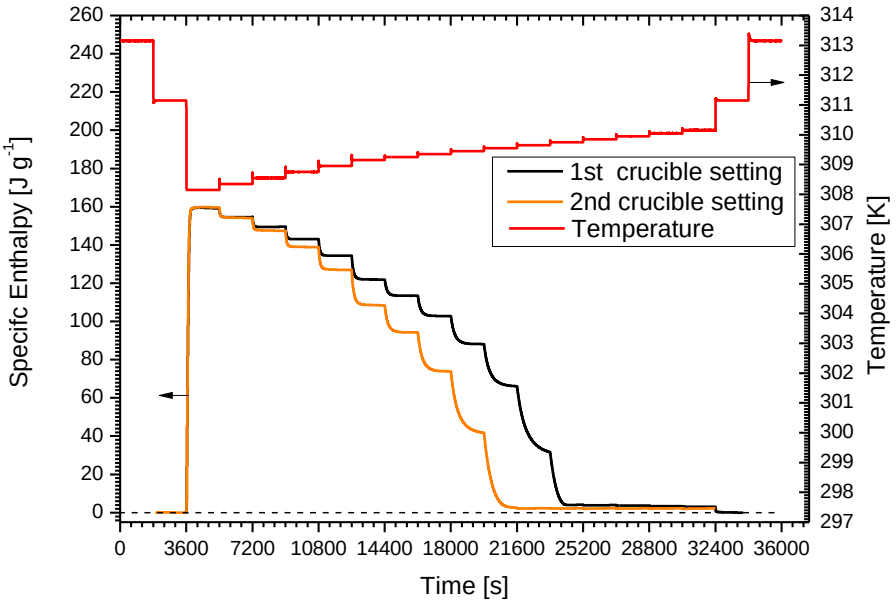

Figure 33: Specific enthalpy for two step experiment with a C20 sample with mass m=12.02mg and purity of 99.0+%. The first experiment show the specific enthalpy for one crucible setting. The second measurement was with the sample put again in the DSC.

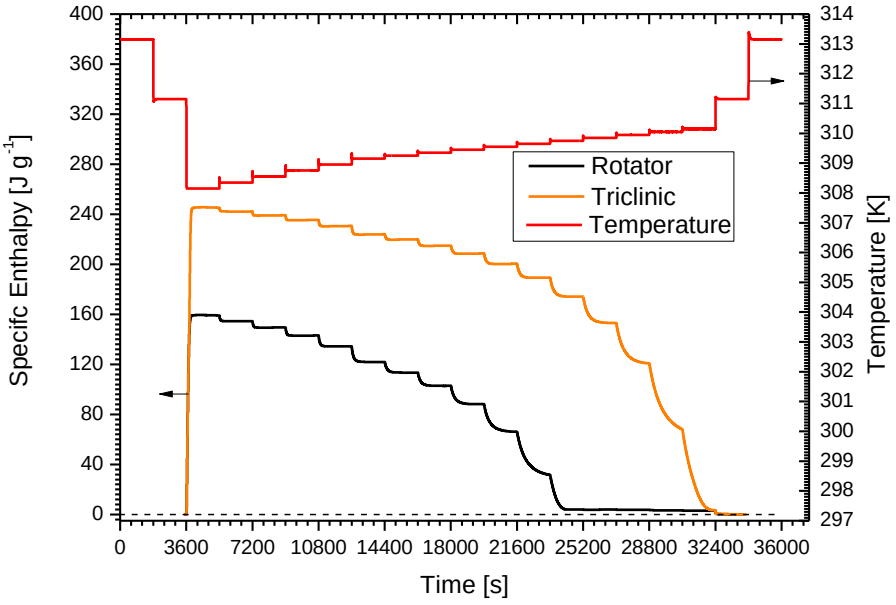

Figure 34: Specific enthalpy for two step experiment with a C20 sample with mass m=12.02mg and purity of 99.0+%. The first experiment show the specific enthalpy for the rotator phase. The second shows the one for the triclinic phase.

IV.2.2. Tri-step experiment

To investigate reversibility tri-step experiments are realized. They consist of an alternating series of three temperature steps followed by isotherms each of duration of 10 minutes. For each sequence of three successive temperature steps two are in the same direction (see figure 35). The temperature profile of the first series of sequences is such that the sample is cooled from 309.25 K to 307.85 K. During a second series the tri-steps within a sequence are inverted: the sample is heated from 307.85 K to 310.25 K. Obviously heating steps show a stronger overshoot than cooling jumps.

Figure 36 shows the time evolution of the enthalpy for different samples of C20. Except for the steps close to the final melting the specific enthalpy goes back to the same value after opposing steps. This hints that the process behind the enthalpy change is reversible. Additionally, steps in the same direction even yield the same temporal evolution of the specific enthalpy. The reversibility excludes any type of nucleation processes with a non-reversible mechanism

For the samples with higher purity the range showing large variation in the specific enthalpy is again narrow. As expected the specific enthalpy is larger for the samples with the highest purity.

The light blue curve in Figure 36 shows a transition to the triclinic phase. Also the triclinic phase for the high purity (99.5+%) samples show some relaxation before melting

.

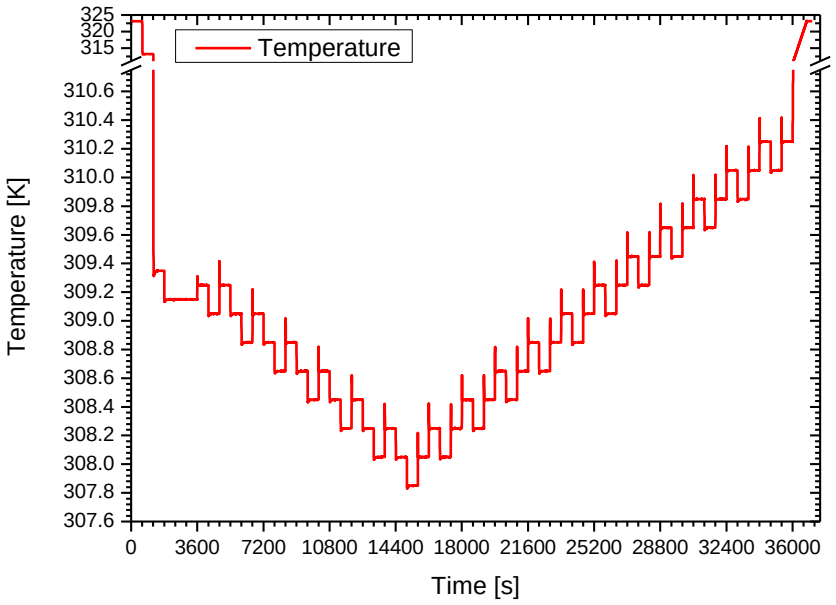

Figure 35: Temperature profile for a tri-step experiment.

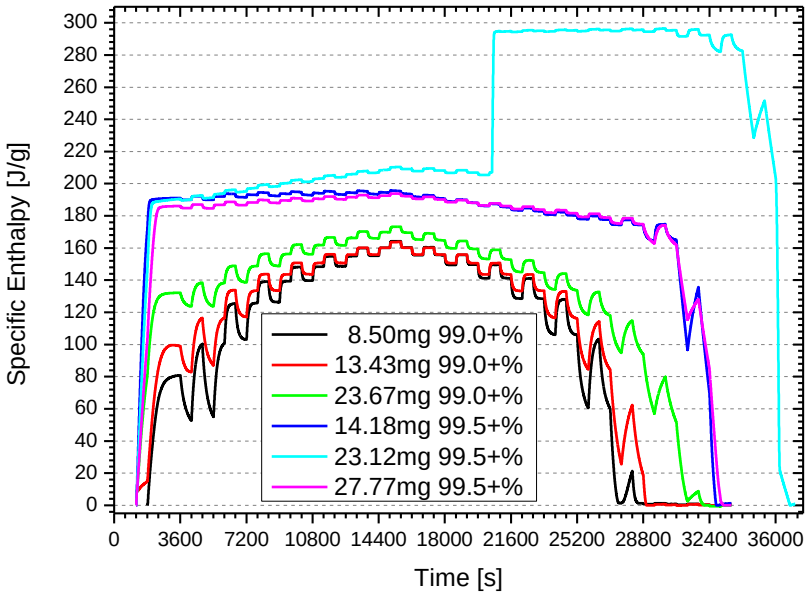

Figure 36: Specific enthalpy for a tri-step experiment for different C20 samples (see legend).

IV.2.3. Relaxation times for the step experiments

Similar to the heat pulse response discussed in the last part of section II.1.1 the heat flux response to a temperature step can be described by a double exponential function. For the C20 samples the right hand side of the heat flux peaks is the one which shows variation with increasing temperature. We assume that the internal thermal resistances and heat capacities of the DSC instrument cannot vary considerably in the narrow temperature range extending from 308 K to 311 K. As a matter of fact we do not observe any temperature dependent effect linked to the instrument in the liquid phase of eicosane. As a consequence the long-time behaviour (right hand side of the heat flux peaks) depends on the sample. We have fitted the right hand side of the peaks with a single exponential decay. The influence of the shorter relaxation time (related to thermal resistances of the instrument) is supposed to be negligible beyond the extremum of the peak. Figure 37 shows examples of such fits. The fits work well as long as the heat flux relaxes to the baseline and the transition does not end abruptly. This is e.g. not the case for the last two peaks in the rotator phase in figure 37. So the relaxation times found for the heat flux peaks close to the transition should be considered with care.

Figure 38 depicts the temperature dependence of the relaxation times for low purity samples with different masses for one-side step experiments. The relaxation times associated to the rotator phase increase with growing temperature until a maximum is reached. At higher temperatures (liquid phase) the relaxation times drop down to several seconds. The spread of relaxation times along the temperature scale corresponds to the one observed for the melting isotherms in figure 28.

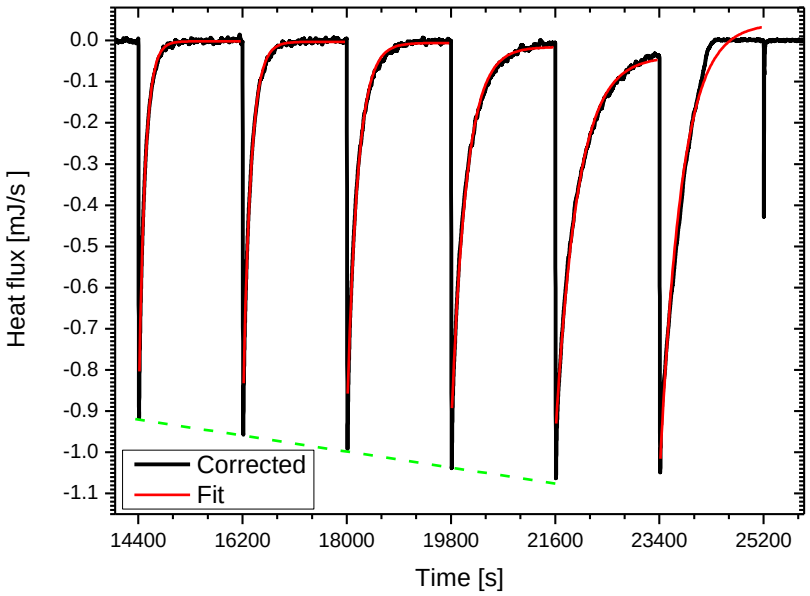

Figure 37: Example of a exponential decay fits on the right hand side of a heat flux peaks. The heat flux is baseline corrected. The black line represents the data, the red lines the fits and the dashed green line highlights the increase of the peaks.

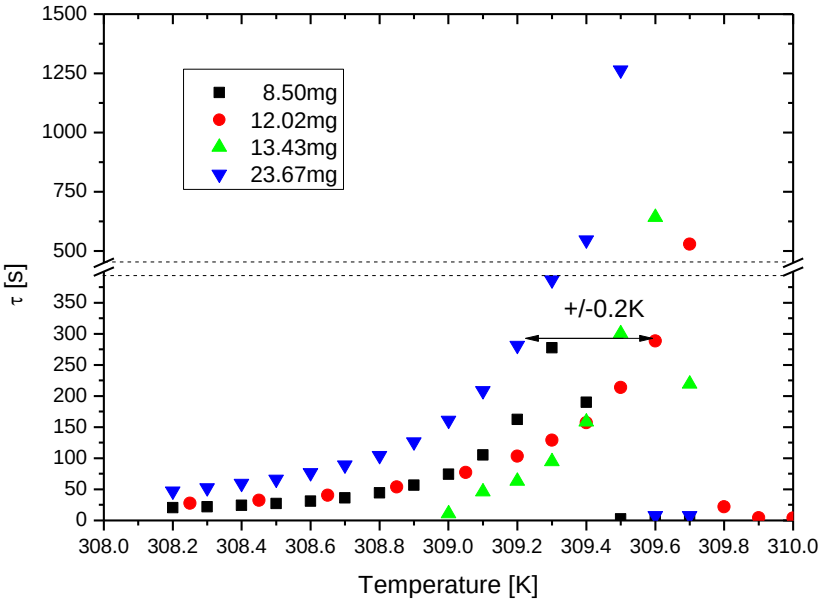

Figure 38: Relaxation times for the one sided step experiments for C20 sample of low purity (mass indicated in legend).

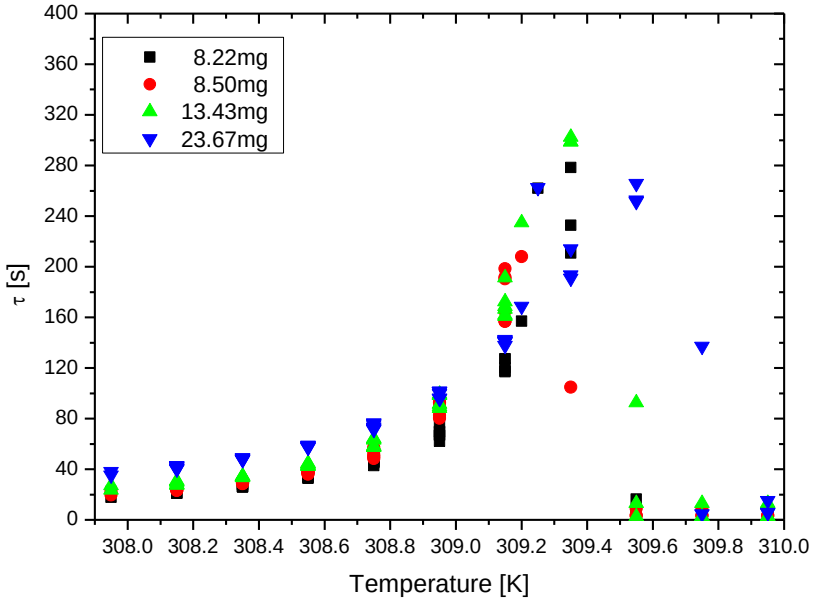

Figure 39: Relaxation times for the tri-step experiments for C20 sample of low purity (mass indicated in legend).

As can be seen in figure 39, the relaxation times obtained from tri-step experiments show a similar temperature behaviour as the one depicted in figure 38 (deduced from one-sided step experiments). No significant difference between heating or cooling step regarding the relaxing behaviour can be observed.

The relaxation times for the 13.43 mg and 23.67 mg samples show opposite behaviour between figure 38 and figure 39. The deviation along the temperature axis corresponds to some extend to those observed for the specific enthalpy in section IV.2.1. This is therefore also attributed to the position of the crucibles.

The relaxation times for the high purity samples were not depicted here as the range for the recognisable relaxation was too short to proper analyse. This will therefore only be discussed in the context of the TOPEM experiments (which allows a more precise investigation).

IV.3. Complex (apparent) heat capacity

IV.3.1. Measuring and evaluation parameters

In appendix B the different parameters relevant for a TOPEM measurement are investigated. Their influence on the acquisition of the quasi-static apparent specific heat capacity c_{p0} and the relaxation times is investigated. For the subsequent measurements the following parameters are used if not indicated otherwise:

- Amplitude a = 0.25 K
- Pulse length $\Delta t_p = 40..60$ s
- Underlying heating rate $\beta_u = 0.02$ K/min
- Starting temperature $T_s = 40$ K
- Evaluation window w = 180s
- No smoothing window

Here it should also be mentioned that no phase correction has been employed. This correction is normally used to compensate for the lag time due to thermal resistances in the DSC sample system [57,58]. It is normally used for glass transitions or crystallisation processes in polymers[59]. In our case on the one hand we do not have enough information on the heat conduction in the rotator phase to use such a correction and on the other hand the relaxing processes are on a much larger timescale so that the correction becomes insignificant, which will be shown later on.

IV.3.2. The quasi-static specific heat capacity at high and low temperatures.

To check the reliability of the results obtained from TOPEM for the quasi-static specific heat capacity c_{p0}, we first compare our data for the liquid and triclinic phases of C20 to literature values. For this purpose we consider the specific heat capacity values from the work of van Miltenburg et al. [52]. The authors used adiabatic calorimetry. It has to be stressed that in the work of van Miltenburg et al., the c_p values in the temperature range between 295 K and 309.65 K correspond to a linear extrapolation of the the c_p data measured in the crystalline phase between 230 K and 295 K.

Figure 40 to figure 43 represent the temperature dependencies of the specific heat capacity for C20 samples for different masses and purities (specified in the figures). All of the measurements were carried out with a cooling/heating rate of $\beta_u = 0.2$ K/min and in a temperature range from 273.15 K to 333.15 K (exception: in figure 42 the temperature range extends from 253.15 K to 353.15 K).

The results obtained on the various samples deviate from the literature values. While the c_{p0} values shown in figure 40, figure 41 and figure 43 are larger than the literature data, those depicted in figure 42 are lower.

To assess the deviations two types of correction are tested. The first one is a correction where the data is multiplied by the ratio literature value at 320 K to measured value at 320 K:

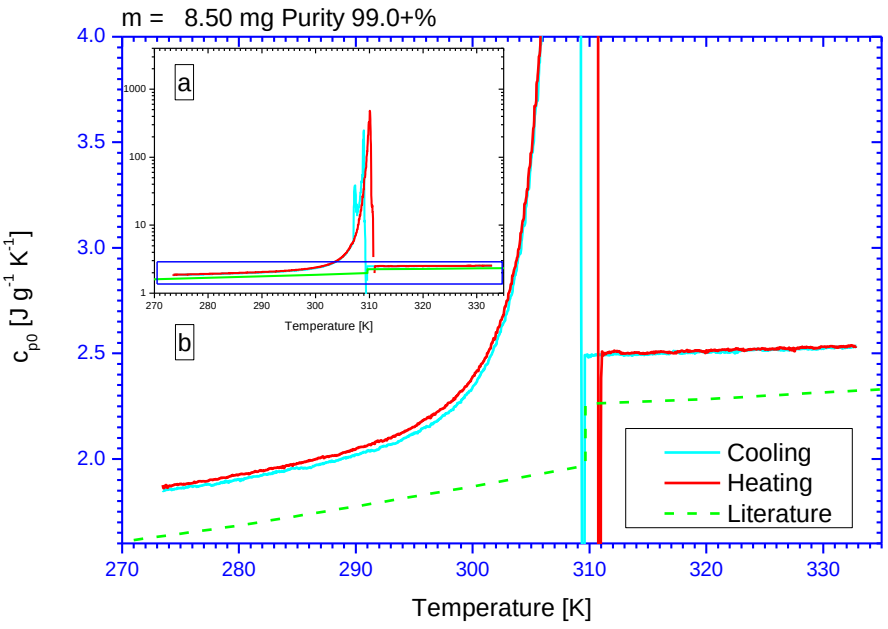

Figure 40: Quasi static heat capacity c_{p0} for a C20 sample with mass m = 8.5 mg and purity 99.0+%. The cooling and heating rate was set to $\beta_u = 0.2$ K/min. The light blue and red lines depict the cooling and heating part respectively. Literature values (dashed green line) are taken from van Miltenburg et al. [52]. a: The whole data range, blue square indicates zoom depicted in b.

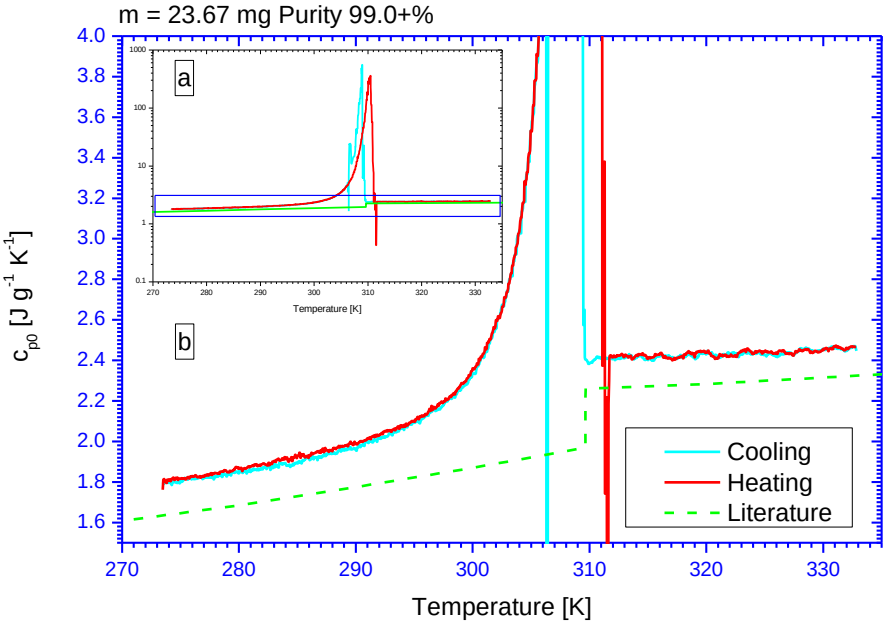

Figure 41: Quasi static heat capacity c_{p0} for a C20 sample with mass m = 23.67 mg and purity 99.0+%. The cooling and heating rate was set to $\beta_u = 0.2$ K/min. The light blue and red lines depict the cooling and heating part respectively. Literature values (dashed green line) are taken from van Miltenburg et al. [52]. a: The whole data range, blue square indicates zoom depicted in b.

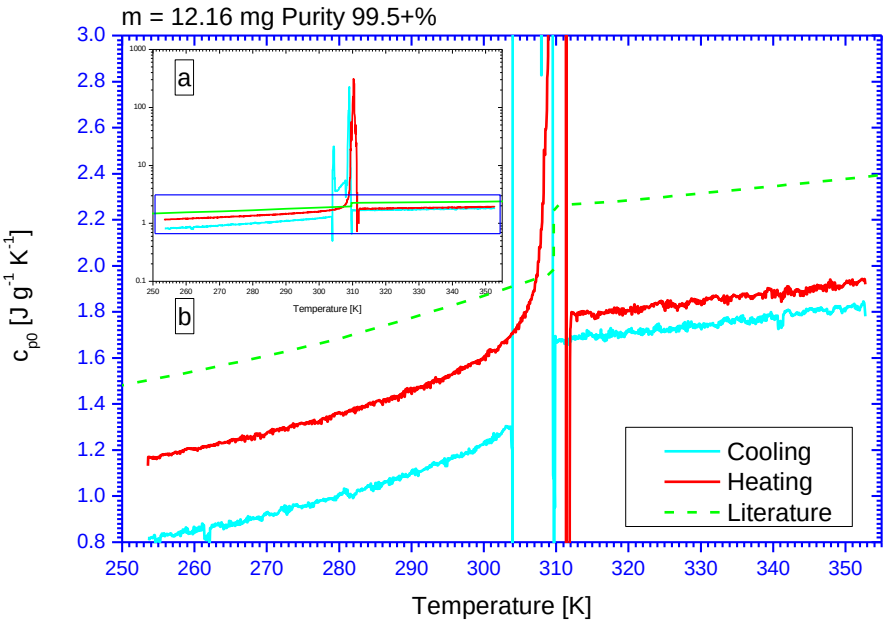

Figure 42: Quasi static heat capacity c_{p0} for a C20 sample with mass m = 12.16 mg and purity 99.5+%. The cooling and heating rate was set to $\beta_u = 0.25$ K/min. The light blue and red lines depict the cooling and heating part respectively. Literature values (dashed green line) are taken from van Miltenburg et al. [52]. a: The whole data range, blue square indicates zoom depicted in b.

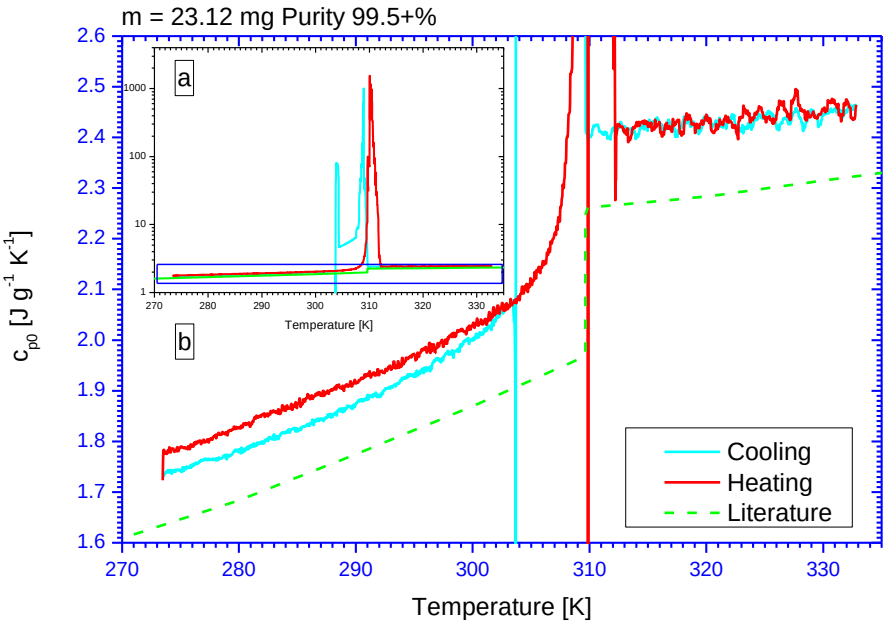

Figure 43: Quasi static heat capacity c_{p0} for a C20 sample with mass m = 23.12 mg and purity 99.5+%. The cooling and heating rate was set to $\beta_u = 0.2$ K/min. The light blue and red lines depict the cooling and heating part respectively. Literature values (dashed green line) are taken from van Miltenburg et al. [52]. a: The whole data range, blue square indicates zoom depicted in b.

$$c_{p0}^{Prop.}(T) = c_{p0}(T) \cdot \frac{c_{p0,Lit}(T = 320\text{K})}{c_{p0}(T = 320\text{K})} \qquad \text{(IV.2)}$$

This correction accounts for an error in the calibration of the heat flux.

The second type of correction is an additive one

$$c_{p0}^{Add.}(T) = c_{p0}(T) + \left(c_{p0,Lit}(T = 320\text{K}) - c_{p0}(T = 320\text{K})\right) \qquad \text{(IV.3)}$$

where, at each temperature, the difference between literature and measured data at 320 K is added to the measured data. Here the deviation between measured and literature data is treated as an additional heat capacity of the system which is not compensated by the TOPEM evaluation algorithm.

Figure 44 to figure 47 allow for comparing the results yielded by the two types of correction. Obviously the "additive" type of correction generally delivers a better coincidence between literature and measured data in the liquid and triclinic phases of the various C20 samples. Because of the additive character of the correction its impact on the apparent heat capacity in the rotator phase is low.

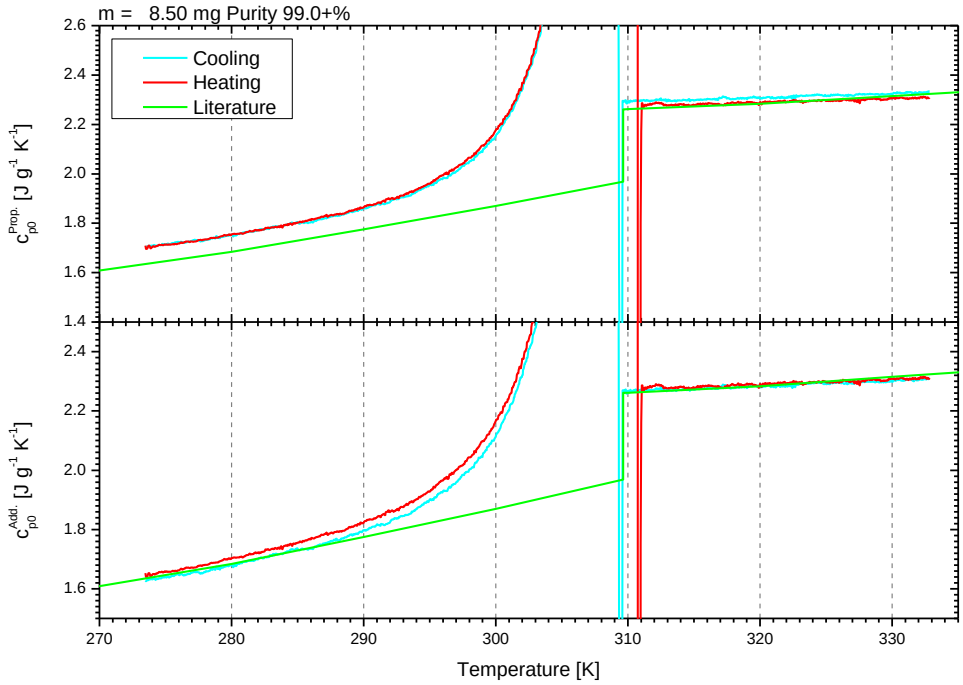

Figure 44: Corrected quasi static heat capacity $c_{p0}^{Prop.}$ (top) and $c_{p0}^{Add.}$ (bottom) for a C20 sample with mass *m* = 8.5 mg and purity 99.0+%. The cooling and heating rate was set to $\beta_u = 0.2$ K/min. The light blue and red lines depict the cooling and heating part respectively. Literature values (dashed green line) are taken from van Miltenburg et al. [52].

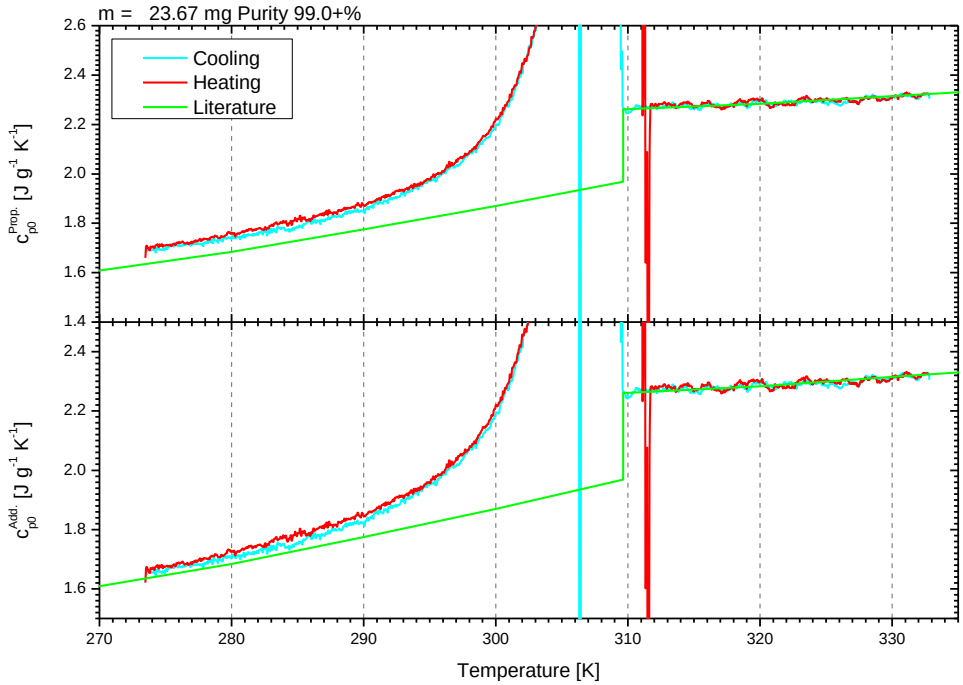

Figure 45: Corrected quasi static heat capacity $c_{p0}^{Prop.}$ (top) and $c_{p0}^{Add.}$ (bottom) for a C20 sample with mass *m* = 23.67 mg and purity 99.0+%. The cooling and heating rate was set to $\beta_u = 0.2$ K/min. The light blue and red lines depict the cooling and heating part respectively. Literature values (dashed green line) are taken from van Miltenburg et al. [52].

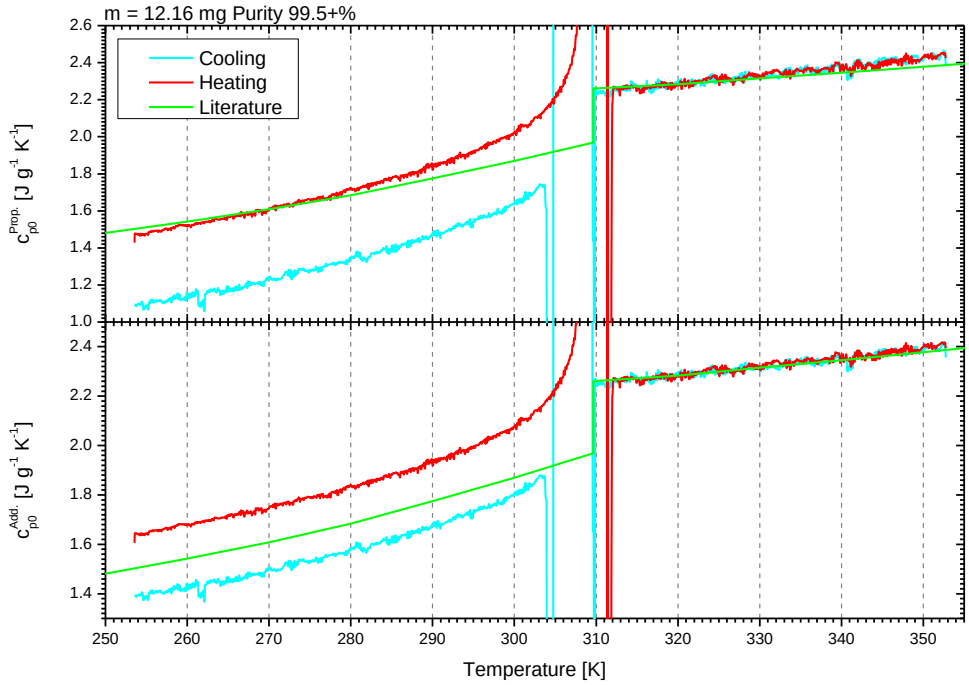

Figure 46: Corrected quasi static heat capacity $c_{p0}^{Prop.}$ (top) and $c_{p0}^{Add.}$ (bottom) for a C20 sample with mass *m* = 12.16 mg and purity 99.5+%. The cooling and heating rate was set to $\beta_u = 0.25$ K/min. The light blue and red lines depict the cooling and heating part respectively. Literature values (dashed green line) are taken from van Miltenburg et al. [52].

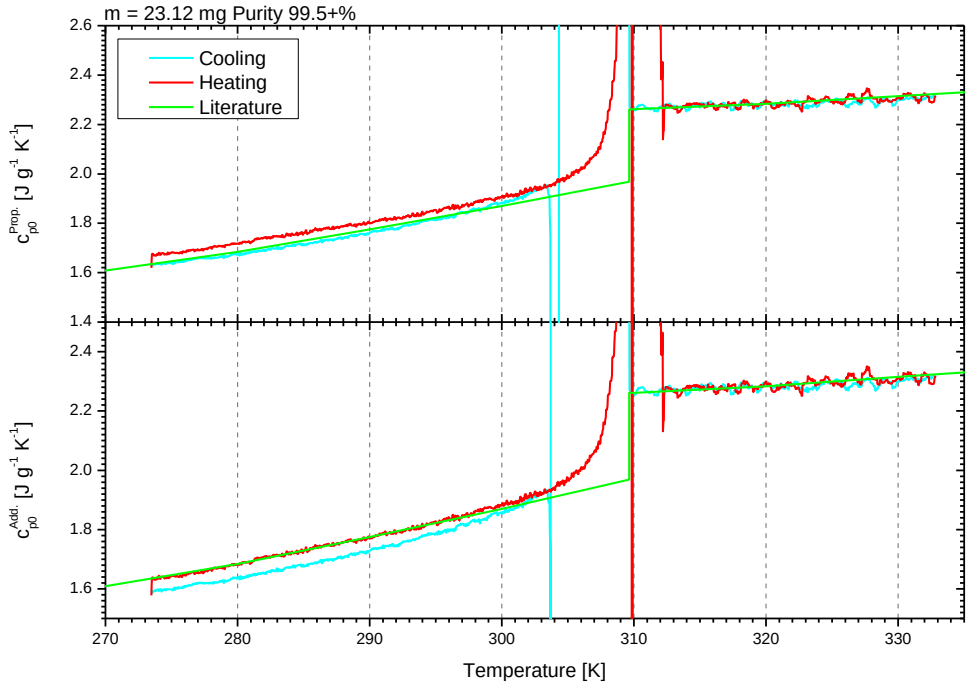

Figure 47: Corrected quasi static heat capacity $c_{p0}^{Prop.}$ (top) and $c_{p0}^{Add.}$ (bottom) for a C20 sample with mass *m* = 23.12 mg and purity 99.5+%. The cooling and heating rate was set to $\beta_u = 0.2$ K/min. The light blue and red lines depict the cooling and heating part respectively. Literature values (dashed green line) are taken from van Miltenburg et al. [52].

From the following measurements (next section) the deviations from the literature values were also calculated. As these experiments only went up to 313.15 K, the offset deviation was taken at 310 K. Figure 48 illustrates the deviations of measured data from literature values as a function of the sample mass. The deviations have been calculated at T =310 K. While the literature values are taken from Miltenburg et al.[37], the measured data stem from tests shown in figure 49 to figure 51 and figure 53 to figure 56. It can be observed that most of the deviations scatter around 10%. The result obtained for the sample with the smallest mass (m = 4.24 mg) represents an exception to the general trend. There seems to be no dependency on the purity of the samples

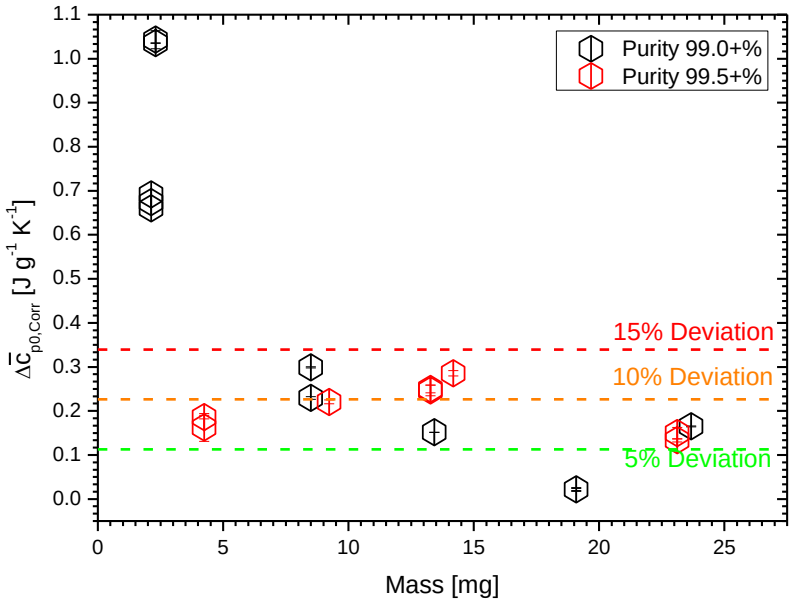

Figure 48: Deviation at 310 K of the heat capacity from measurements and literature for C20 samples with different mass and purities.

IV.3.3. The quasi-static specific heat capacity close to the transitions

Figure 49 shows the temperature dependencies of the quasi-static specific heat capacity obtained for C20 samples (low purity : 99.0%+) for different masses upon cooling. The data have been corrected ("additive" type of correction) as described in the previous section. We account for the scattering of the temperature at which the rotator phase appears relates to the crucible placement inside the furnace (see section IV.2.1). The heights of the $c_{p,0}^{Add}$ – peaks close to the transition to the rotator phase are comparable. For two of the samples we observe the transition from the rotator phase to the triclinic phase (indicated by arrows). The step between the rotator phase and the triclinic phase is in the range of 2-3 J $g^{-1}K^{-1}$. There is empirical evidence that the probability of the RI-T transition occurring at higher temperatures increases with the sample mass. This is the reason why the investigation of the rotator phase could only be extended to lower temperatures for samples with small masses.

Figure 50 depicts the temperature evolution of the corrected quasi-static specific heat capacity for a heating run. Irrespective of the sample mass (purity: 99.0%+) the apparent specific heat capacity strongly increases when approaching the respective final melting temperature.

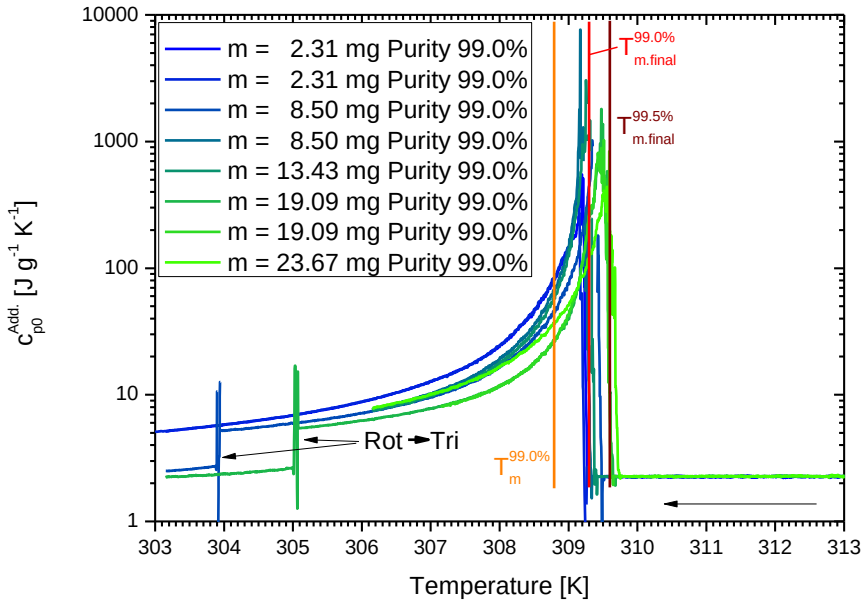

Figure 49: Quasi-static heat capacity for cooling runs of C20 samples with a purity of 99.0+%. Masses are indicated in the legend. The characteristic temperatures for the rotator phase (see section IV.1.1) are indicated as vertical lines.

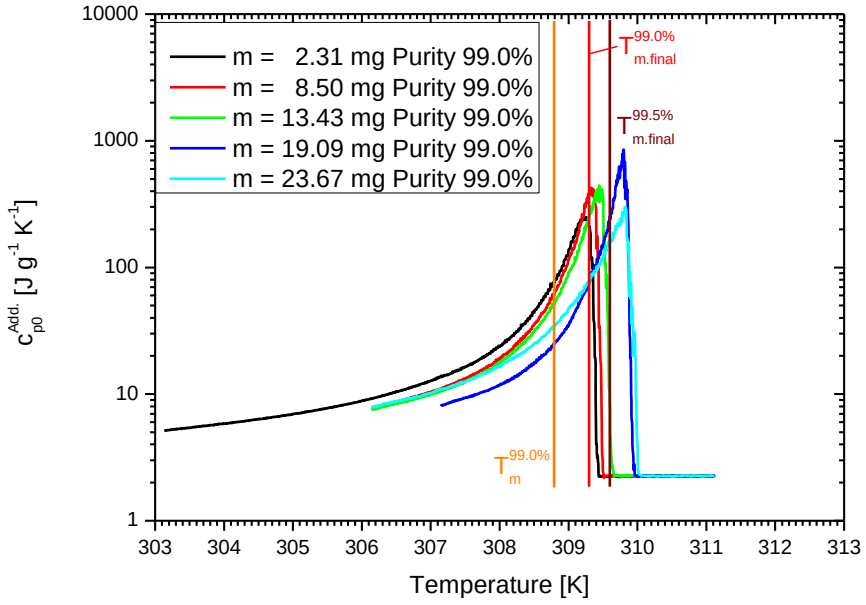

Figure 50: Quasi-static heat capacity for heating runs of C20 samples in the rotator phase with a purity of 99.0+%. Masses are indicated in the legend. The characteristic temperatures for the rotator phase (see section IV.1.1) are indicated as vertical lines.

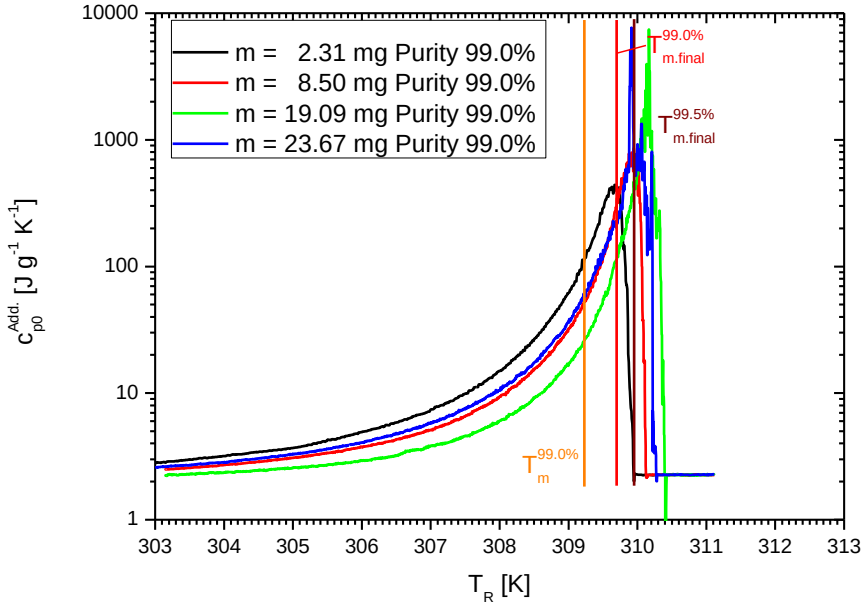

Figure 51: Quasi-static heat capacity for heating runs of C20 samples in the triclinic phase with a purity of 99.0+%. Masses are indicated in the legend. The characteristic temperatures for the triclinic phase (see section IV.1.1) are indicated as vertical lines.

Figure 51 illustrates the behaviour of the corrected specific heat capacity when the triclinic phase is heated up to the T-L transition temperature. Again an important increase of the specific heat capacity can be noted when the transition temperature is approached.

Relying on the hypothesis that the scattering of the temperatures corresponding to the maxima of the $c_{p,0}^{Add}$ – peaks is due to the crucible position of the crucibles in the furnace the the $c_{p,0}^{Add}$(T) curves can be shifted along the temperature axis to coincide (see figure 29) An example is displayed in figure 52 for a C20 sample with mass *m* = 23.67mg and purity 99.0+%. A shift along the temperature axis by -2.2 K lets the two measurements coincide (see green dashed line).

For the samples with higher purity (99.5+%) the temperature evolutions of the quasi-static corrected apparent specific heat capacity are shown in figure 53 to figure 55. Figure 53 shows the results obtained for samples with different masses upon cooling. For most of the samples crystallization starts at temperatures which are not too far off the final melting temperature of the rotator phase. In literature [60] the closeness of the melting and crystallisation temperatures is attributed to heterogeneous nucleation. Compared to the results obtained for the samples with lower purity (see figure 49), the decrease of the apparent specific heat capacity in the rotator phase is much sharper. At low temperatures it converges to about 4 J $g^{-1}K^{-1}$. For three of the investigated samples the transition the transition between rotator phase and triclinic phase occurred within the temperature range of the

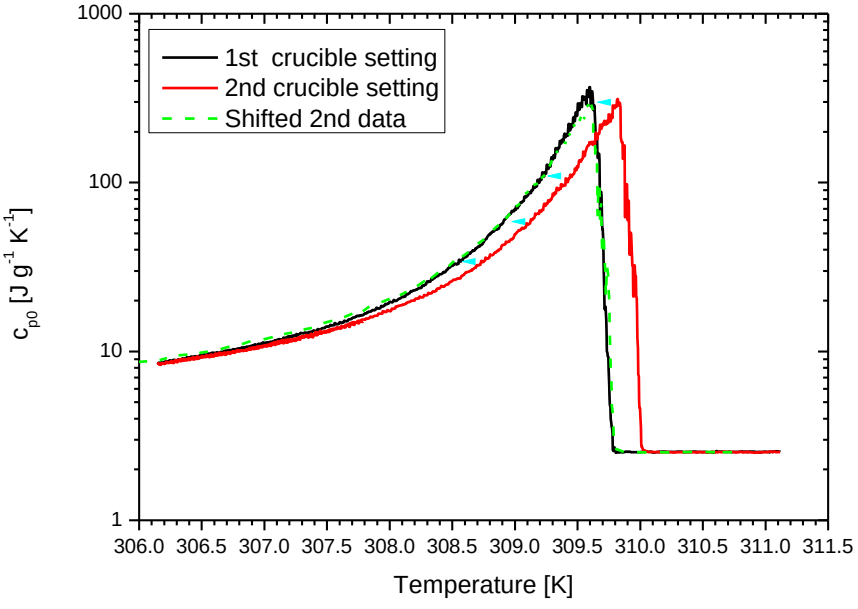

Figure 52: Quasi-static heat capacity for two heating measurements of a C20 sample with mass m=23.67mg and purity 99.0+%. Between 1st (black line) and 2nd (red line) measurement the crucible was removed from the DSC. The a shift of the data of the 2nd measurement by 2.2 K is shown as green dashed line.

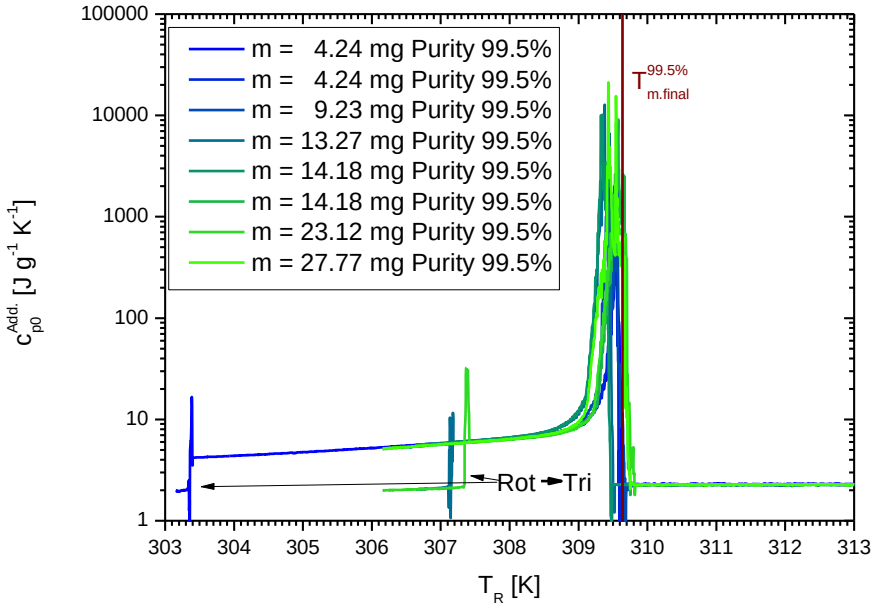

Figure 53: Quasi-static specific heat capacity of C20 samples with a purity of 99.5+% for cooling runs. Masses are indicated in the legend. The characteristic temperatures for the rotator phase (see section IV.1.1) are indicated as vertical lines.

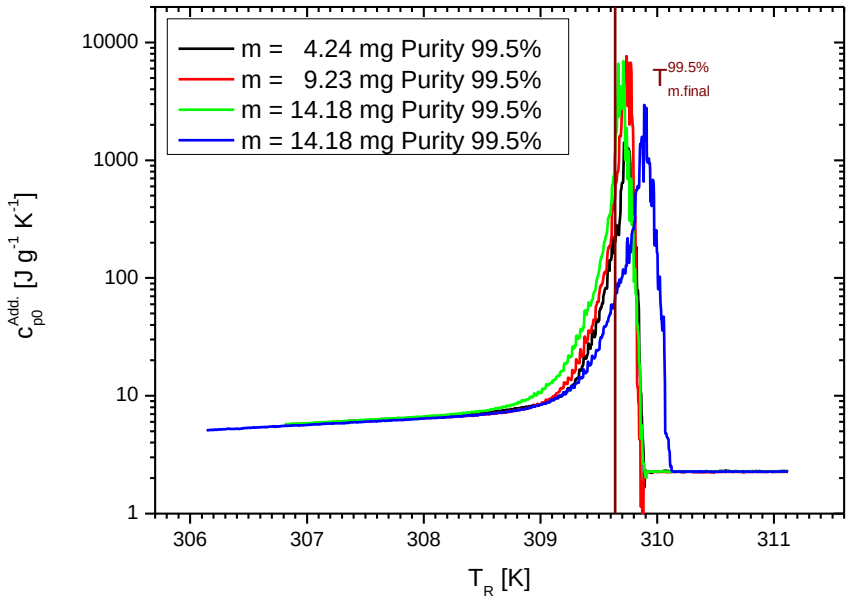

Figure 54: Quasi-static heat capacity of C20 samples in the rotator phase with a purity of 99.5+% for heating runs. Masses are indicated in the legend. The characteristic temperatures for the rotator phase (see section IV.1.1) are indicated as vertical lines.

experiment. At this transition the specific heat capacity of C20 drops by about 2-3 J $g^{-1}K^{-1}$.

For the samples with higher purity the tendency to go to the triclinic phase is more pronounced than in case the samples with lower purity. That is the reason why in figure 54, $c_{p0}^{Add}(T)$ data measured upon heating are missing for samples with masses higher than 14.18mg.

For the melting of the rotator phase the $c_{p0}^{Add}(T)$-curves obtained for the different samples coincide quite well. The maximum in the apparent heat capacity is close to the final melting temperature of the rotator phase determined in section IV.1.1.

The melting behaviour of the triclinic phase is similar to the one observed for the rotator phase (see figure 55). The low temperature values of $c_{p0}^{Add}(T)$ correspond to literature values. At temperatures T>308 K the specific heat capacity starts to strongly increase. In contrast to the observations made for melting of the rotator phase, the peak values of the apparent specific heat capacity $c_{p0}^{Add}(T)$ are no longer sharply defined but rather noisy. This feature will be further elaborated in the discussion (Chapter V).

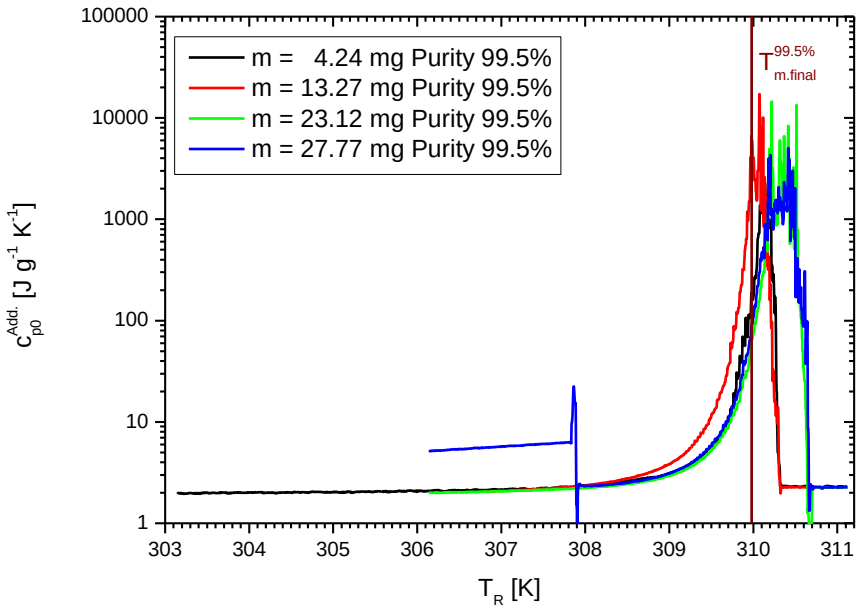

Figure 55: Temperature dependence of the quasi-static specific heat capacity of C20 samples (purity of 99.5+%) while melting the triclinic phase.. Masses are indicated in the legend. The characteristic temperatures for the triclinic phase (see section IV.1.1) are indicated as vertical lines.

IV.3.4. Relaxation times

For the determination of the relaxation times we uses a Debye model (see section II.1.2) yield relaxation times. Figure 56 shows the temperature evolution of the relaxation times for a series of C20 samples with lower purity. The underlying c_{p0}^{add} data stems from cooling runs. In the liquid, triclinic and rotator phase one can see a clear increase of the relaxation times with mass (indicated by vertical arrows in figure 56). This is expected, as the instrumental relaxation time τ depends on the mass *m* and the specific heat capacity c_p (see equation(II.17) e.g.):

$$\tau = R_{eff} \cdot m \cdot c_p \qquad \text{(IV.4)}$$

with $R_{eff.}$ representing the effective thermal resistance (see eq. (IV.5 for more detail). Close to the RI-L transition an important increase of the relaxation times can be observed.

Figure 57 and figure 58 respectively show the temperature dependencies of the relaxations times calculated for the rotator phase and triclinic phase of C20 samples (low purity) upon heating. Again a strong increase of the relaxation times can be observed when the RI-L or T-L transitions are approached. Here again the relaxation times depend on the sample mass (though there is lack of systematics).

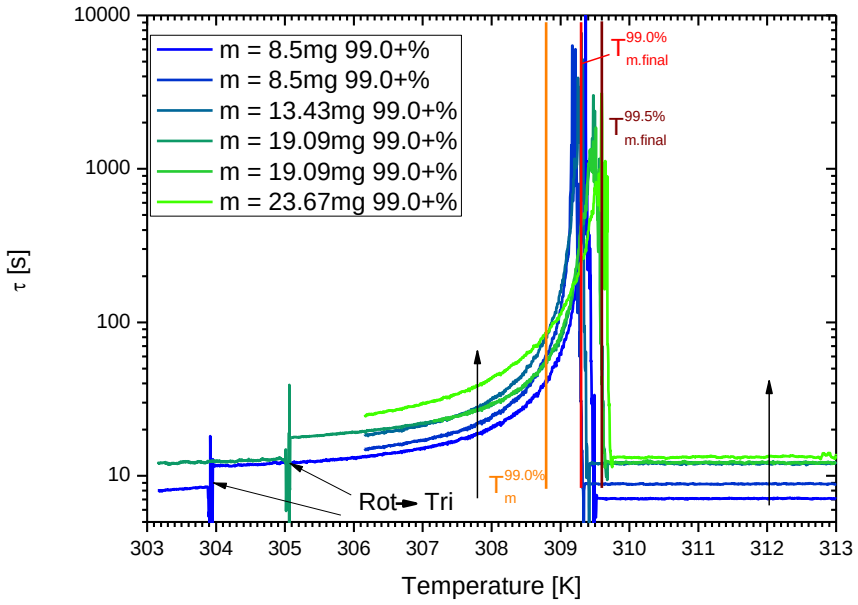

Figure 56: Temperature dependence of the relaxation times for various C20 samples with a purity of 99.0+%. The relaxation times have been obtained from TOPEM measurements realized upon melting the rotator phase. The characteristic temperatures for the rotator phase (see section IV.1.1) are indicated as vertical lines.

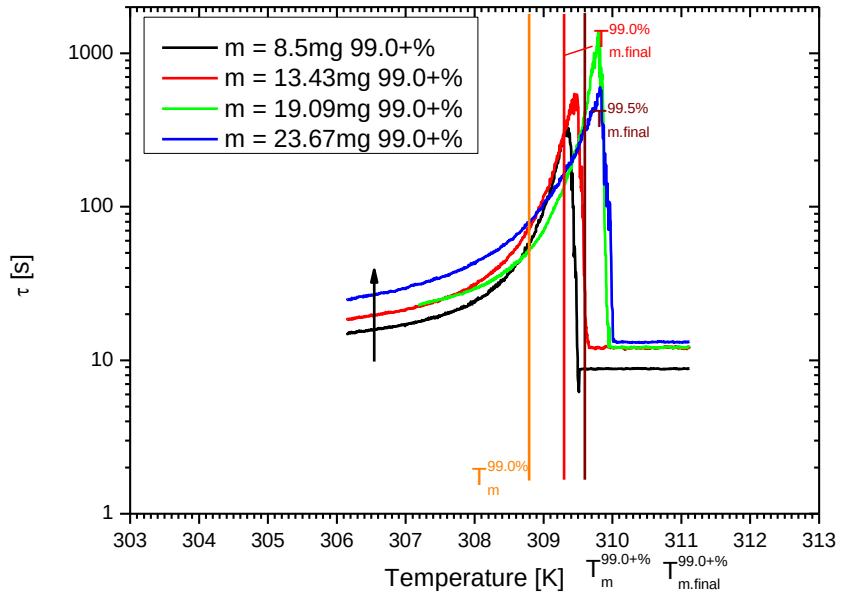

Figure 57: Temperature dependence of the relaxation times for various C20 samples with a purity of 99.0+%. The relaxation times have been obtained from TOPEM measurements realized upon melting the rotator phase. The characteristic temperatures for the rotator phase (see section IV.1.1) are indicated as vertical lines.

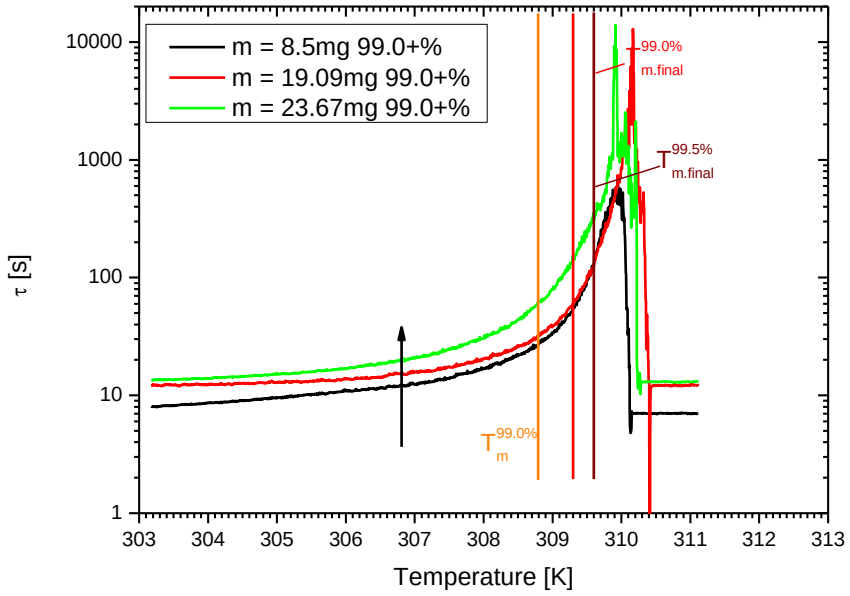

Figure 58 Temperature dependence of the relaxation times for various C20 samples with a purity of 99.0+%. The relaxation times have been obtained from TOPEM measurements realized upon melting the triclinic phase. The characteristic temperatures for the triclinic phase (see section IV.1.1) are indicated as vertical lines.

To identify the process(es) which is/are responsible for the relaxation behaviour we consider the effective thermal resistance R_{eff}. Assuming that the heat capacity of the crucible containing the sample is given by $C_S = C_R + m \cdot c_p$, equation (II.17) can be written as:

$$\Delta\phi^*_{SR,mod} = -\frac{i \cdot \omega \cdot m \cdot c_p}{(1 + i\omega \cdot C_R \cdot R)} \cdot \frac{\Delta T^*_F}{\left(1 + i\omega \cdot m \cdot c_p \cdot R\left(1 + \frac{C_R}{m \cdot c_p}\right)\right)} \quad \text{(IV.5)}$$

Information on the relaxation behaviour is essentially last factor of the right hand side of eq. IV.5. If the sample's heat capacity is much larger than the one of the crucibles $m \cdot c_p \gg C_R$, the relaxation behaviour is dominated by the denominator of the second factor (especially as for the Debye fit the frequency range is cut around $\omega = 0.2s^{-1}$). Thus the effective thermal resistance can be estimated as:

$$R_{eff} = R\left(1 + \frac{C_R}{m \cdot c_p}\right) \quad \text{(IV.6)}$$

For $m \cdot c_p \gg C_R$ the effective thermal resistance converges to $R = K'^{-1}$, i. e. the inverse calibration factor (see section II.1.1). Figure 59 and figure 60 depicts the temperature evolution of the thermal resistance R_{eff} for various C20 samples with different masses and of low purity. R_{eff} is calculated from equation (IV.4) using data measured upon melting the rotator phase.

At any temperature in the liquid phase the effective thermal resistance decreases with increasing mass, as expected. When approaching the transition to the liquid phase R_{eff} is approaching K'^{-1} (independent of sample mass).

Considering a sample with masses between 8.5 mg and 23.67 mg and a specific heat capacity of about 300 J $g^{-1}K^{-1}$, one can estimate that the effective thermal resistance should exceed K'^{-1} by about 2% to 4% (for a crucible mass of 50 mg). However we learn from figure 59 , that upon approaching the RI-L transition, the effective thermal resistance exceeds the inverse calibration factor by 30% to 45%. From this result we conclude that the relaxation times determined from our experiments are longer than those one would expect taking into account only classical "RC – behaviour" of the calorimeter.

At lower temperatures in the rotator phase, the specific heat capacity of the C20 samples drops to much smaller values. As expected the effective thermal resistance R_{eff} depends on the sample mass in the same way as for the liquid phase (figure 59).

Figure 60 shows the temperature evolution of the thermal resistance R_{eff} for C20 samples of low purity upon melting the triclinic phase. Obviously the effective thermal resistance calculated for the triclinic phase exhibits a similar behaviour than the one observed for the melting of the rotator phase (see figure 59). At any temperature in the liquid phase or at low temperatures in the triclinic phase, R_{eff} decreases with increasing sample mass. Close to the transition the effective thermal

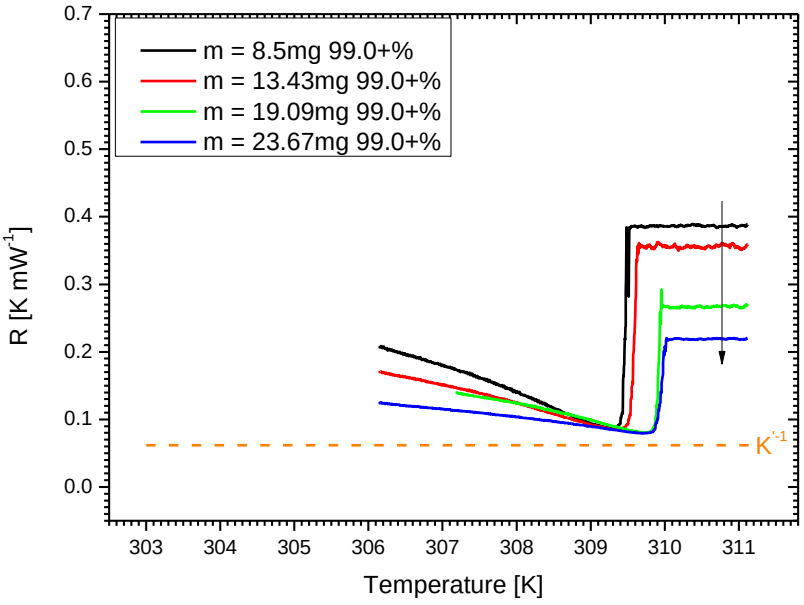

Figure 59: Temperature dependence of the effective thermal resistance for C20 samples with different masses and purity of 99.0+%. R_{eff} is calculated from experimental data measured while melting the rotator phase. The inverse DSC calibration factor *K'* is indicated as orange dashed line.

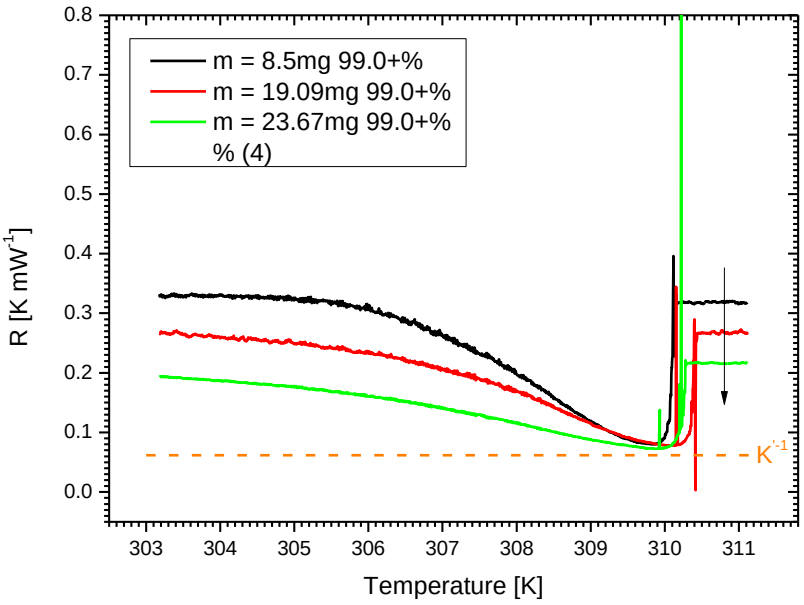

Figure 60: Temperature dependence of the effective thermal resistance for C20 samples with different masses and purity of 99.0+%. R_{eff} is calculated from experimental data measured while melting the triclinic phase. The inverse DSC calibration factor *K'* is indicated as orange dashed line.

resistance no longer depends on the mass and approaches K'^{-1}. The R_{eff} values are of about 15%-20% higher than expected from an RC-behaviour close to the transition.

Figure 61, figure 62 and figure 63 show the temperature evolutions of the relaxation times for C20 samples of higher purity. In figure 61 the data are obtained while cooling the samples from the liquid to the rotator phase. Figure 62 depicts relaxation times determined from calorimetric data while heating in the rotator phase. Finally, in figure 63 we present relaxation times for the melting of the triclinic phase. Generally we find the same behaviour as for the samples with lower purity with the exception that the relaxation time-peak near the liquid/solid transition is much narrower for the high purity systems.

The corresponding evolutions of the effective thermal resistance as a function of temperature (see figure 64 and figure 65) are comparable to the behaviours found for the samples with lower purity behaviour. However it has to be noted that in the vicinity of the phase transition the R_{eff} values come closer to the inverse calibration factor. During the melting of the triclinic phase the behaviour of R_{eff} (T) reaches a plateau value of 10% above K'^{-1}.

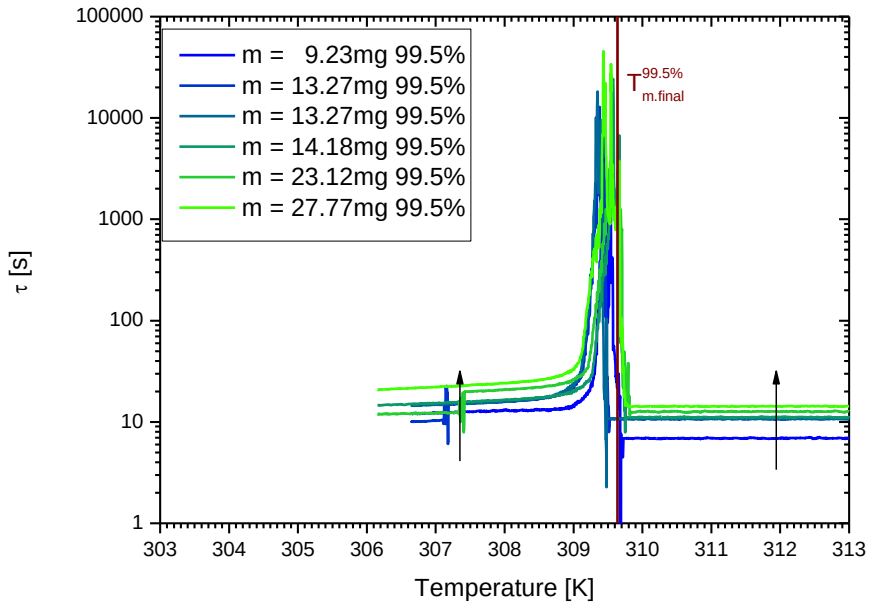

Figure 61: Temperature dependence of the relaxation times of C20 samples with a purity of 99.5+%. The relaxation times are obtained from data determined by TOPEM while melting the rotator phase. The final melting temperature of the rotator phase (see section IV.1.1) is indicated by a brown vertical line

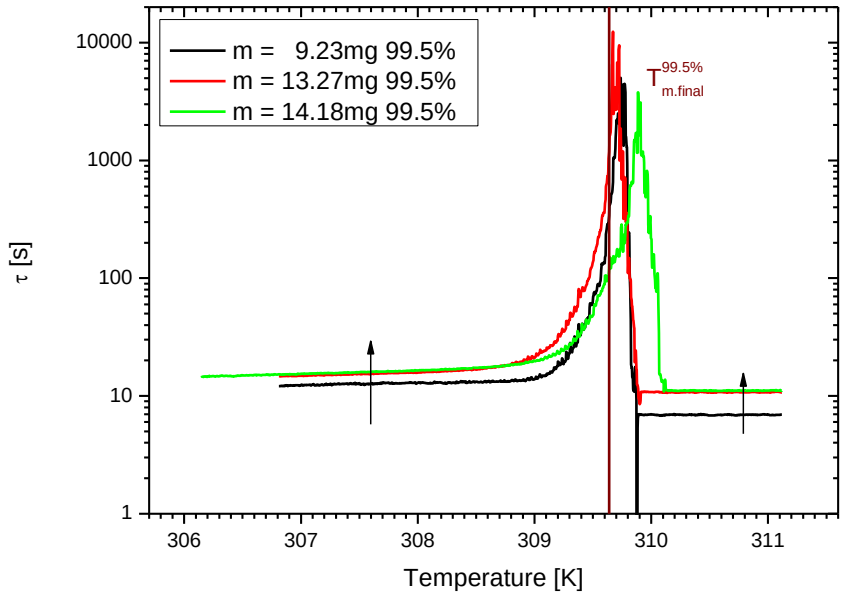

Figure 62: Temperature dependence of the relaxation times of C20 samples with a purity of 99.5+%. The relaxation times are obtained from data determined by TOPEM while melting the rotator phase. The final melting temperature of the rotator phase (see section IV.1.1) is indicated by a brown vertical line

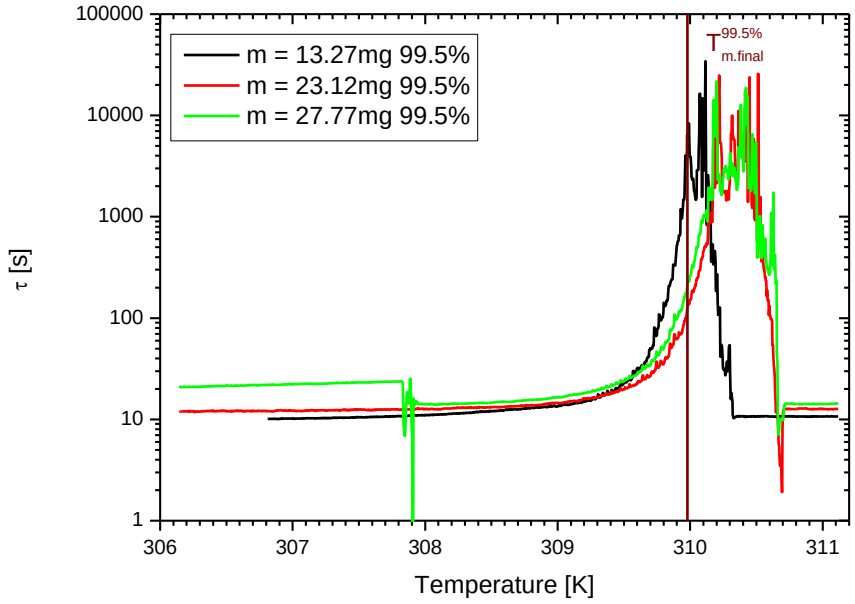

Figure 63: Temperature dependence of the relaxation times of C20 samples with a purity of 99.5+%. The relaxation times are obtained from data determined by TOPEM while melting the triclinic phase. The final melting temperature of the triclinic phase (see section IV.1.1) is indicated as a vertical line.

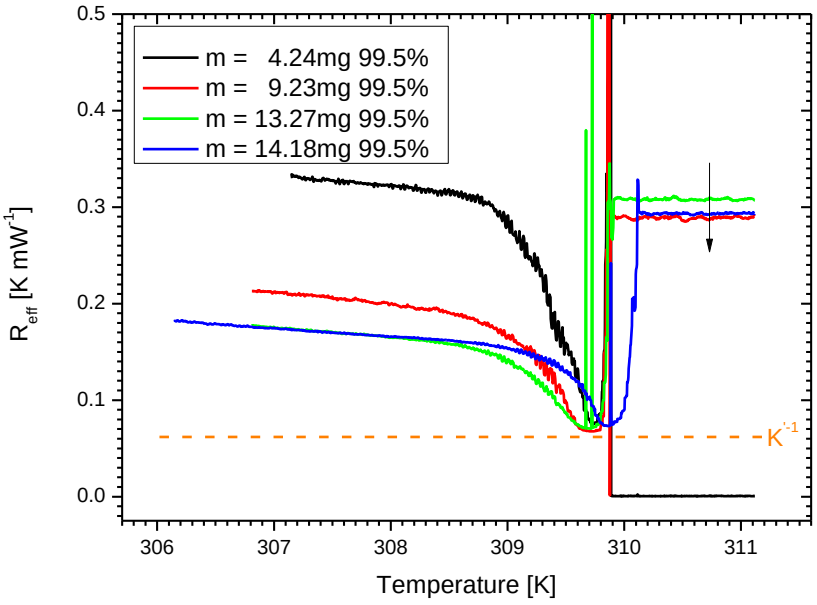

Figure 64: Effective thermal resistance for heating runs of C20 samples in the rotator phase with a purity of 99.5+%. Masses are indicated in the legend. The inverse DSC calibration factor *K'* is indicated as orange dashed line.

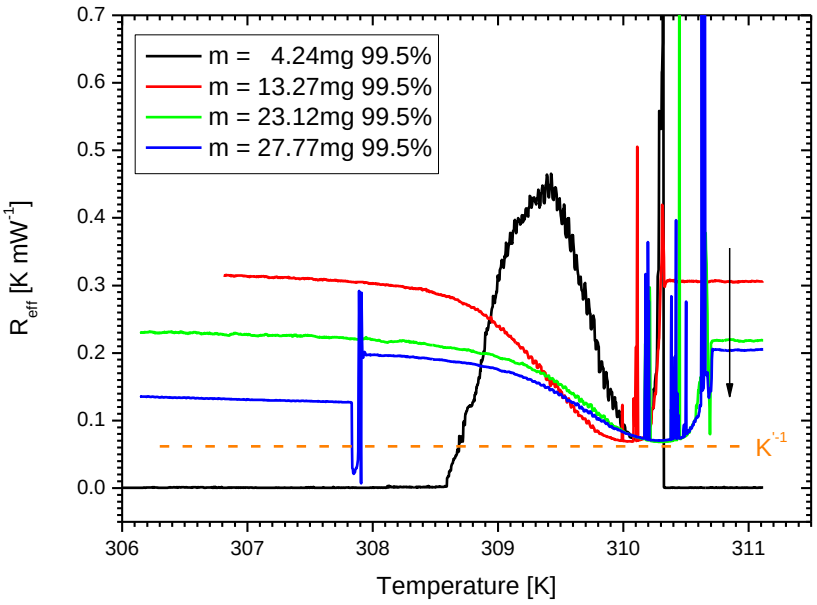

Figure 65: Effective thermal resistance for heating runs of C20 samples in the rotator phase with a purity of 99.5+%. Masses are indicated in the legend. The inverse DSC calibration factor *K'* is indicated as orange dashed line.

IV.4. Lattice structure in eicosane (XRD)

IV.4.1. Identification of the phases

In figure 66 a diffractogram of a liquid sample is shown. It depicts an amorphous peak at d = 4.545 Å (Literature: d_{Lit} = 4.5 Å [61]). The asymmetric behaviour between low and high scattering angles stems mostly from the shape of the sample holder. The exact shape also depends on the height alignment. The Topas software [62] is used to correct for this asymmetric behaviour. Nevertheless this underground could influence the fit of the amorphous peak. For sharper peaks this should not pose any problem because the asymmetry is on a larger angular range.

In figure 67 the diffractogram of a sample in the triclinic phase is depicted. Due to the low symmetry of the structure the number of observable peaks between 5° to 30° in the 2θ is high. With the TOPAS software the profile was fitted with a Rietveld structure refinement algorithm[63]. This algorithm considers the geometry of the setup and the shape of the different peaks to better define the lattice structure and parameters as height offset or crystallite size. The structural data were taken from the Crystallography Open Database (COD) [64,65]. These data were taken as starting point for the refinement algorithm. The fit is depicted in figure 67. It reproduces the peaks in the range between 18° and 30°. For lower angles the positions of the peaks seem to be accurate whereas the shape and the intensity of the peaks are different. These deviations are probably linked to the fact that the triclinic phase is crystallised from the melt. Nyburg and Gerson [65] grew their crystals of n-dodecane to

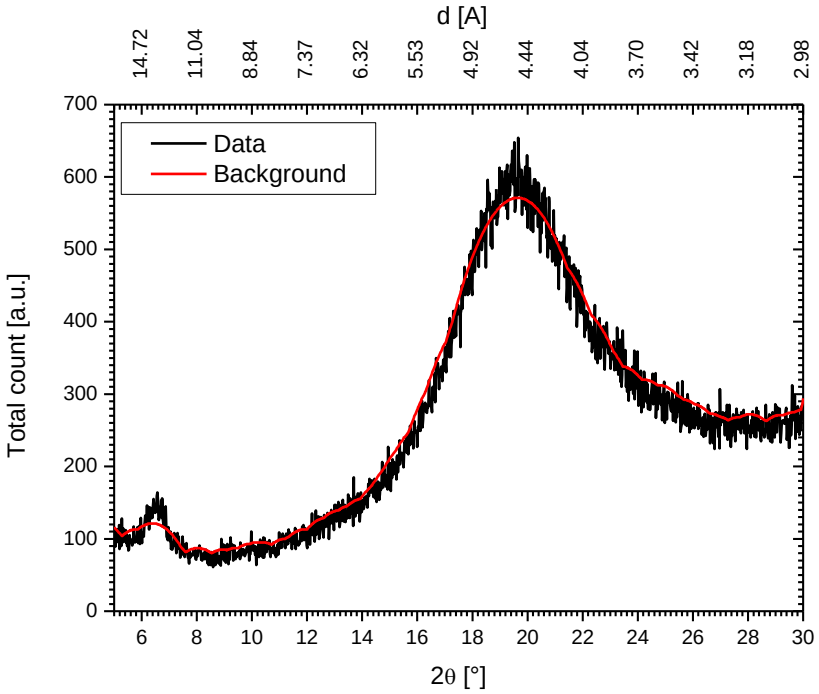

Figure 66: Diffractogram of the liquid phase of a C20 sample with purity 99.0+%. Black line data measured, red line background calculated with the Eva software by Bruker.

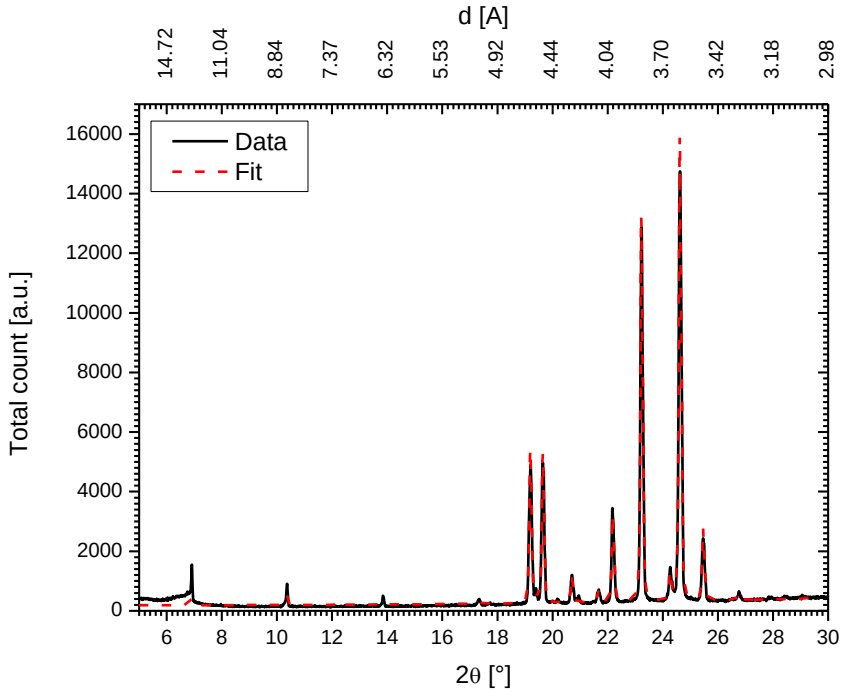

Figure 67: Diffractogram of the triclinic phase of a C20 sample with purity 99.5+%. Black line data measured, red line fitted with a Rietfeld refinement method with the Topas software [62].

obtain single crystals. In comparison our melt grown samples show crystallites of different shape and size already at a macroscopic level (see figure 68). This means that on one hand we cannot compare the relative intensities of the peaks, because the measurements do not fulfil the powder diffraction criterion. On the other hand defects can be introduced by the crystallisation process itself (e.g. screw dislocations) [66]. Albeit this error source the lattice parameters acquired from our data fitting are comparable to literature values (see table 3). The fitted lattice parameters correspond to a structure where the *c*-axis is along the backbone of the C20 molecules. The reduced parameters correspond to the shortest possible axis and smallest angle deviations from 90° to describe the unit cell[67]. The corresponding transformation is in our case:

$$\vec{a}' = -\vec{a} \quad \text{(IV.7)}$$

$$\vec{b}' = \vec{b} \quad \text{(IV.8)}$$

$$\vec{c}' = \vec{c} - 2\vec{a} \quad \text{(IV.9)}$$

where $\vec{a}$, $\vec{b}$, $\vec{c}$ are the fitted- and $\vec{a}'$, $\vec{b}'$, $\vec{c}'$ are the reduced lattice parameters.

Table 3: Lattice parameters for the triclinic phase of C20, fitted with Rietveld refinement, reduced by (IV.7) - (IV.9) and literature values.

Parameter	Fitted	Reduced	Lit. [65]	Lit. [8]	Lit. red.[68]
a	4.301 Å	4.301 Å	4.293 Å	4.296 Å	4.281 Å
b	4.838 Å	4.838 Å	4.841 Å	4.828 Å	4.820 Å
c	27.40 Å	25.51 Å	27.35 Å	27.5 Å	25.52 Å
α	85.68 °	91.17°	85.33 °	86.0 °	91.18 °
β	68.35 °	93.38°	68.21 °	68.6 °	93.52 °
γ	72.49 °	107.51°	72.61 °	72.8 °	107.35 °

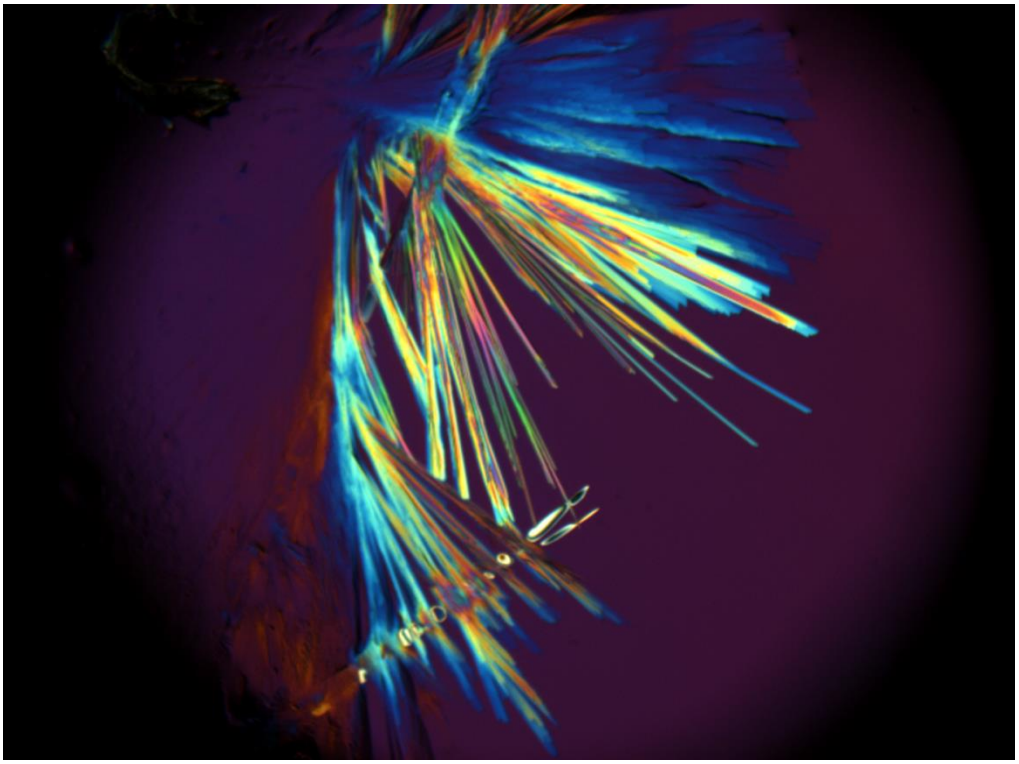

Figure 68: Polarisation optical micrograph (POM) of crystallising C20. Purple (1st order red, λ-plate) background is the amorphous liquid phase.

Another interesting parameter that we obtained from the Rietveld refinement is the height displacement of the sample $\Delta h = 109\ \mu\mathrm{m}$. Although an alignment of the sample holder height has been carried out (see subchapter III.3) the samples are not necessarily aligned. The angular correction for the height mismatch is [44]:

$$\theta_{\Delta h} = \theta + \frac{\Delta h}{R}\cos(\theta) \qquad \text{(IV.10)}$$

where $\theta_{\Delta h}$ is the actual scattering angle, θ is the measured angle and R is the goniometer radius. The angular deviation due to height mismatch is more dominant at lower angles which can be seen in the second term on the right hand side of (IV.10).

A diffractogram of a sample in the rotator phase is depicted in figure 69. The peaks correspond to face centred orthorhombic symmetry found in the RI phase [7,8]. The first three reflexes (0 0 l) for even *l* describe the *c*-axis along the backbone of the molecules. The (1 1 1) and (0 2 0) reflexes show the largest variation with temperature in the RI phase (see below). They will be referred to as peak 1 and peak 2 respectively form this point on. The RI phase of C20 shows no tilt of the molecules relative to the layer normal [7]. Peak 1 and peak 2 sit on top of an increased background. Ungar et al. [30] explained it as being caused by an increased Debye-Waller effect. The Debye-Waller effect describes the broadening of a peak due to thermal fluctuations of atoms or molecules around their equilibrium position[69]. Due to the inherent disorder in the rotator phases with gauche defects [19] and different configurations [7] the positional uncertainty is bigger than the one cause

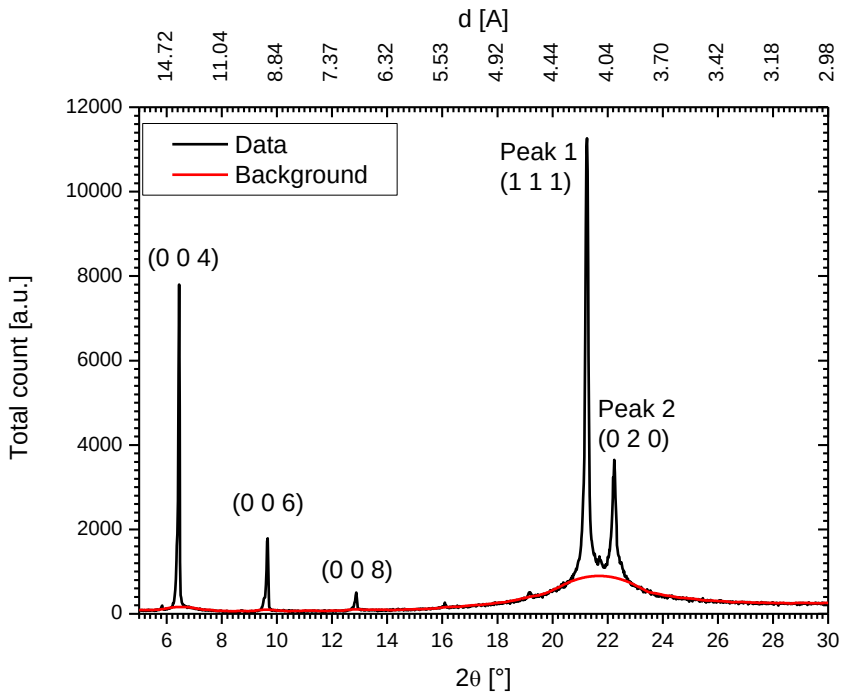

Figure 69: Diffractogram of the rotator phase of a C20 sample with purity 99.0+%. Black line data measured, red line background calculated with the Eva software by Bruker.

only by thermal vibrations around an equilibrium position. The interpretation of the increased background is ambiguous [70] and will further discussed in chapter V.

IV.4.2. Temperature dependence of structure the rotator phase

In order to be able to compare DSC and XRD measurements the temperature must be comparable. Therefore a similar experiment as for the determination of the final melting temperature in section IV.1.1 was employed. Starting in the liquid phase, a C20 sample with purity 99.0+% was cooled down to 308.95 K. Then the temperature was increased in steps of 0.2 K staying for 36 minutes at each temperature. The diffractograms were recorded for 2θ-values between 5° and 30° with an increment of 0.0198° per data point. A complete scan lasted about 70 seconds, thus 30 scans were done during each isothermal segment between the steps.

Figure 70 shows a zoom into the diffractograms resulting from these measurements in the region where peak 1 and peak 2 can be found. As expected, the peaks appear after the initial temperature jump from the liquid phase (313.15 K) to the rotator phase (308.95 K) (blue line). Judging from the height of the peak the crystallisation process is not completed at 308.95 K but rather at 309.05 K. Subsequent step-wise increase of temperature causes the first peak to move to slightly larger 2θ angles while the peak area decreases. Peak 2 shifts more prominently to smaller 2θ angles while its peak area decreases [7]. At 310.15 K both peaks disappear.

In figure 71 the background resulting from the fit of the data shown in figure 69 is depicted. The amorphous peak of the liquid phase (around 19.5°) and the halo below peak 1 and peak 2 (around22°) are clearly distinguishable. Moreover there seems to be no coexistence of the amorphous peak and the halo up to at least 309.75 K. Still the halo remains stable on a long time scale at 309.75 K.

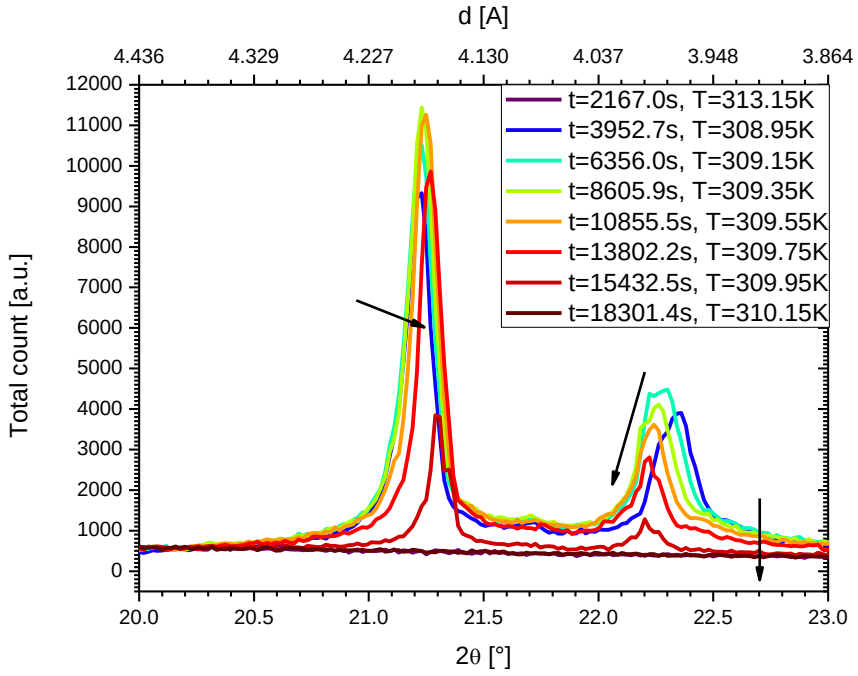

Figure 70: Peak 1 and peak 2 at different times and temperatures for a C20 sample with 99.0+% purity. The arrows indicate the trend in the rotator phase with increasing temperatures.

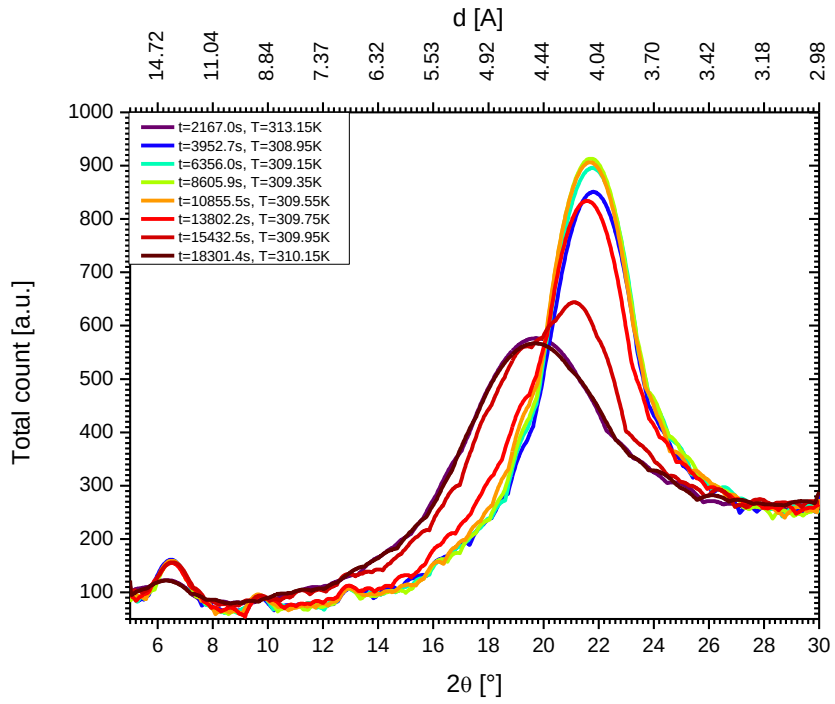

Figure 71: Background of the diffractograms at different times and temperatures created with the Eva software (see figure 66 and figure 69). Curvature and threshold criteria were chosen to obtain the background and reproduce the amorphous liquid peak completely.

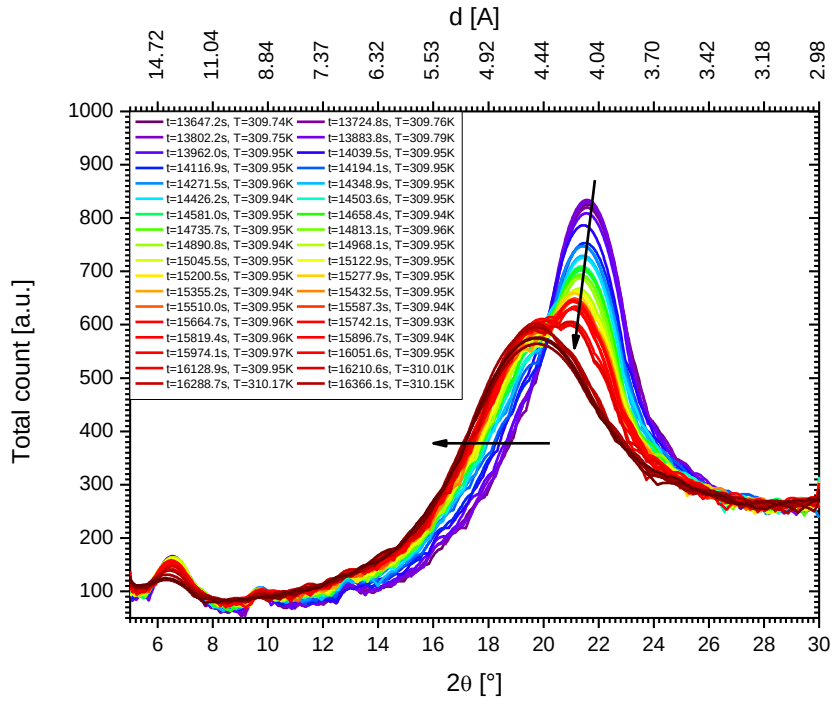

Figure 72: Background of the diffractograms at different times and temperatures between 309.75 K and 310.15 K The background was attained like in the previous figure. Arrows indicate change with time.

Figure 72 shows the background for each measurement between 309.75 K and 310.15 K. While the first three measurements at 309.75 K still coincide, the measurements at 309.95 K show a gradual decrease of the halo and increase of the amorphous peak with time. This means that at 309.95 K there is coexistence of the liquid and the rotator phases.

This melting temperature should be comparable to the final melting temperature derived in section IV.1.1. From here on a shift of $\Delta T = -0.4\,\mathrm{K}$ is used to correct temperatures from XRD measurements to adapt them to temperatures from DSC measurements.

Measurements with constant cooling rate

Similar to the TOPEM measurements, XRD measurements were performed with a slow cooling rate $\beta_u = 0.02$ K/min. In figure 73 the result of such a cooling run is shown in a 2d intensity plot. As mentioned in the previous section, one can see that the amorphous peak around 19° disappears immediately at one very sharply defined temperature. This is then identified as the transition to the rotator phase. In the rotator phase the variation of the position of peak 2 with temperature is clearly visible, the one of peak 1 is less pronounced. At the transition to the triclinic phase the halo around peak 1 and 2 vanishes together with both peaks. Therefore this part of the background is clearly relatable to the RI phase. In the triclinic phase none of the peaks shows any shift with temperature on a measurable scale within the observed temperature range.

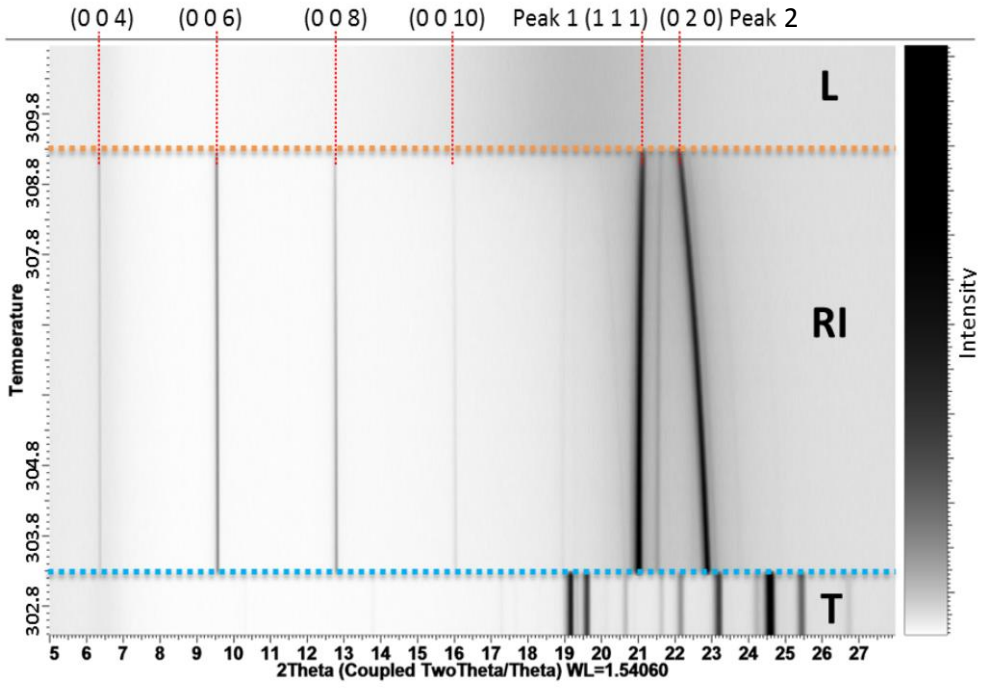

Figure 73: 2D difractorgram as a function of temperature for a C20 sample with purity 99.0+%. (created with Eva software by Bruker). The orange dashed line indicates the transition to the rotator (RI) phase. The blue dashed line indicates the transition to the triclinic phase.

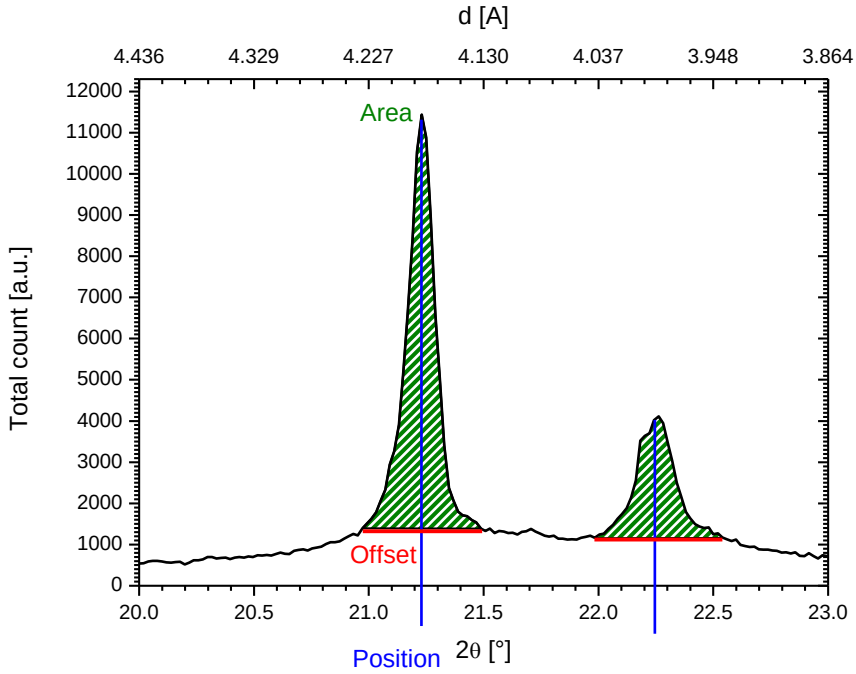

Figure 74: Quantities of interest for the characterisation of the peaks from the diffractograms.

We used three parameters to characterize the peaks: position, area and offset (see figure 74). These parameters are determined from Gaussian fits of the peaks. The position of the (0 0 l) peaks are used to correct for the height mismatch (see equation (IV.10)). With peak 1 and peak 2 the other lattice parameters of the sub structure can be calculated:

$$\bar{c} = \frac{1}{L - l_0 + 1} \sum_{l=l_0}^{L} \frac{2 \cdot l \cdot \lambda}{2 \cdot \sin\left(\theta_{(0\,0\,2l)}\right)} \tag{IV.11}$$

$$b = \frac{2 \cdot \lambda}{2 \cdot \sin\left(\theta_{(0\,2\,0)}\right)} \tag{IV.12}$$

$$d_{(1\,1\,1)} = \frac{\lambda}{2 \cdot \sin\left(\theta_{(1\,1\,1)}\right)} \tag{IV.13}$$

$$a = \sqrt{\frac{1}{\frac{1}{d_{(1\,1\,1)}^2} - \frac{1}{b^2} - \frac{1}{\bar{c}^2}}} \tag{IV.14}$$

where $\theta_{(h\,k\,l)}$ is the reflex corresponding to (h k l), λ the average wavelength of the x-ray difractometer ($\lambda = 1.5406\,\text{Å}$) and *a*, *b*, $\bar{c}$ are the lattice parameters of the face centred orthorhombic structure. $\bar{c}$ correspond to an average value of the *c*-axis and was calculated from the (0 0 6), (0 0 8) and (0 0 10) peaks. In figure 75 the height deviation for different scans is depicted. The height deviation scatters mostly around a certain constant value. To calculate the lattice parameters an average value was taken.

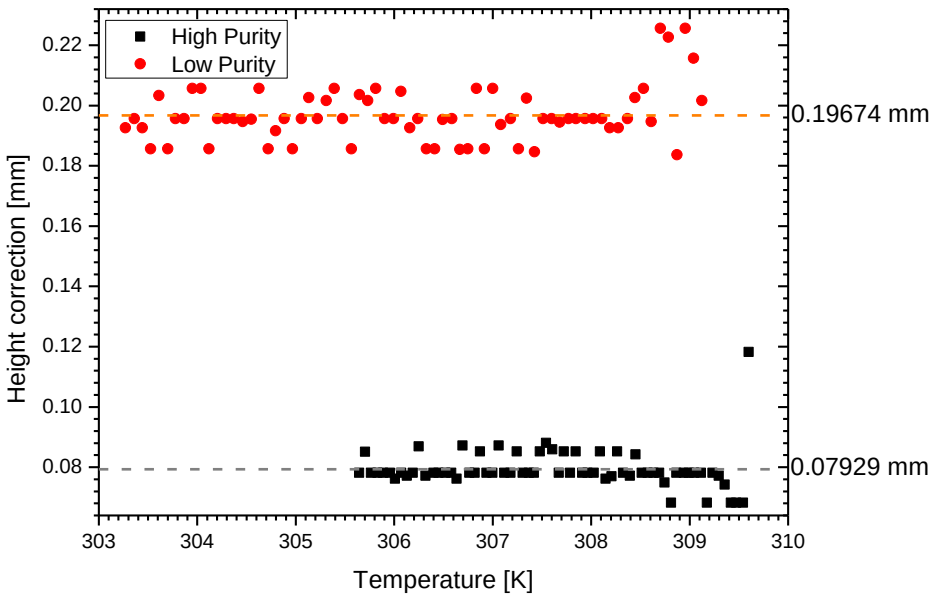

Figure 75: Height deviation calculated from diffractogram (see text) for a high purity black squares (99.5+%) and low purity red circles (99.0+%) C20 samples. The dashed lines indicate the average used to calculate the actual position of the reflexes.

In figure 76 the lattice parameters and the hexagonal distortion parameter D [7,16] are depicted for the two (for each purity one) slow cooling measurements for which the triclinic phase appeared at the lowest temperature.

$$D = 1 - \frac{b}{\sqrt{3}a} \qquad \text{(IV.15)}$$

The distortion parameter is an order parameter which indicates how close the actual structure is to hexagonal symmetry (D=0). Sirota et al.[7] showed that D is equal to 0.133 when the structure is at the orthorhombic limit. Independent of the purity both samples depict the same lattice parameters. The liquid to rotator phase transitions seem to correspond to the final melting temperatures found in section IV.1.1. This supports the choice of the temperature shift factor adopted in the previous part.

The data of the lattice parameters in figure 76 are used to fit a parabolic equation to it:

$$x = x_0 + A\left(T - T_{Ref}\right) + B\left(T - T_{Ref}\right)^2 \qquad \text{(IV.16)}$$

where x represents the lattice parameters a, b or c. x_0, A and B are polynomial fit parameters and T_{Ref} is an arbitrary reference temperature. T_{Ref} is chosen in a way that the polynomial fit parameters x_0 and A do not change if B=0. As the model is empirical T_{Ref} has no specific meaning. The fits and their residuum are depicted in figure 77. The fitted parameters are shown in table 4 and table 5 for the high and

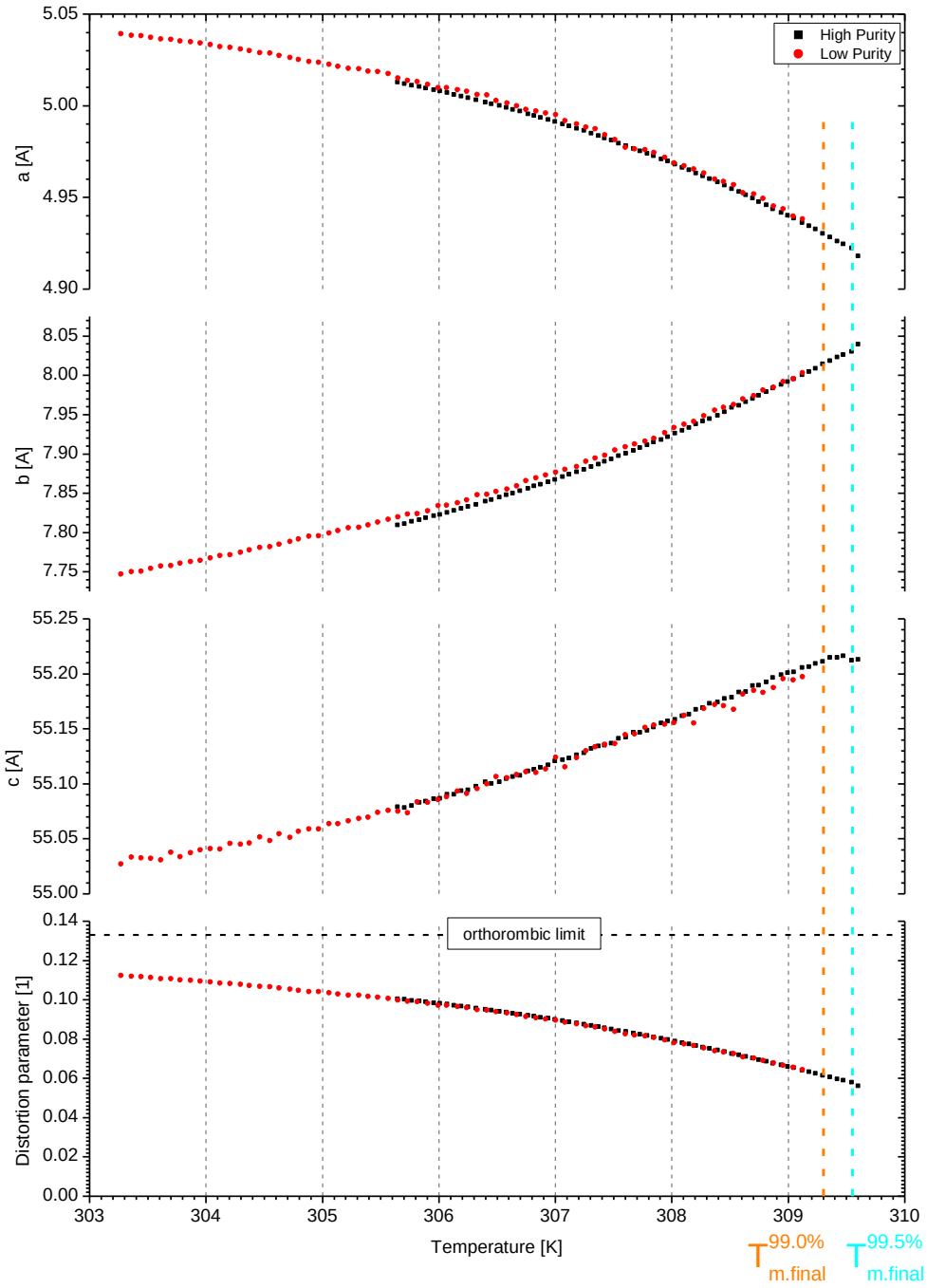

Figure 76: Lattice parameters a, b, c and distortion parameter *D* as a function of temperature for a high purity (black squares 99.5+%) and low purity (red circles 99.0+%) sample. The corresponding final melting temperatures are indicated by dashed lines (99.5+% teal, 99.0+% orange).

Table 4: Fit parameters for sub-lattice of C20 sample with 99.5+% purity.

T_{Ref} = 306.19 K	a	b	c
x_0 in Å	5.0077 ± 0.0004	7.8406 ± 0.0006	55.093 ± 0.001
A in Å K^{-1}	-0.0168 ± 0.0001	0.0428 ± 0.0002	0.0296 ± 0.0004
B in Å K^{-2}	-0.0023 ± 0.0001	0.0041 ± 0.0001	0.0025 ± 0.0003

Table 5: Fit parameters for sub-lattice of C20 sample with 99.0+% purity.

T_{Ref} = 307.62 K	a	b	c
x_0 in Å	4.9780 ± 0.0004	7.9016 ± 0.0002	55.144 ± 0.001
A in Å K^{-1}	-0.0234 ± 0.0001	0.0578 ± 0.0001	0.0374 ± 0.0005
B in Å K^{-2}	-0.0030 ± 0.0001	0.0056 ± 0.0001	0.0014 ± 0.0005

low purity samples respectively. The accuracy of the parameters is given by 95% confidence interval of the fit.

It is interesting to note that the *b* and *c* axis are increasing with temperature whereas the *a* axis is decreasing. Ungar et al. relate this to enhanced longitudinal oscillations accompanied by a reduction of lateral oscillations with increasing temperature[14,30]. The layer spacing d = c/2 = 27.54 Å and its change with temperature $\Delta d / \Delta T =$ 0.0146 ± 0.0025 Å/K are in good agreement with values from literature[7] (27.65 Å and 0.02 Å/K at 305.6 K). Both axes *a* and *b* are in the range of 5.03 to 4.91 Å and 7.77 to 8.13 Å respectively, expected for the RI phase in this temperature range [8,9].

Figure 78 shows the fit of the hexagonal distortion parameter with an empirical model introduced by Sirota et al. [7]:

$$D(T) = D_1(1 - T_0/T) + D_2(1 - T_0/T)^2 \qquad \text{(IV.17)}$$

where D_1 and D_2 are polynomial fit parameters and T_0 describes the temperature at which the structure becomes hexagonal. The derived fit parameters are in table 6

This temperature is in the liquid phase for C20 as it does not reach the hexagonal structure before melting. The critical temperature $312.5\ \mathrm{K} \leq T_0 \leq 313.1\ \mathrm{K}$ suggested by this model corresponds to the surface crystallisation temperature[50] $T_{m,ML} \approx T_m + 3K$. As this model is empirical the extrapolation can be a coincidence.

Table 6: Fit parameters for the hexagonal distortion parameters for C20 samples with different purity.

Parameter\Sample	99.0+%	99.5+%
D_1	-6.1525	-7.1204
D_2	-83.498	-118.14
T_0	313.06	312.53

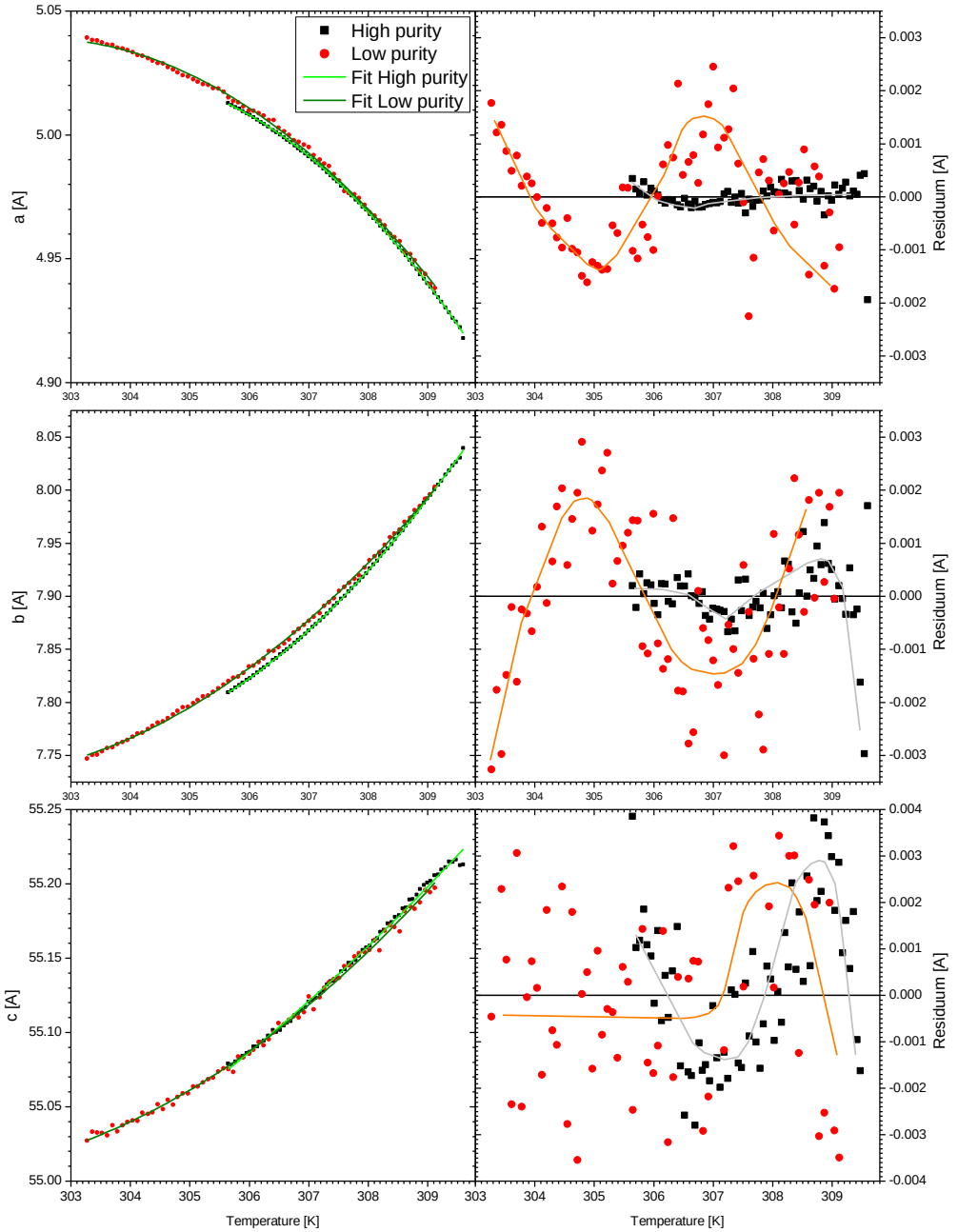

Figure 77: Left hand side lattice parameters *a*, *b*, *c* as a function of temperature for a high purity (black squares 99.5+%) and low purity (red circles 99.0+%) sample. Residuums are shown in the graphs on the right hand side.

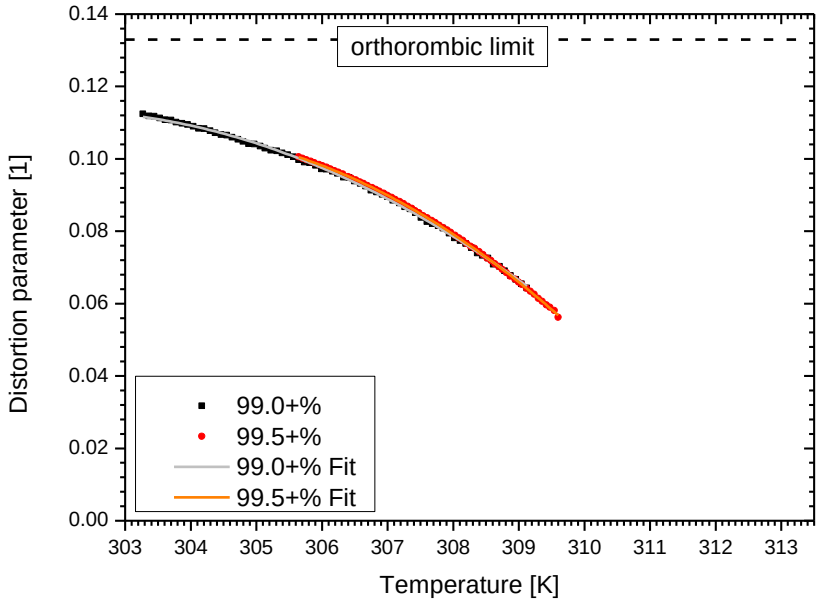

Figure 78: Distortion parameter, fits (solid lines) and extrapolation (dashed lines) as function of temperature for C20 samples with different purities.

In figure 79 the lateral area per chain (perpendicular to the molecule backbone) and the volume per monomer (CH_2) are depicted. The area is comparable to the ones measured by Sirota et al. [7] for other n-alkanes in the rotator phase. The volume per monomer is slightly above the values of hexagonal structure (26 to 26.5 $Å^3$[6]) but it is still below the liquid monomer volume of 29.6 $Å^3$. It cannot be excluded that the deviation of the derived parameters between the measurements of different purities arises from the inaccuracy of the measurements. Measurements on samples with the same purity showed similar deviations.

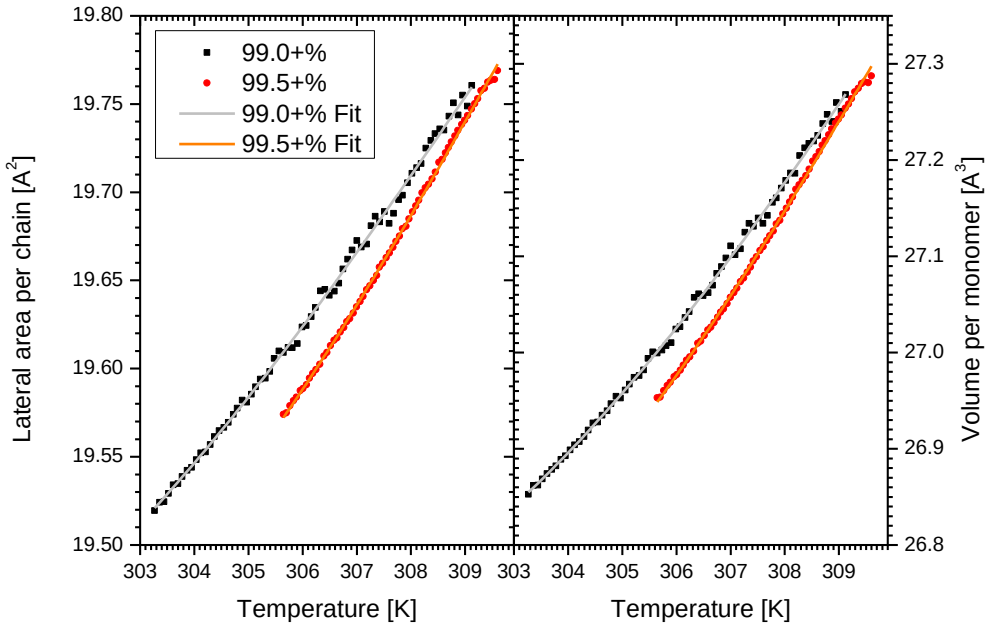

Figure 79: Lateral area (left) and volume per monomer (right) over temperature for C20 samples with different purities.

Measurements with temperature modulation

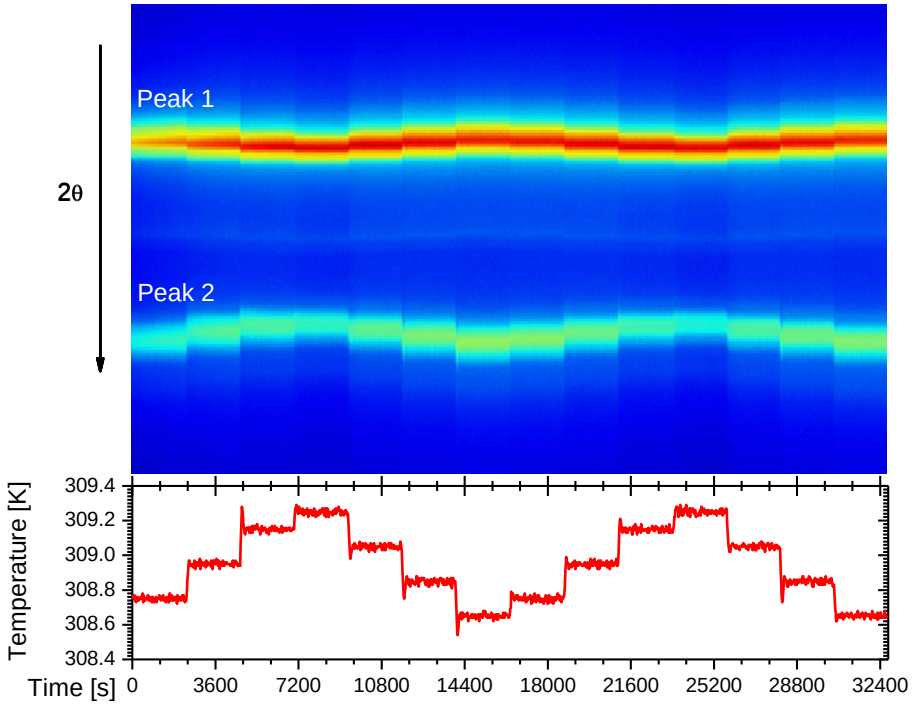

Figure 80: Top difractogram in 2d intensity graph for a step experiment with moving detector and x-ray cathode. Colours indicate x-ray intensity (blue (low) to red(high)). Bottom corresponding temperature over time. As the horizontal direction of the intensity graph depicts single measurements the timesscales do not necessarily coincide precisely.

Step experiment with moving x-ray tube and detector were done An increment of 0.015° a 2θ range of 20.5° to 23° and an illumination time of 100 ms allowed us to do a scan every 25 seconds.

In figure 80 the diffractogram of such an experiment is shown. The measurement started after cooling from the melt at 313.15 K to 308.75 K. Then the temperature program shown in the lower part of Figure 80 was used. Figure 81 shows the evolution of the different parameters defining the two peaks over time. It is interesting to note that although in the area as in the offset a monotonic increase (without steps) can be observed during the first two steps, the positions of the peaks already adept fast to the temperature steps. The variation of the peak's position during the first two isotherms is small in comparison to the response to the temperature steps. If the position of the peaks is taken as an indicator of the temperature of the system, this would then suggest that the new temperature is reached relatively fast after each temperature step.

In the experiment each temperature is reached twice, which then allows to compare the values of each parameter for these temperatures. For the position of peak 1 the values are the same with the exception of the first two isotherms. For the position of peak 2, the first 3 isotherms are show different values whereas for the following isotherms, the same values for the first and second run are found.

The increase observable in the area of peak 1 during the first 3 isotherms is a hint for ongoing crystallisation due to the initial jump to the lowest temperature. A similar behaviour is observed for the area of peak 2. The first two isotherms show an increase in area and afterwards the area seems to adapt to specific values for the different temperatures.

The offsets for both peaks display similar behaviour. They show a monotonic increase during the first 2 isotherms then further increase after a step-like decrease (between isotherms) during the 3rd isotherm. It is interesting to note that the offset increases where the area also grows. This could mean that when the crystalline part (area of the peaks) grows, the broad background which could be related to defects, does also grow. It should be stressed that the background can be clearly separated from the amorphous halo.

The step experiments have been used to derive the lattice parameters (see figure 82). Due to the lack of the (0 0 l) peaks no height correction could be employed. Additionally the distance $d_{(1\,1\,1)}$ was approximated as $d_{(1\,1\,0)}$ which yields the following approximation for the *a* axis:

$$d_{(1\,1\,0)} \approx d_{(1\,1\,1)} \tag{IV.18}$$

$$a' = \sqrt{\frac{1}{\frac{1}{d^2_{(1\,1\,0)}} - \frac{1}{b^2}}} \tag{IV.19}$$

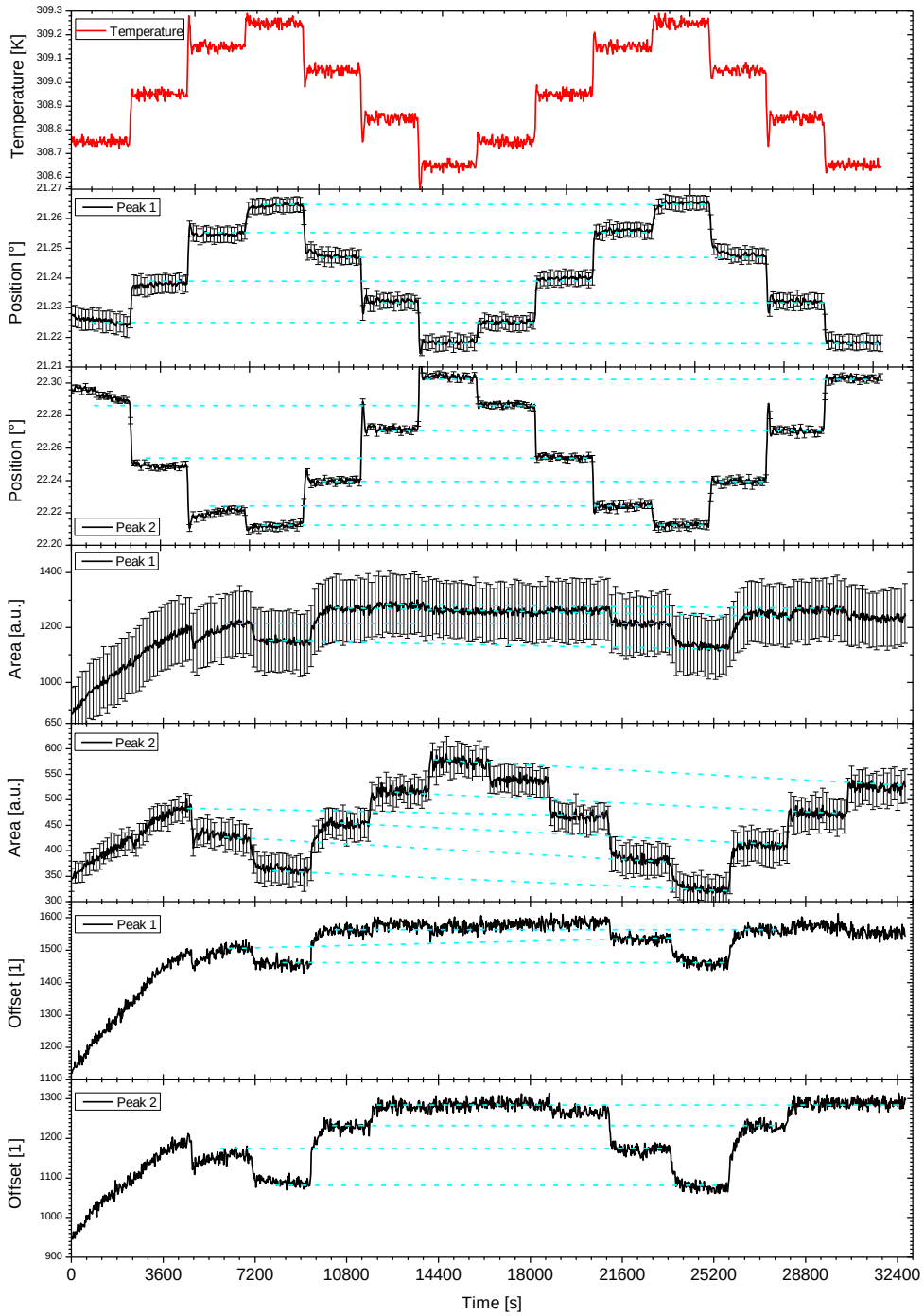

Figure 81: Temperature, position, area and offset for peak 1 and 2 over time for the experiment depicted in figure 80.

The resulting lattice parameters were fitted with equation (IV.16) with the quadratic part set to $B = 0$ Å K^{-2} as the temperature range is too small to see a quadratic contribution. The reference temperature is set to $T_{Ref} = 307$ K to better compare the lattice parameters to the ones in table 4 and table 5. The resulting fit parameters are shown in table 7.

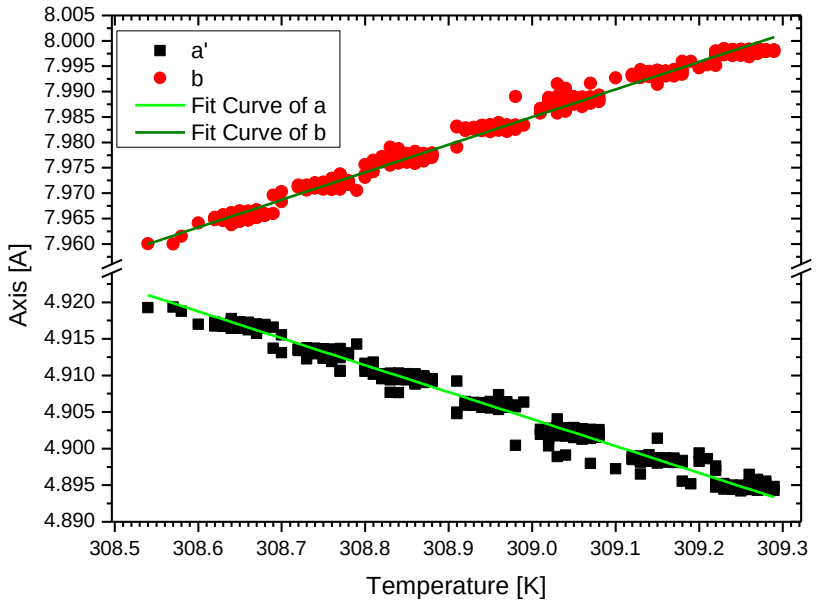

Figure 82: Lattice parameter a' and b over temperature for a step experiment.

Table 7: Fit parameters for sub-lattice of C20 sample with 99.0+% purity from a step experiment.

$T_{Ref} = 307$ K	a'	b
x_0 in Å	4.9777 ± 0.0002	7.8763 ± 0.0003
A in Å K^{-1}	-0.0368 ± 0.0001	0.0543 ± 0.0001

The parameter for the b-axis is in good agreement with values in the previous part. The slope for the a-axis is considerably larger than the one previously derived. Nevertheless the calculated data are comparable to the previous ones since the deviation is in the range of 1%.

IV.4.3. Relaxations of the lattice structure

Relaxations after single temperature steps

Since the actual temperature steps that can be realized by the X-Ray machine do not correspond to ideal step functions, the following expression is used to describe the temporal evolution of the sample temperature during a step:

$$T(t) = T_0 + \theta(t - t_0) \cdot \Delta T \cdot \left(1 - \exp\left(\frac{t_0 - t}{\tau_T}\right)\right) \tag{IV.20}$$

where T_0 is the initial temperature, $\theta(t - t_0)$ the heavyside function, ΔT the temperature step and τ_T the settling time of the temperature. To describe the response of the structural parameters we use a generalised linear response function:

$$\chi(t - t') = \frac{\chi_0}{\tau} \exp\left(\frac{t - t'}{\tau}\right) \tag{IV.21}$$

where χ_0 is a generalized susceptibility and τ the relaxation time. The response function is normalized such that:

$$\int_{-\infty}^{t} \chi(t - t')dt' = \chi_0 \tag{IV.22}$$

The response $g(t)$ is then given by:

$$g(t) = \int_{-\infty}^{t} \chi(t - t') \cdot T(t')dt' + g_0 \tag{IV.23}$$

$$<=> \quad g(t) = \chi_0 T_0 + \theta(t - t_0) \cdot \chi_0 \cdot \Delta T \cdot \left(1 + \frac{\tau}{\tau_T - \tau} \exp\left(-\frac{t - t_0}{\tau}\right) - \frac{\tau_T}{\tau_T - \tau} \exp\left(-\frac{t - t_0}{\tau_T}\right)\right) + g_0 \tag{IV.24}$$

where g_0 is an offset value. This response function can be used for the different fit parameters of the peaks (position, area, offset) as well as for the lattice parameters *a* and *b*.

To apply equation (IV.20), the temperature profiles should not have overshoots, nor deviations before the temperature steps (indicated by blue circles in figure 83 and figure 84). Experiments with several steps between two isotherms were done to control that the measured parameters relax to an equilibrium state and are not in a state of transition. First the temperature profile is fitted with equation (IV.20) (see figure 85). Using the temperature fit results, the peak parameters are fitted according to equation (IV.24) (see figure 86 and figure 87). Figure 85 depicts an example of the fit of the temperature step and its corresponding

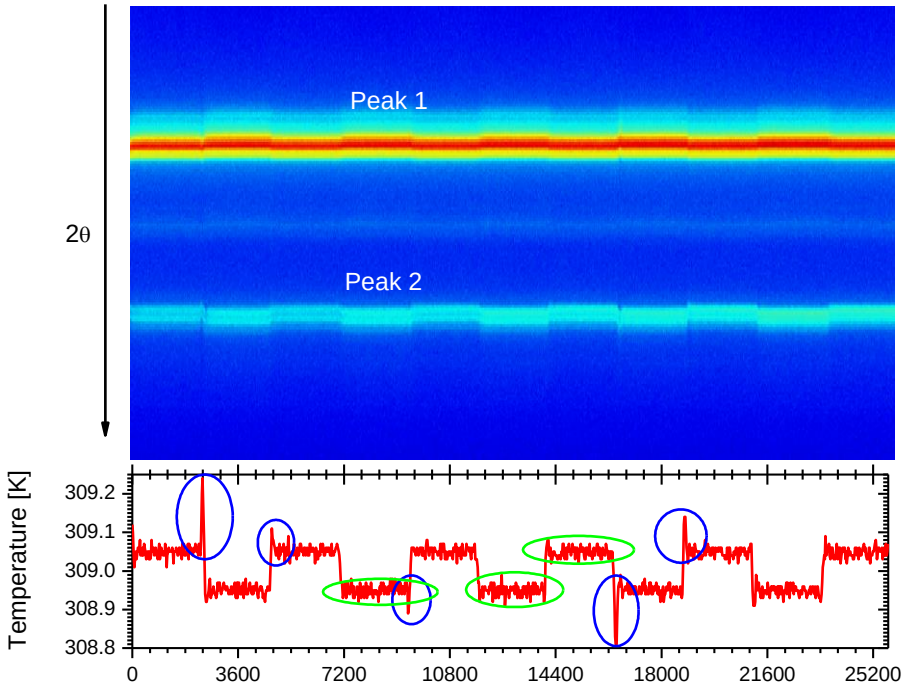

Figure 83: Top difractogram in 2d intensity graph for a step experiment with moving detector and x-ray cathode. Colours indicate x-ray intensity (blue (low) to red(high)). Bottom corresponding temperature over time. As the horizontal direction of the intensity graph depicts single measurements the timesscales do not necessarily coincide precisely. Blue circles indicate over- or undershoots in temperature. Green cirlces indicate isotherms with a monotonic approach to the temperature.

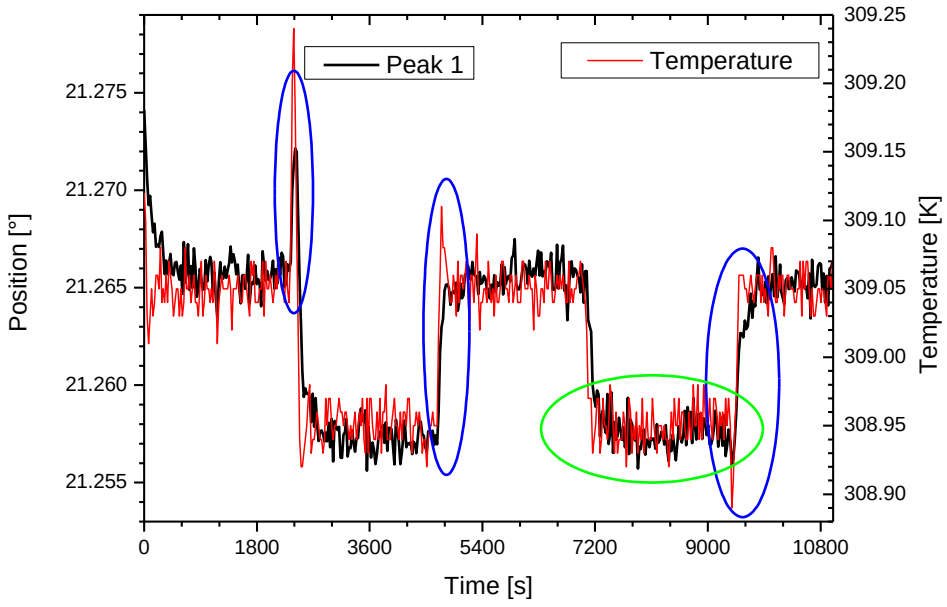

Figure 84: Temperature and position of peak of for the experiment depicted in figure 83. Blue circles indicate over- or undershoots in temperature. Green cirlces indicate isotherms with a monotonic approach to the temperature.

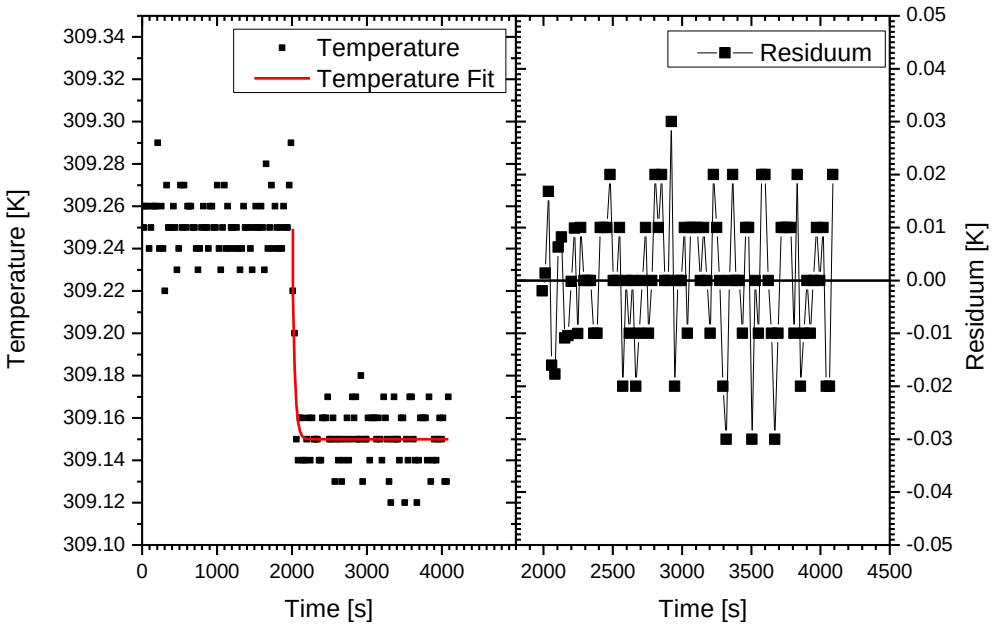

Figure 85: Temperature step of an XRD measurement, left hand side data and fitted step, right hand side residuum of the fit.

residuum. The residuum of the temperature fits is mostly between ±0.02 K. An example for a fit of the peak parameters is displayed in figure 86 and figure 87.

The lattice parameters *a* and *b* are then calculated from the fitted peak parameters using equations (IV.12) and (IV.19) , see figure 88. Table 8 lists the relaxation times for the different quantities. Form this specific example some more general result are discussed. The accuracy given by the confidence interval corresponds to the noise in the data. Secondly the relaxation observable in the position of the first peak is larger than the one of the second. The times found for the position of the second peak are close to the settling time of the temperature regulation and have an uncertainty close to 100%. For the lattice parameters the a-axis has a characteristic time below the one of the position of the first peak. The b-axis has values close to the one of the position of peak 2.

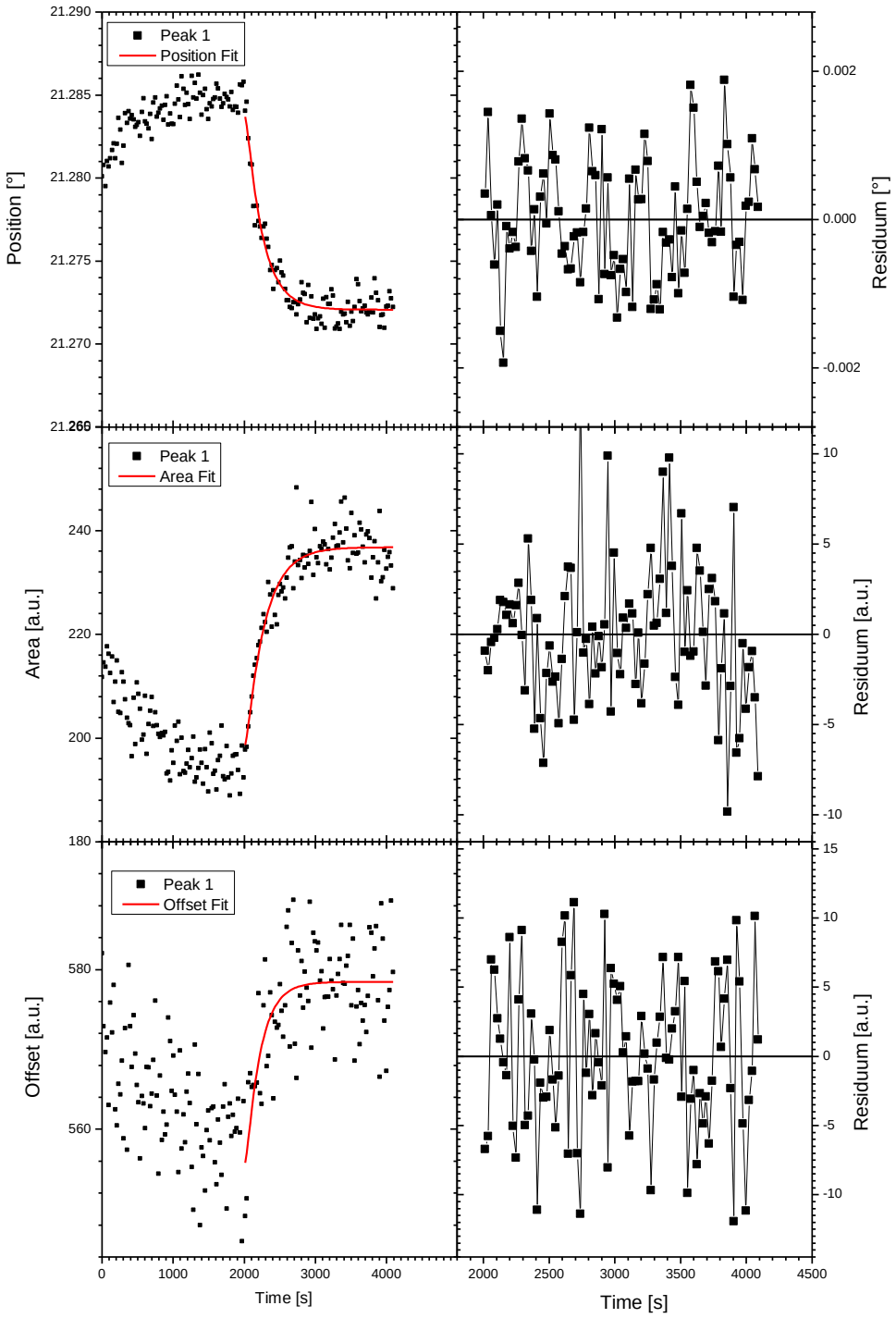

Figure 86: Fit of the position, area and offset of peak 1, left hand side data and fitted step, right hand side residuum of the fit.

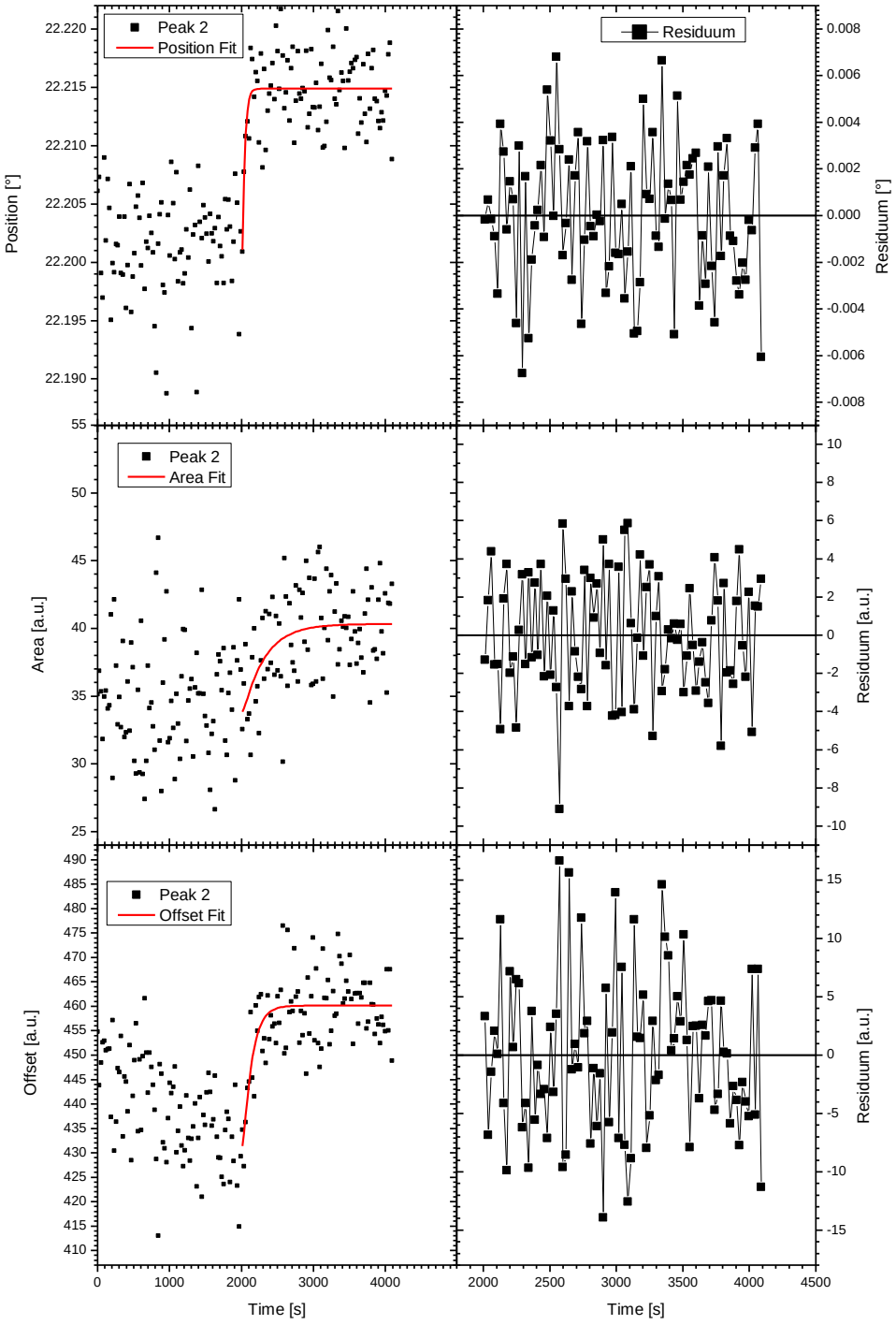

Figure 87: Fit of the position, area and offset of peak21, left hand side data and fitted step, right hand side residuum of the fit.

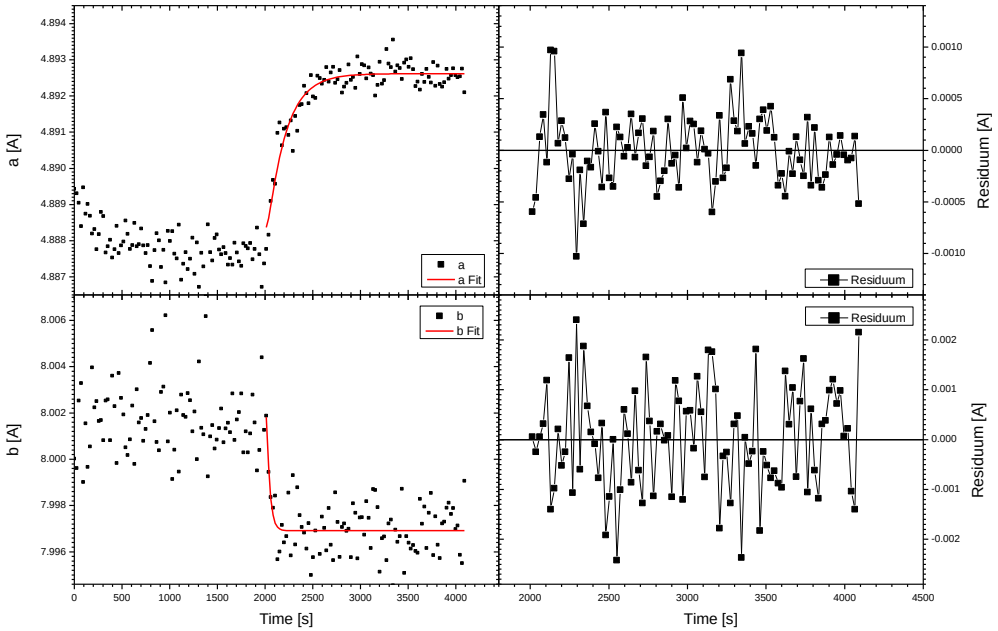

Figure 88: Fit of lattice parameters, left hand side data and fitted step, right hand side residuum of the fit.

Table 8: Relaxation times from the fits from figure 85 to figure 88.

Parameter		Relaxation time τ in s
Temperature		32.1 ± 6.1
Peak 1	Position	229.6 ± 31.0
	Area	263.2 ± 52.2
	Offset	199.2 ± 100.0
Peak 2	Position	11.8 ± 30.8
	Area	298.7 ± 266.04
	Offset	114.6 ± 65.7
a-axis		189.9 ± 31.4
b-axis		11.8 ± 30.8

Average relaxation times in the lattice structure

From approximately 300 measured steps 62 were kept for calculating the average. The kept measurements did not have a considerable drift in the parameters describing the peaks nor a considerable overshoot in temperature. To consider the different accuracy depending on the measurements the following weights are introduced:

$$w_i = \frac{\tau_i}{\delta\tau_i} \qquad \text{(IV.25)}$$

where τ_i is the relaxation of any parameter time of the i-th measurement and $\delta\tau_i$ the corresponding inaccuracy. The weighted arithmetic average is then in this case:

$$\langle\tau\rangle\left(T = T_{Ref}\right) = \frac{\sum_{i=1}^{n} w_i\left(T = T_{Ref}\right) \cdot \tau_i\left(T = T_{Ref}\right)}{\sum_{i=1}^{n} w_i\left(T = T_{Ref}\right)} \quad \text{(IV.26)}$$

where the reference temperature is the middle temperature between steps. The corresponding error are calculated from the uncertainty of fits.

In figure 89 the average relaxation times for the position of peak 1 and peak 2 are depicted. Next to the data points the number of temperature steps for the average is indicated. The dashed blue line indicates the average settling time of the temperature. The average scan time is depicted as orange dashed line. The relaxation times at 309.05 K and 309.25 K are from measurements with steps size of $\Delta T = 0.2$ K. These step had a high tendency to show temperature overshoot and therefore only two measurements have been taken under consideration. All the other data points are from measurements with a step size of $\Delta T = 0.1$ K. The average relaxation times for the position of peak 1 show a clear increase with temperature. The ones for peak 2 show rather constant values.

The dashed lines can be used as indicators for the classification of the relaxation time. Values of relaxation times close to or below this line or the settling time of the temperature are not reliable.

In figure 90 the average relaxation times for the area of the peaks is depicted. Both show an increase with rising temperatures. The relaxation times are comparable to the one for the position of peak 1. The relative error is in the same range for the area below peak 1 and much larger for the one of peak 2. The inaccuracies of the fits increase even more in the relaxations of the offset depicted in figure 91. The errors increase considerably for lower temperatures. This is linked to the smaller variation in the values of the offset (see last part in section Temperature dependence of structure the rotator phaseIV.4.2) which makes the fit difficult due to the noise (see fit of area in figure 87 as example).

The relaxation of the lattice parameters is depicted in figure 92. Above 308.8 K, the relaxations in the values for the a-axis are lower than the ones found for the position of peak 1. Their errors of the fits are comparable to those of the position. Considering the scattered data in the determination of the peaks position, the derived a-axis from both positions is less reliable than the position of peak 1. The relaxation times for the b-axis and the position of peak 2 coincide. This was expected as their dependence on each other is direct.

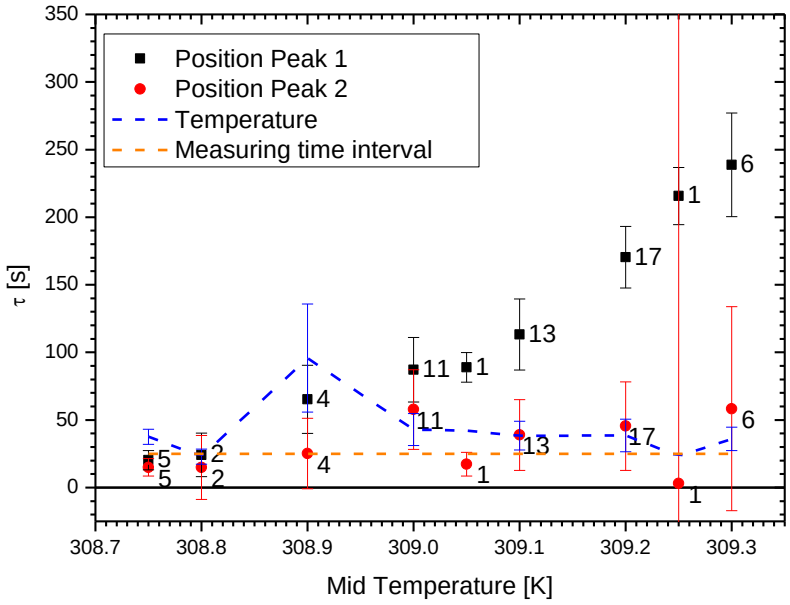

Figure 89: Average relaxation times for the position of the peaks over temperature. Numbers next to data points indicate the number of measurement over which was averaged. The blue dashed line indicates the average for the settling time of the temperature. The orange dashed line indicates the average time interval between scans.

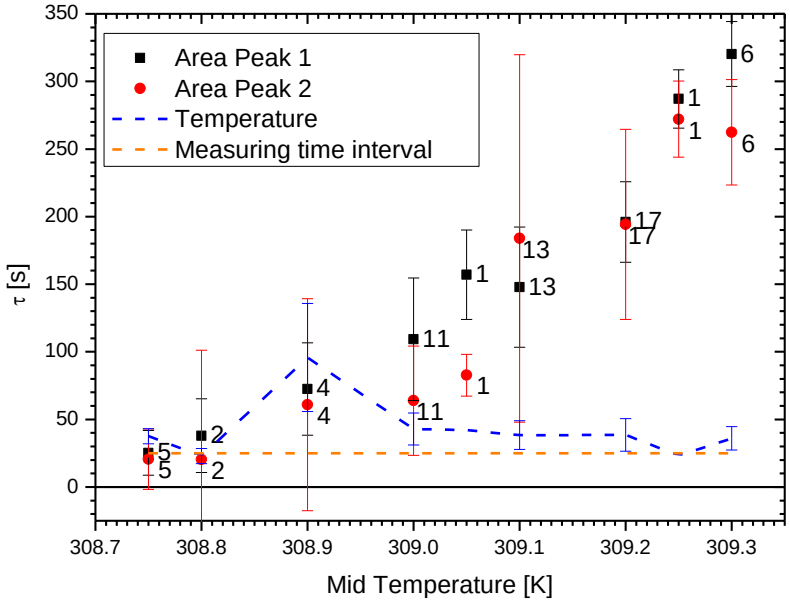

Figure 90: Average relaxation times for the area of the peaks over temperature. Numbers next to data points indicate the number of measurement over which was averaged. The blue dashed line indicates the average for the settling time of the temperature. The orange dashed line indicates the average time interval between scans.

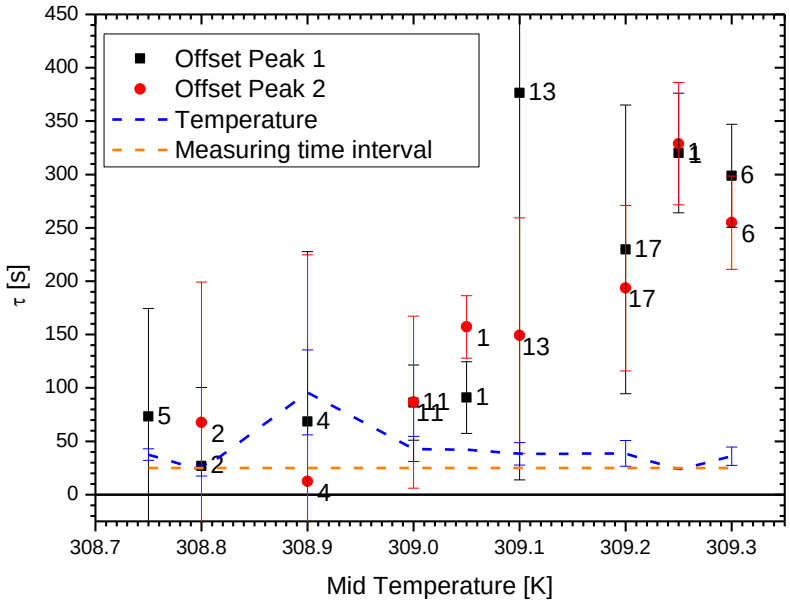

Figure 91: Average relaxation times for the offset of the peaks over temperature. Numbers next to data points indicate the number of measurement over which was averaged. The blue dashed line indicates the average for the settling time of the temperature. The orange dashed line indicates the average time interval between scans.

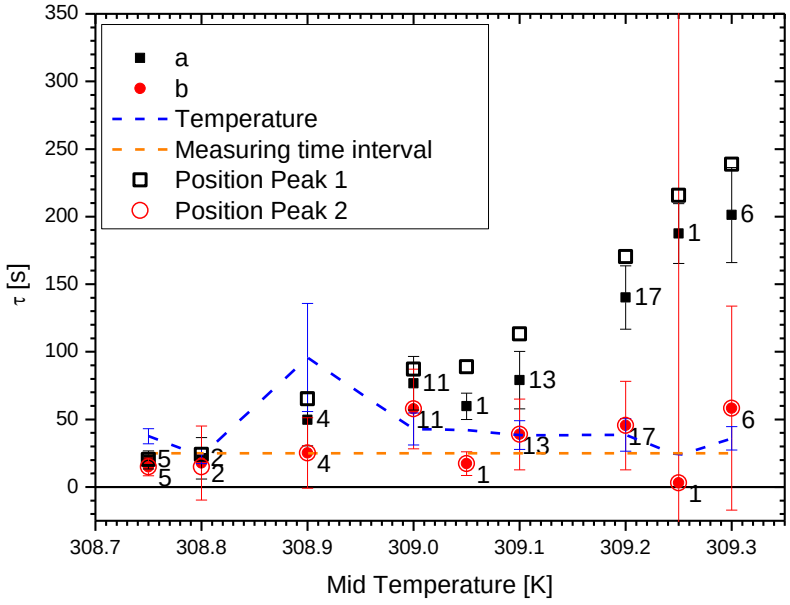

Figure 92: Average relaxation times for the lattice parameters over temperature. Hollow symbols show the average relaxation times for the position of the peaks. Numbers next to data points indicate the number of measurement over which was averaged. The blue dashed line indicates the average for the settling time of the temperature. The orange dashed line indicates the average time interval between scans.

By fitting the lattice parameter one can also check if fit parameters g_0 and χ_0 are reasonable. g_0 corresponds to the value of the corresponding lattice parameter at $T = 0$ K, χ_0 correspond to its slope as a function of temperature. To draw a comparison to previous measurements we can calculate its value at $T_{Ref} = 307$ K :

$$\bar{g}_0 = g_0 + \chi_0 \cdot T_{Ref} \qquad \text{(IV.27)}$$

Figure 93 depicts the calculated lattice parameters from the different averages of the temperature steps. As teal dashed line the values from the multistep experiments from table 7 is shown. The average values deviate marginally from these values (below 1%). The errors are considerable but this is mostly due to the narrow temperature window in which the fits were performed.

Figure 94 depicts the average generalized susceptibilities for the different temperatures For the a-axis the slopes χ_0 are still higher than those indicated table 4 and table 5 but lower than the one in table 7, which is indicated as teal dashed line. For the b-axis the values are rather corresponding to those of table 4 and table 5 than the one of table 7. The lattice parameters *a* and *b* show the same behaviour for step-like measurements as well as for slow cooling measurements. In summary different measurements of different samples at different times and with different evaluations yielded comparable results.

The relaxations which were observable in the calorimetric measurements are also observable in the x-ray measurements. It is important to note that it can be excluded that the relaxations are due to thermal resistances as the position of the peak 2 or b-axis in the lattice show an immediate response to the temperature steps. The dependency of the different parameters defining the peaks will be discussed in the following chapter.

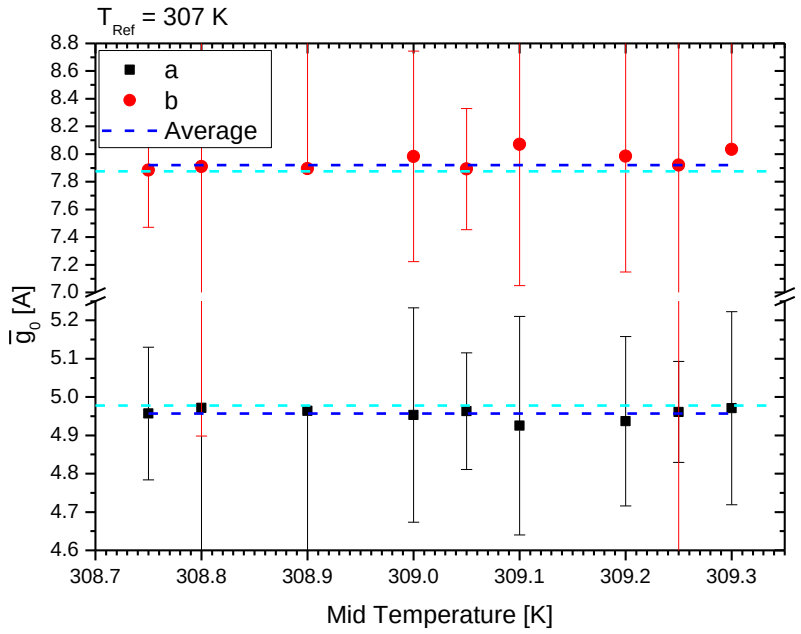

Figure 93: Reference lattice parameter for the measurement around different temperatures. Average values depicted as dark blue dashed lines. Teal dashed lines indicate the values at 307 K listed in table 7.

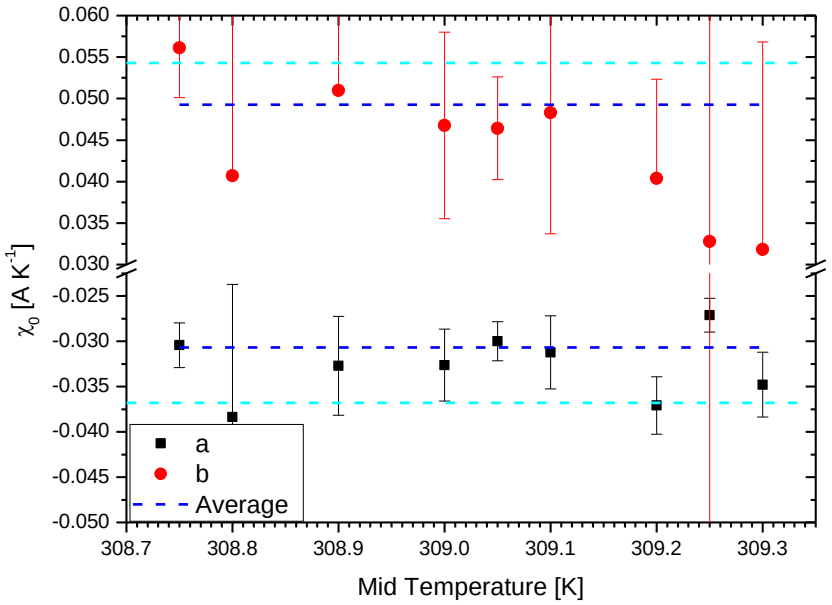

Figure 94: Generalized susceptibility for the measurement around different temperatures. Average values depicted as dark blue dashed lines. Teal dashed lines indicate the values at 307 K listed in table 7.

V. Discussion

In the previous chapter, results from measurements with calorimetry and X-ray diffraction on eicosane have been presented. In this chapter we proceed to a synthesis of these findings with known properties from literature. First, the reversibility of the processes presented in the previous chapters is discussed.

V.1. Reversibility

With the step experiments described in sub-chapter IV.2 it could be shown that for similar temperature steps the heat, which goes into or comes out of the sample is always the same. Deviations between measurements have been related to the position of the crucibles inside the DSC furnace. Especially with the tri-step experiment, the reversibility of the heat flow could be shown. Pak and Wunderlich [5] reported an increased apparent heat capacity for C26, C44 and C50 close below the melting temperature. For now no relation between the large values for the apparent heat capacity and heat flow found in the step experiments has been established. Therefore the specific enthalpy found during the step experiments is compared to the apparent heat capacity found with the TOPEM method. To calculate a "heat capacity" from the results of the step experiments, an average heat capacity change Δc_p is introduced:

$$\Delta c_p = \frac{\Delta h}{\Delta T} \qquad \text{(V.1)}$$

where Δh is the difference in specific enthalpy measured for a temperature step of

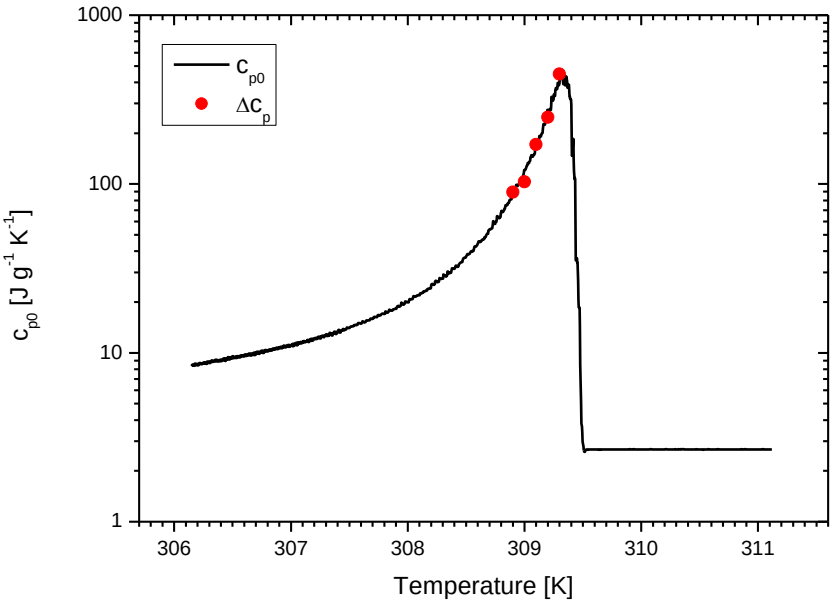

Figure 95: Comparison of the temperature dependences of the specific heat capacities obtained from TOPEM (black line) and calculated from DSC step experiments according equation V.1.. The data stem from measurements on a C20 sample with mass m = 8.5mg and purity 99.0+%.

size ΔT. Figure 95 allows to compare the heat capacities derived from the step experiments and those obtained from TOPEM measurements for a C20 sample of mass 8.5 mg and purity 99.0+%.

The good consistency of both temperature dependences in figure 95 leads to the conclusion that the heat flow due to changes of the specific heat capacity and the one resulting from possible latent heat exchanges during a phase transition cannot be distinguished: as a matter of fact, the observed heat flow is completely reversible. It should be stressed that this holds only true because the heat capacity measured by the TOPEM method corresponds to a quasi-static susceptibility, i.e. the measurement is done at very low frequencies. If one measured the heat capacity at higher frequencies, e.g. with conventional TMDSC, one would obtain lower values since the processes occurring in the experimental temperature range show certain kinetics (please see detailed discussion below). In figure 96 the total, reversing and non-reversing heat fluxes calculated from a TOPEM measurement of the same sample as in figure 95 are depicted. In line with the argumentation above, the reversing heat flux calculated from this measurement is equal to the total heat flux up to at least 309.3 K. Closer to the transition the non-reversing part of the heat flow becomes erratic. This is mostly linked to the appearance of an non-reversing (latent) contribution. The evolution of the latter is too fast to be properly resolved [34].

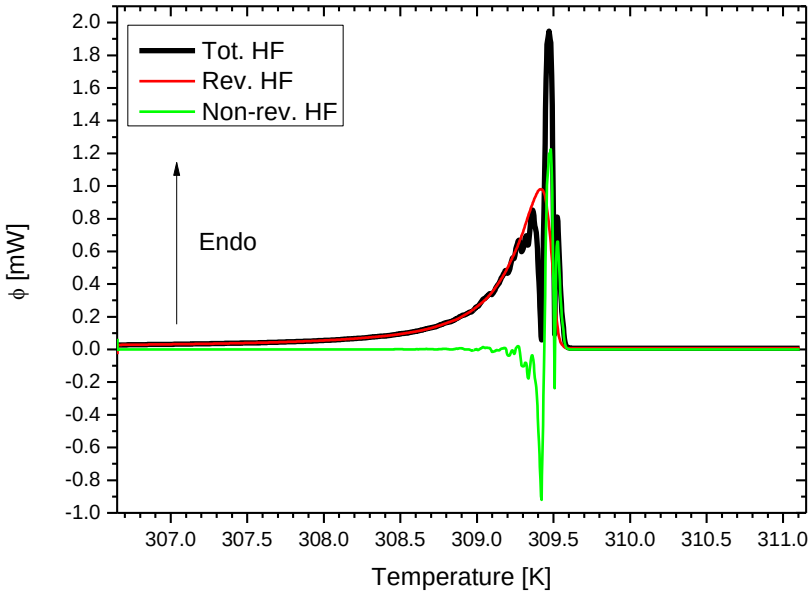

Figure 96: Temperature dependences of the total, reversing and non-reversing heat fluxes calculated for a C20 sample with mass *m* = 8.5mg and purity 99.0+%.

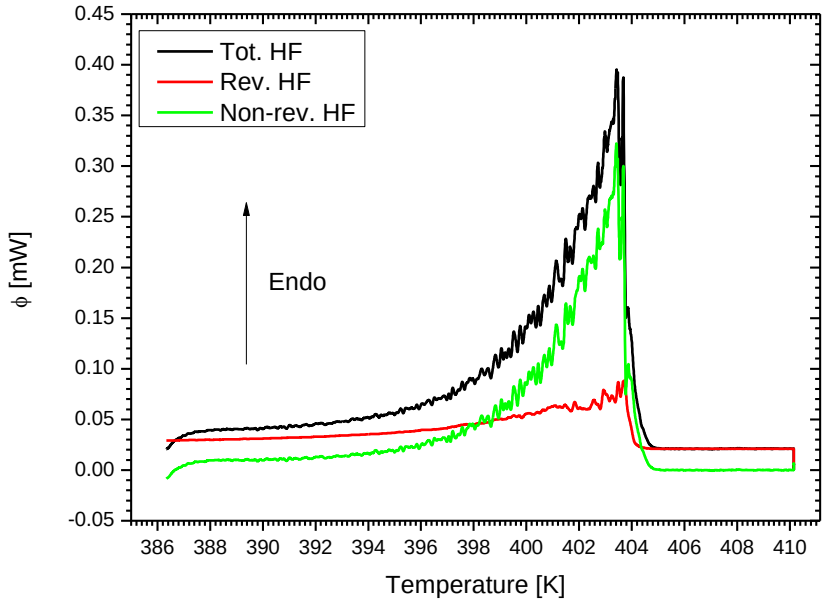

Figure 97: Total, reversing and non-reversing heat flow for a high density poly-ethylene with a mass of m = 10.60mg at the melting transition(weight averaged molecular weight M_w = 12500)

The comparison of the melting behaviour of a polymer and the one of C20 is illustrated in figure 97 and figure 96 respectively. For the polymer (high density poly-ethylene molecular weight M_W = 125000 g mol^{-1}) a reversing part of the heat flow above the one expected for skeletal vibrations can be observed in the semi-crystalline state [24]. Still the non-reversing part of the heat flow is the major contribution at the melting of the polymer. Pak and Wunderlich [5,28] argued that the reversing heat flux in polymeric material would relate to the melting of side chains or segments of the size of n-alkane molecules. Furthermore they refer to the low undercooling possibilities to explain why these segments can crystalize without secondary nucleation. As C20 displays an increase of heat capacity itself, without a detectable amount of molecules being in the liquid phase, the same process could also describe the behaviour in polymers. This would then mean that the increased apparent heat capacity in polymers could be related to conformational changes which push monomers out of the equilibrium lattice structure. Goderis et al. [71] showed a lamella thinning and thickening with temperature modulates small angle x-ray scattering which corresponds to the mechanism we observed in C20.

V.2. Relaxation times in the rotator phase

The relaxation times for the rotator phase for the C20 sample with low purity (99.0+%) have been acquired with different methods. These relaxation times are shown in figure 98. Obviously the results from the different measurements are in good agreement with each other. The accuracy of the temperature is ±0.2 K for each measurement type. The correspondence between the XRD and DSC/TOPEM suggests that the relaxation times determined above 309.3 K are measured in the coexistence region of the liquid and rotator phases as in XRD the liquid halo has been observed above this temperature (see figure 72). This would also explain, why for this temperature range deviations of the results obtained for samples with different masses have been observed as kinetics become relevant when a finite amount of material can melt. Furthermore a possible coexistence of the liquid and rotator phases could help explaining the increased error bars of the relaxation times in figure 98. Moreover the region of coexistence corresponds to the temperature range where the separation of reversing and non-reversing heat fluxes becomes erratic (see figure 96).

As it is very improbable that the device response functions of the DSC and the XRD are identical, the coincidence of the relaxation times obtained from both experimental techniques suggests that the observed relaxation times are intrinsic to the C20 samples. To attain a higher degree of certainty concerning the alignment of

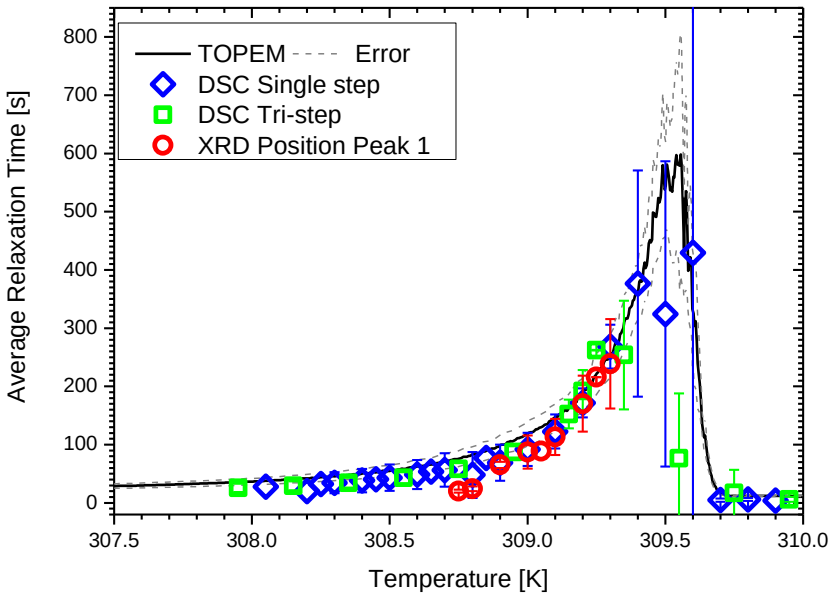

Figure 98: Relaxation times in the rotator phase of a C20 sample of low purity (99.0+%) as obtained from different measuring techniques. Errors bars and lines are obtained from the standard deviations between the data for different masses. For the XRD relaxation times the error was calculated as described in sectionIV.4.3.

the temperature scales of different experimental methods, a combined system of DSC and XRD would be ideal.

Irrespective of the accuracy of the temperature, the increase of the relaxation times is observable in all methods. As the increased relaxation times are not observed for peak 2 and the *a*-axis couples to longitudinal movements (along the molecule axis) [30] we can conclude that the lateral direction in the layers can probably adjust fast to temperature changes. Moreover the experimental fact that peak 2 quickly reacts to temperature changes excludes the possibility that the relaxation time is linked to the settling time of the temperature in the sample itself.

V.3. Premelting versus reversible melting

The question remains which kind of phenomena we are observing. It is clear that the transition from the liquid to the rotator phase is of first order, as a discontinuity in symmetry can clearly be observed.

On the other hand the complete lack of an amorphous, liquid background in the X-ray data in the temperature range where the lattice structures and also the heat capacities display relaxation behaviour (see figure 71), shows that the observed kinetics is not due to melting. Effects such as the decrease of the areas of the diffraction peaks with rising temperature are due to the increase of defects in the crystalline structure on approaching the melting temperature. This is in line with observations in literature that gauche defects are accumulating at the end of the chains [19] and thus a decoupling of the layers can be observed [72]. This could be the cause for the halo observed below peak 1 and 2. To further investigate this aspect, small angle scattering techniques would be necessary.

To summarize, at least to a temperature of 309.3 K, the description of the phenomena as reversible premelting instead of reversible melting is more accurate mainly due to the lack of a measurable liquid phase.

V.4. The mechanism

From the preceding paragraph, it is clear that to some extend the rising amount of gauche defects is the driving force for the conformational disorder [19,20]. As trans-gauche transitions are activated processes [21] the characteristic times for the transitions should drop with increasing temperature. This is why for processes occurring along the lateral direction (as depicted by the position of peak 2) the relaxation times remain practically constant for all temperatures. On the other hand the position of peak 1 shows increasing relaxation times. Additionally the increase in specific heat capacity has been related to conformational disorder appearing also in the low temperature crystal structure [45,73]. These conformational defects exert an effective pressure inside the crystal structure which softens the system [74]. Strobl et al. [14] already discussed that screw jump motions [17] exert an inter-lamellar pressure. Ungar [30] argued that the decrease of the short *a*-axis is related to a weakening of oscillatory movement around the equilibrium lattice position along the *a*-axis as a consequence of increasing freedom of movement along the *c*-axis. The latter argument hints to the complicated interplay between processes along the longest axis and lateral directions in the lattice structure [19].

One possible explanation, for the increasing relaxation times, could be that some defect cooperativities between chains are needed to form them. Especially if kinks are moving closer to the centre of the chain, molecules deviate more from their planar configuration [20]. With rising temperature more defects emerge. As an increasing number of defects requires a larger cooperative volume, the probability for defect formation decreases. As a result, the characteristic times needed for the equilibrium to be established after temperature changes grow. This mechanism is not only linked to the rotator phase. Therefore the increase in the relaxation times can also be observed in the triclinic phase. As the integration of impurities created more free space around the ends of the molecules, it is clear that samples with more impurities can adopt a higher degree of disorder already at low temperatures.

Figure 99 depicts the relaxation times in an Arrhenius plot. For a regular activated process an upward slope would be expected. The relaxation times where fitted with an empirical Arrhenius-like function with a divergence temperature T_0:

$$\tau = A \cdot \exp\left(\frac{B}{T_0 - T}\right) \tag{V.2}$$

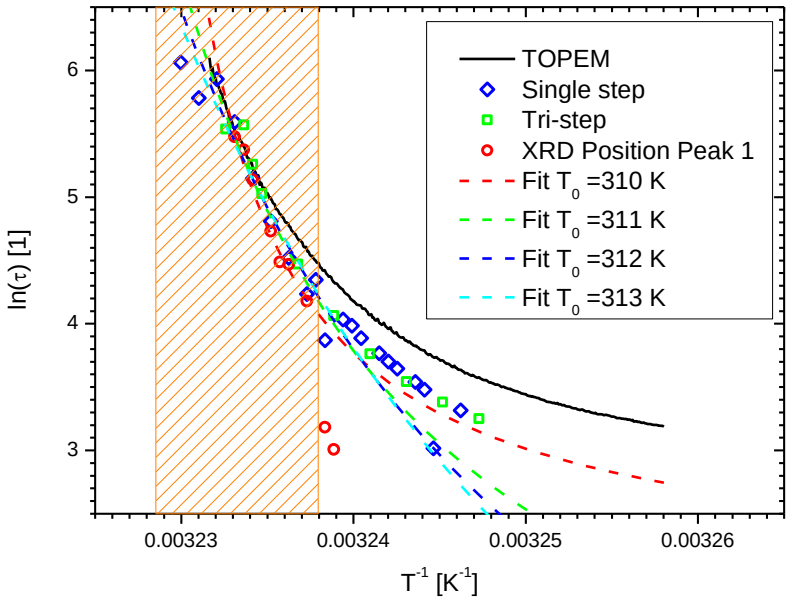

Figure 99: Arrhenius plot of the relaxation times depicted in figure 98.

where *A* and *B* are fit parameters whose physical meaning are unclear up to now. The orange area depicts the data range which was used for the fits to avoid the impact of the device related characteristic times. The relevant aspect of these fits is that with rising divergence temperature T_0, they better describe the trend of the data. This is similar to the extrapolation of the distortion parameter in section IV.4.2. Although these are pure empirical models, the aspect that a critical temperature for both characteristics (hexagonal lateral conformation and relaxation time divergence) exists with a similar value, should motivate further theoretical and experimental investigations.

VI. Conclusion

N-alkanes are often used as model systems for polyethylene or more generally for polymers. However, the presented results show that compared to polymers, n-alkanes exhibit different behaviour close to the transition from and to the liquid phase. When cooling polymers below the melting temperature, two competitive processes are usually found: On one hand there is the straightening of the molecular chains necessary to transform into the crystalline phase. This process is driven by the reduction of free energy. On the other hand there is the opposite effect, i.e. the creation of conformational disorder driven by the increase of entropy and favoured by steric constraints. This leads to the formation of a semi-crystalline structure.

Most of the work done in the frame of this PhD project focused on the investigation of the melting process of eicosane. For many materials the melting temperature is sharply defined. For examples metals like indium show a transition in a temperature interval smaller then 0.1K [75]. In contrast, polymers, like polyethylene, can exhibit a melting range spreading over several 10 degrees. Within this melting range, the amount of amorphous (liquid) phase generally increases with increasing temperature - at the expense of the crystalline phase. Thus the degree of crystallinity depends on temperature. In quasi-static DSC experiments in which the temperature is only slightly varied around an isotherm the heat capacity can exceed values expected from vibrational contributions [26,28]. This additional contribution is attributed to partial reversibility of the crystallinity and therefore referred to as reversible melting.

In this work XRD and DSC measurement were exploited to characterize the metastable rotator phase of n-eicosane close to the transition to the liquid phase. A lot of effort has been put into the ability to combine the results of both methods. First, the major findings will be briefly addressed. Then the experimental evidences leading to these findings will be recapitulated followed by a more detailed discussion. Finally open questions will be addressed along with an outlook for future research.

1. It could be shown that there is no observable liquid phase in the melting range of eicosane. Therefore this temperature range is better referred to as premelting then reversible melting. This sets the behaviour of n-eicosane below the melting temperature clearly apart from the one of polyethylene despite all other similarities.
2. Additionally it could be shown that each temperature change in the rotator phase close to the melting temperature is accompanied by relaxation processes observable both in crystal structure as well as in heat absorption or emittance. Therefore it can be concluded that the premelting range can be described as a range where structural relaxations occur with a tendency to isotropisation with increasing temperature. The question whether this isotropisation is restricted to inter-lamellar regions or if it also affects the intra-lamellar structure remains open.

3. Another main finding of the present work is the fact that the enthalpy production/absorption depicted by the calorimetric measurements is completely reversible in the rotator phase. This holds true for both short and long timescales. As a consequence, refinement of the crystalline structure with time, which is often observed for polymers, can be excluded for n-eicosane.
4. A further important aspect of the reported relaxation process is the fact that the same relaxation times can be observed both for enthalpy production and absorption. This behaviour diverges from the one expected for crystallisation or melting processes: Molecular systems usually show different kinetics of crystallisation and melting - even when reversible melting can be found.

VI.1. Premelting versus reversible melting

XRD measurements revealed that a broad characteristic peak associated to the liquid phase appears in a heating experiment almost instantly (in a temperature interval of 0.1K, see section IV.4.2. Nevertheless the onset of the steep increase of the apparent heat capacity as well as of the structural and thermal relaxation times emerges around 1K below the melting temperature. The combination of XRD and DSC results shows that the increased apparent heat capacity is not related to an exchange of molecules between the liquid and the rotator phase. Therefore the excess enthalpy cannot be used to calculate the crystallinity [36]. Since molecules in the layers are tending to a more hexagonal, more isotropic structure with increasing temperature (see section IV.4.2), one can describe this phenomenon as a pre-cursor of the melt and therefore refer to it as premelting.

VI.2. Dynamics of premelting

The XRD measurements display both, an almost instantaneous and a relaxing response of the structure of the rotator phase to temperature perturbations. The two time scales prove that the relaxation process itself is an intrinsic property of the samples and that it is not related to instrumental time constants.

The most prominent aspect of the dynamics of premelting is the increase of relaxation times on approaching the melt. For a kinetic process like undercooled crystallisation it is common that the speed of crystallisation increases the further the sample is away from the melting temperature [76]. However inside the rotator phase we do not observe an ongoing process like crystallisation or melting but we are rather looking at a structural relaxation.

VI.3. Reversibility of the premelting

The DSC measurements revealed that the enthalpy is reversible in the premelting regime (see section IV.2.2). A crucial additional insight delivered from this work, is the lack of a hysteresis in the enthalpy, after an initial crystallisation into the rotator phase. Especially when approaching and retreating from the melting temperature the enthalpy values are reproducible at each temperature. This sets eicosane clearly

apart from polyethylene which displays time and temperature dependent refinement of the crystalline structure[26].

The reversibility is also observed in the structure of the rotator phase (see section IV.4.2). With the absence of a liquid phase, as mentioned before, it is clear that the premelting behaviour differs from the reversible melting of polymers. The different behaviour is caused by the different length of the molecules. Both n-alkanes and polymers form layered systems. Polymers have a lamella structure with alternating crystalline and amorphous phase, whereas n-alkanes create layers with a width around the chain length. In a temperature modulated experiment polymers show a corresponding variation of the layer thickness of the crystalline and amorphous phase [71]. For n-alkanes on the other hand the spacing relates to a roughening of the layer surface [16] caused by increased oscillatory movement of the molecules [21] and/or conformational disorder [19].

VI.4. Reversibility of the dynamics of premelting

DSC and XRD both showed that reversibility can also be observed in the dynamics of the relaxation process. Small temperature modulations superposed to an isothermal measurement reveal the same relaxation times for the cooling and heating parts of the modulation. This holds true for both structure as well as enthalpy relaxations. Regarding conventional crystallisation, primary nucleation for initiation and secondary nucleation for crystal growth are needed. Primary nucleation is often accompanied by undercooling effects. For a molecule to detach from the crystallite, its energy only needs to exceed the binding energy. Therefore the observed reversibility of the relaxation dynamics is completely unexpected. The identity of the relaxation times for both heating and cooling steps points to an activated process with negative activation energy. As mentioned above for the general case, this activated process is governed by the interplay of entropic and energetic forces.

VI.5. Outlook

Preliminary measurements carried out in the rotator (RI) phase in C19 and C21 exhibit the similar relaxation behaviour as C20. Further investigations on uneven n-alkanes from C9 to C21 would allow assessing how the chain length impacts the relaxation behaviour. As these materials have a rotator phase which is stable on larger timescales they are also good candidates to be examined by other experimental techniques.

To better characterize the structural relaxation, temperature modulated small angle x-ray scattering can be used. This method would allow observing if the relaxation also takes place in the layer spacing. Another improvement of the structural characterisation could be done with a faster scan speed in a wide angle x-ray scattering experiment. This would then allow to broaden the angular range measured in one scan and so to add more peaks for the evaluation of the structural relaxation.

To assess the relation between the structural relaxation and the conformation of the molecules time resolved temperature modulated infrared spectroscopy could be employed. This technique would allow seeing if the temperature dependence of intensity for certain wave lengths of particular molecular vibrations would correlate with the increasing relaxation times presented in this study.

Appendix

A. DSC equivalent circuit for modulated measurements

The equivalent circuit depicted in section II.1.1 figure 2 can be resolved for temperature modulated measurements. For this we only consider a simple oscillating modulation of the furnace temperature ΔT_F^*

$$\Delta T_F^* = \Delta T_{mod} \exp(i\omega t) \tag{A.1}$$

where the physical quantity is the real part of $\mathrm{Re}(\Delta T_F^*)$, ΔT_0 an amplitude and ω the modulation (angular) frequency. When the stationary state is achieved every varying quantity in the system oscillates with ω. So will also the measured temperature difference:

$$\Delta T_M^* = \Delta T_{M,0}(\omega) \exp(i(\omega t - \delta(\omega))) \tag{A.2}$$

where the amplitude $\Delta T_{M,0}$ and phase shift δ are functions of all the elements in the circuit, the amplitude and the angular frequency of the furnace temperature. Kirchhoff's 1st and 2nd law state that the sum of currents or in our case heat flows in a junction and the sum of all voltages or our case temperature differences in a loop are zero respectively. One can establish the following equations (see figure 2):

1) $$R_{FMS}\left(\dot{Q}_S + \phi_{S,mod}^* + \dot{Q}_{FMS} + \dot{Q}_{MM}\right) + R_{MM}\dot{Q}_{MM} - \dot{Q}_{FMR,1}R_{FMR} = 0 \tag{A.3}$$

2) $$\dot{Q}_{FMR,1}R_{FMR} + \frac{Q_{FMR,2}}{C_{FMR}} - \Delta T_F^* = 0 \tag{A.4}$$

3) $$\Delta T_M^* - R_{MM}\dot{Q}_{MM} = 0 \tag{A.5}$$

4) $$Q_{MM} + Q_{FMR,1} = Q_R + Q_{FMR,2} \tag{A.6}$$

5) $$R_{MR}\dot{Q}_R + \frac{Q_R}{C_R} - \frac{Q_{FMR,2}}{C_{FMR}} = 0 \tag{A.7}$$

6) $$\frac{Q_{FMS}}{C_{FMS}} - \frac{Q_R}{C_R} - R_{MR}\dot{Q}_R - \Delta T_M^* = 0 \tag{A.8}$$

7) $$R_{MS}\left(\dot{Q}_S + \phi_{S,rev}\right) + \frac{Q_S}{C_S} - \frac{Q_{FMS}}{C_{FMS}} = 0 \tag{A.9}$$

with $\dot{Q}_i = i\omega Q_i$ the following reductions can be made:

1&2&3 &5&6: $$R_{FMS}\left(\dot{Q}_S + \phi_{S,mod}^* + \dot{Q}_{FMS}\right) + \frac{R_{FMS}}{R_{MM}}\Delta T_M^* + \frac{Q_{FMS}}{C_{FMS}} - \Delta T_F^* = 0 \tag{A.10}$$

4&2&3 &5&6 $$\frac{Q_{FMS}}{C_{FMS}} = \frac{\left(\frac{R_{FMR}}{R_{MM}} + \frac{i\omega C_R R_{FMR}}{1 + i\omega C_R R_{MR}} + 1 + i\omega C_{FMR}R_{FMR}\right)\Delta T_M^* + \Delta T_F^*}{\frac{i\omega C_R R_{FMR}}{1 + i\omega C_R R_{MR}} + 1 + i\omega C_{FMR}R_{FMR}} \tag{A.11}$$

combining (A.9), (A.10) and (A.11) we finally get:

$$\frac{\Delta T_M^*}{\Delta T_F^*} = \frac{[W_R^* - W_S^*] - W_R^* \dfrac{R_{FMS} \cdot \phi_{S,mod}^*}{\Delta T_F^*}}{W_R^* \cdot W_S^* + \dfrac{R_{FMR}}{R_{MM}} W_S^* + \dfrac{R_{FMS}}{R_{MM}} W_R^*} \tag{A.12}$$

with

$$W_S^* = \left(\frac{i\omega\tau_{S,FMS}}{1 + i\omega\tau_S} + i\omega\tau_{FMS} + 1\right) \tag{A.13}$$

$$W_R^* = \left(\frac{i\omega\tau_{R,FMR}}{1 + i\omega\tau_R} + i\omega\tau_{FMR} + 1\right) \tag{A.14}$$

where $\tau_S = C_S R_{MS}$; $\tau_R = C_R R_{MR}$; $\tau_{FMS} = C_{FMS} R_{FMS}$; $\tau_{FMR} = C_{FMR} R_{FMR}$; $\tau_{S,FMS} = C_S R_{FMS}$; $\tau_{R,FMR} = C_R R_{FMR}$. This allows in general the separation of parts relating to the heat capacity C and parts relating to the reversible latent heat production or absorption $\phi_{S,rev}$:

$$\left[\frac{\Delta T_M^*}{\Delta T_F^*}\right]_C = \frac{[W_R^* - W_S^*]}{W_R^* \cdot W_S^* + \dfrac{R_{FMR}}{R_{MM}} W_S^* + \dfrac{R_{FMS}}{R_{MM}} W_R^*} \tag{A.15}$$

$$\left[\frac{\Delta T_M^*}{\Delta T_F^*}\right]_{\phi_{S,rev}} = \frac{-W_R^* \dfrac{R_{FMS} \cdot \phi_{S,mod}^*}{\Delta T_F^*}}{W_R^* \cdot W_S^* + \dfrac{R_{FMR}}{R_{MM}} W_S^* + \dfrac{R_{FMS}}{R_{MM}} W_R^*} \tag{A.16}$$

In general $\phi_{S,mod}^*$ is a function of temperature *T,* modulation amplitude ΔT_F^* and angular frequency ω. Therefore if such a process is investigated one has to check for linearity $\frac{\phi_{S,mod}^*}{\Delta T_F^*} = \text{const.}$.

In the zeroth approximation (A.15) reduces to

$$\left[\frac{\Delta T_M^*}{\Delta T_F^*}\right]_C = \frac{1}{(1 + i\omega C_S R)} - \frac{1}{(1 + i\omega C_R R)} \tag{A.17}$$

with a sample pan and reference pan of same mass $C_S = \tilde{C} + mc_p$; $C_R = \tilde{C} + \delta C$ with $\tilde{C}$ the mass of the sample pan, mc_p mass and specific heat capacity of the sample and δC an asymmetry term the ratio of the amplitudes can be reduced to:

$$\left|\left[\frac{\Delta T_M^*}{\Delta T_F^*}\right]_C\right| = \frac{\Delta T_{M,0}(\omega)}{\Delta T_{mod}} = \frac{R \cdot \omega\left(mc_p + \delta C\right)}{\left(1 + i\omega^2 \tilde{C}^2 R^2\right)} \frac{1}{\sqrt{1 + \dfrac{1 + i\omega^2\left(mc_p\right)^2 R^2}{1 + i\omega^2 \tilde{C}^2 R^2}}} \tag{A.18}$$

B. Parameter check for TOPEM

The TOPEM method relies on several controllable measuring and evaluation parameters. It is important to assess their impact onto the results to avoid artefacts and ensure that the results are related to C20 and not the measuring method or instrument. We have checked the following parameters

- Measurement
  - Modulation amplitude (linear regime)
  - Pulse length
  - Underlying heating rate
  - Starting temperature (memory effect)
- Evaluation
  - Evaluation window (data range for the evaluation algorithm)
  - Smoothing window (before Fourier analysis)

The impact of these parameters will be discussed in the following section.

Linear regime

Before realizing modulated measurements of any kind it is important to fix the linear regime. The linear regime describes the amplitude range for which the response (in our case heat flux) is proportional to the excitation (in our case temperature variation). In case of TOPEM the proportionality factor is the quasi-static specific heat capacity c_{p0} (see section II.1.2). Non-linear behaviour can also appear in the phase shift. This would then impact on the relaxation time τ found by the Debye fit of the complex heat capacity.

Amplitude sweep experiments were done at different temperatures to check for the linear regime. An exponential amplitude increase was chosen to cover a large amplitude range with five amplitudes per decade. Four reference temperatures T_{Ref} were chosen in the rotator phase around which the amplitude was increased stepwise every 10 minutes. Each test in the the rotator phase started in the liquid phase at 323.15 K. The sample temperature was then lowered to the value of interest in two steps. At this temperature it was kept for 30 minutes thus making sure that the first order transition to the rotator phase was completed. A typical temperature program is depicted in figure 100. The resulting heat flux is shown in figure 101.

Figure 102 and figure 104 show the evolution of the evaluated quasi-static specific heat capacity c_{p0} for C20 samples of mass m = 8.22 mg and m = 19.09 mg respectively as a function of the amplitude. For each reference temperature an increase of the c_{p0} values can be seen up to an amplitude a = *0*.158 K. In the range extending from a = 0.158 K to a =0.398 K, c_{p0} is almost constant. This range therefore represents the linear regime.

Figure 103, figure 105 and figure 107show the evolution of the relaxation times as a function of the modulation amplitude for C20 samples with different masses and

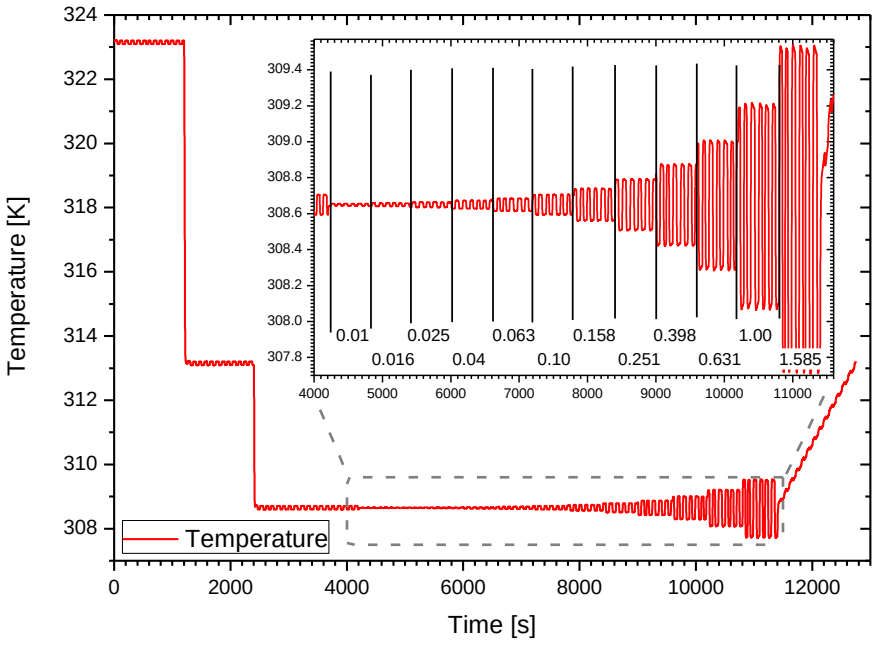

Figure 100: Temperature profile for an amplitude sweep experiment with the TOPEM method. Amplitudes scale exponentially. Amplitudes which are indicated are in K.

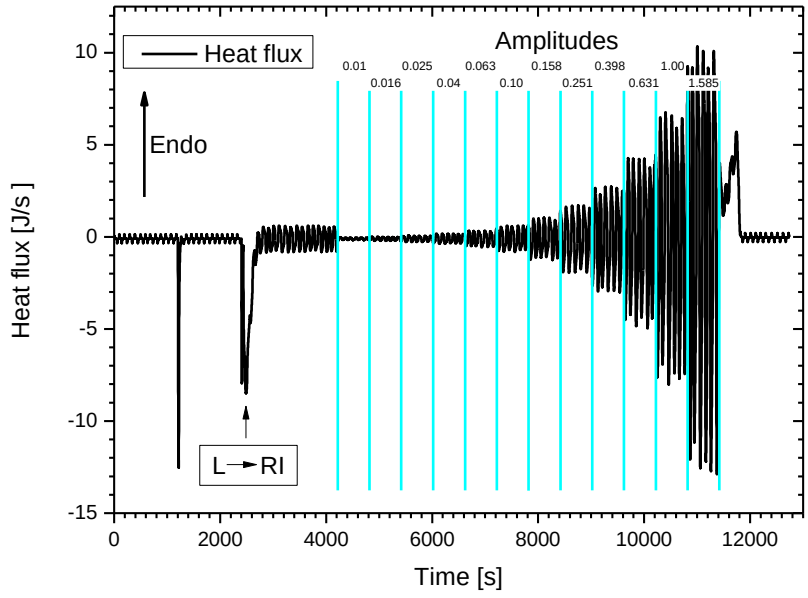

Figure 101: Heat flux for an amplitude sweep experiment. Amplitudes which are indicated are in K.

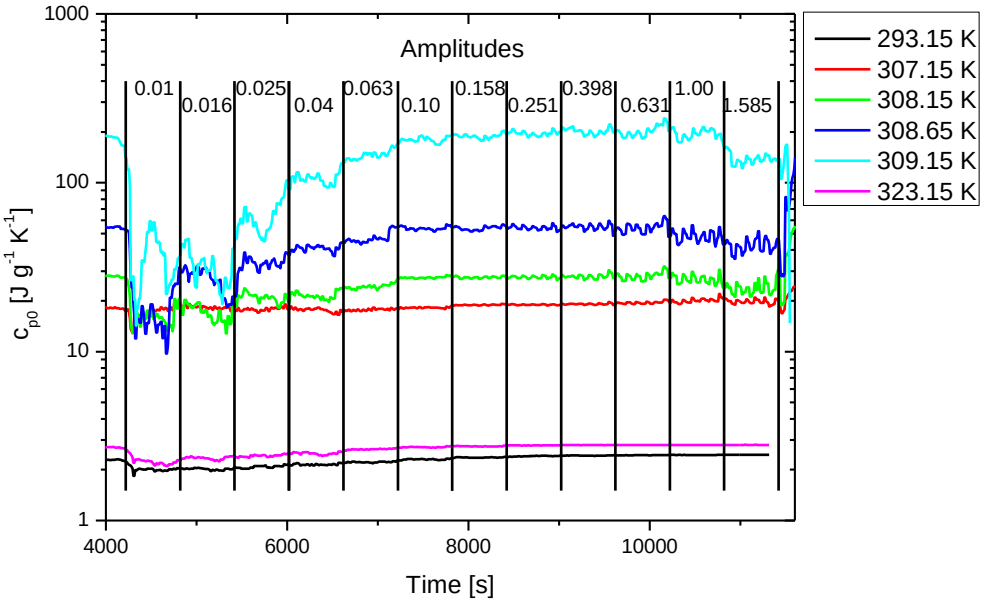

Figure 102: Quasi static heat capacities c_{p0} for an amplitude sweep experiment of a C20 sample with mass m=8.22mg and purity of 99.0+%. Reference temperatures are indicated in the legend. Amplitudes which are indicated are in K.

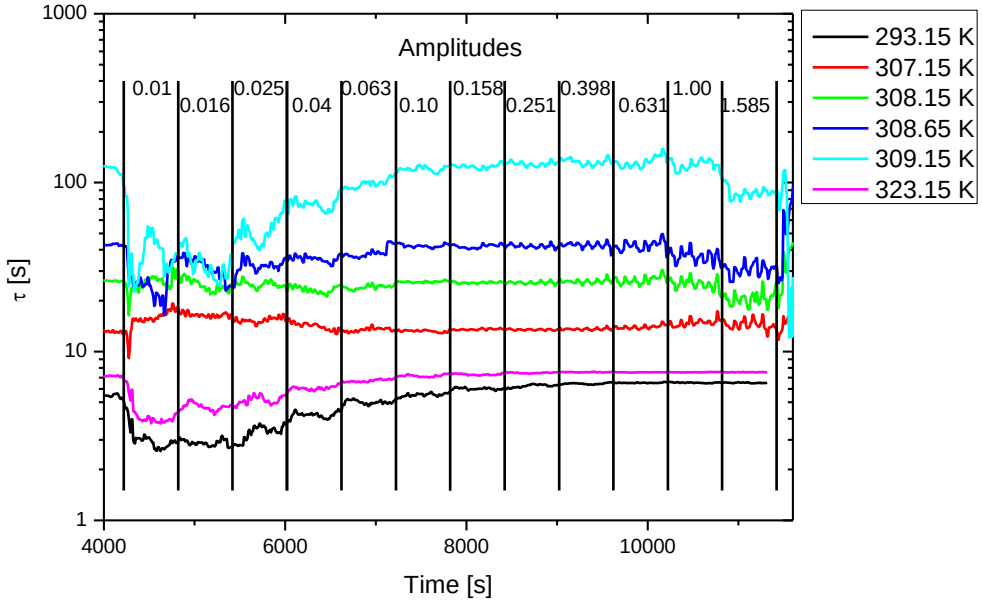

Figure 103: Relaxation time τ for an amplitude sweep experiment of a C20 sample with mass m=8.22mg and purity of 99.0+%. Reference temperatures are indicated in the legend. Amplitudes which are indicated are in K.

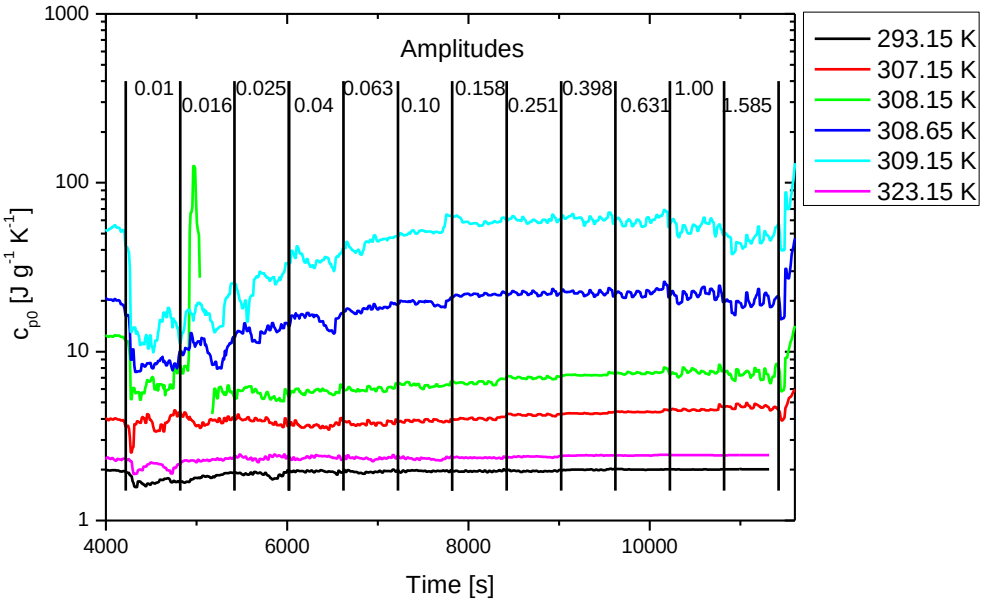

Figure 104: Quasi static heat capacity c_{p0} for an amplitude sweep experiment of a C20 sample with mass m=19.09mg and purity of 99.0+%. Reference temperatures are indicated in the legend. Amplitudes which are indicated are in K.

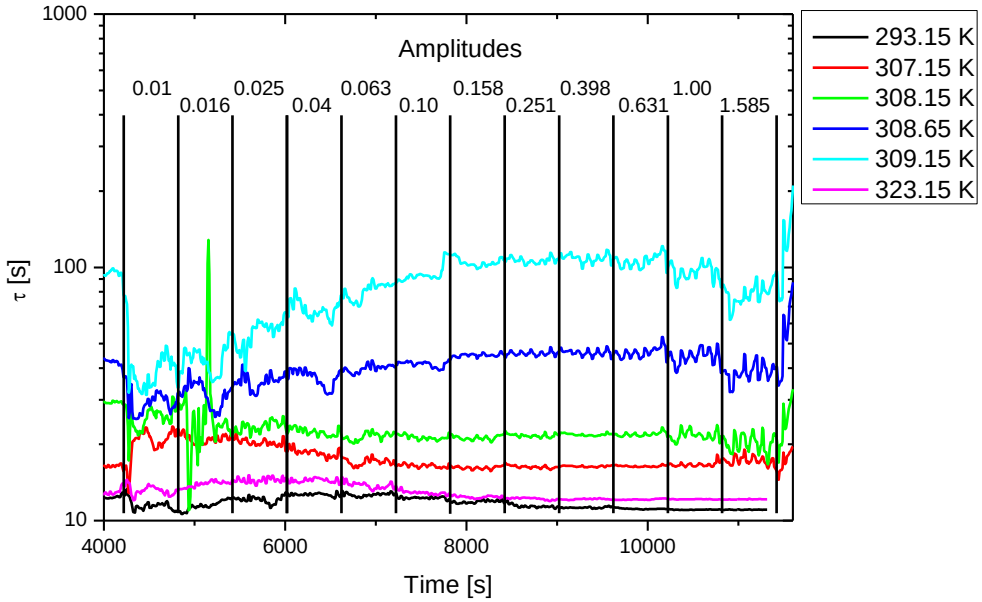

Figure 105: Relaxation time τ for an amplitude sweep experiment of a C20 sample with mass m=19.09mg and purity of 99.0+%. Reference temperatures are indicated in the legend. Amplitudes which are indicated are in K.

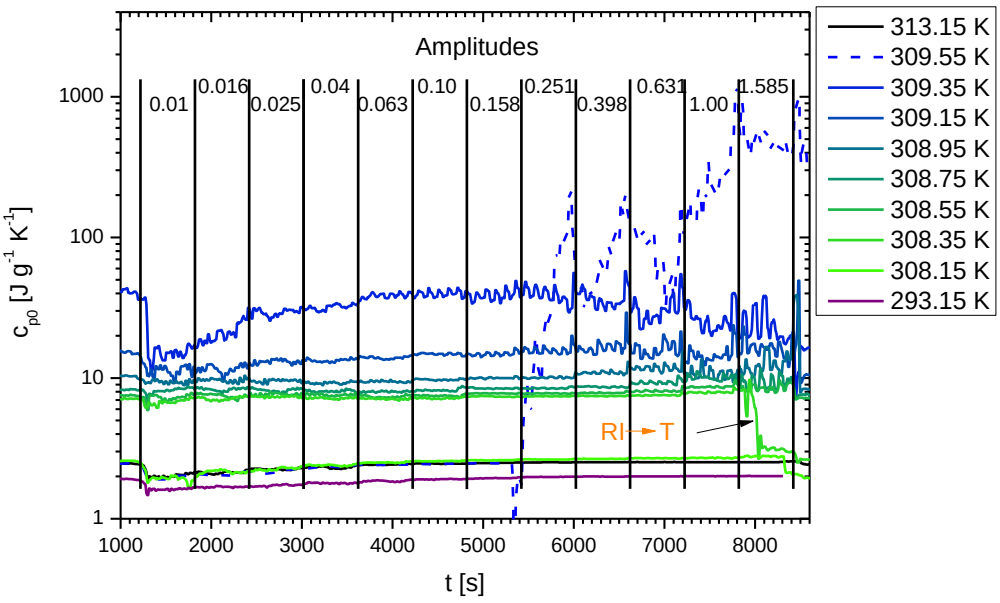

Figure 106: Quasi static heat capacity c_{p0} for an amplitude sweep experiment of a C20 sample with mass m=8.64mg and purity of 99.5+%. Reference temperatures are indicated in the legend. Amplitudes which are indicated are in K.

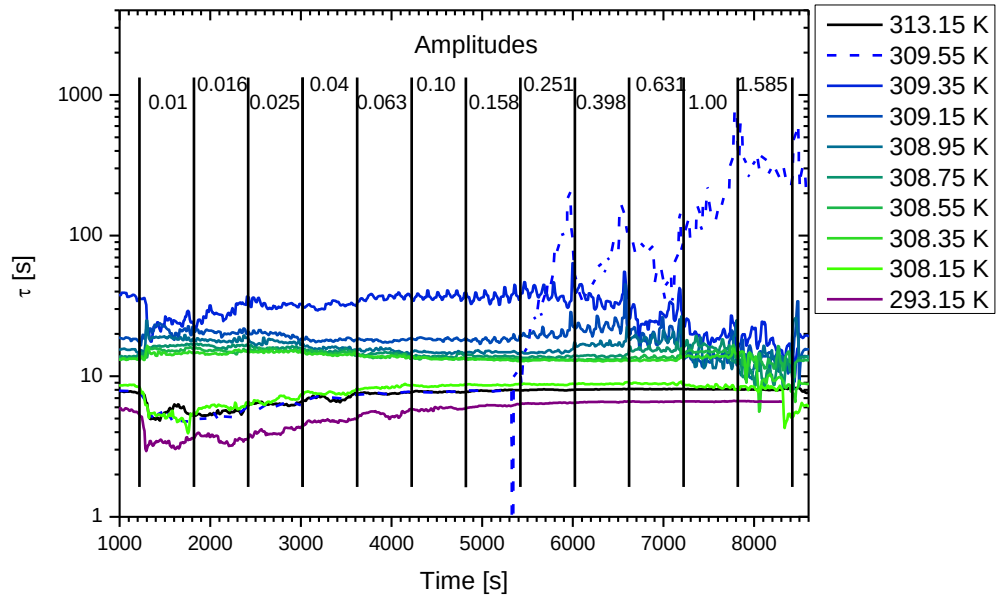

Figure 107: Relaxation time τ for an amplitude sweep experiment of a C20 sample with mass m=8.64mg and purity of 99.5+%. Reference temperatures are indicated in the legend. Amplitudes which are indicated are in K.

purities. For each sample, the relaxation times have been obtained from Debye fits of complex specific heat capacity data provided by a TOPEM amplitude sweep experiment. Obviously for amplitudes respecting linear regime the same relaxation times are constant.

For a C20 samples with a mass of m = 8.64 mg and purity of 99.5+% a different temperature program was employed. The first amplitude sweep was performed at 313.15 K. Then then the temperature was reduced to 309.55 K in a single step. The range from 309.55 K to 308.15 K was passed through using temperature steps of 0.2 K. A final amplitude sweep was realized at 293.15 K. For each temperature, the evolutions of c_{p0} and τ as a function of the modulation amplitude can be looked at in figure 106 and figure 107 . The dashed line indicates the reference temperature at which the sample crystallized. It is in agreement with the final melting temperature found in section IV.1.1. The transition to the triclinic phase occurs around 308.35 K. Irrespective of the temperature, linear regime conditions are respected for modulation amplitudes ranging between a = 0.063 K and a = 0.251 K.

Pulse length

The pulse length Δt_p describes the stochastic distributed time between two temperature steps in the TOPEM method (see section III.2). Therefore it is generally indicated as a time range. The default setting is $\Delta t_p = 20..40$s which is sufficient to investigate glass transitions or similar processes. It is necessary to check, if for the rotator phase this range can also be applied or an adjustment of the pulse length needs to be done.

In figure 108 and figure 109 the temporal evolutions of temperature and heat flux response are depicted for TOPEM measurements using different Δt_p 's for a sample of mass m = 8.5 mg and purity 99.0+%. The sample was cooled from 313.15 K to 306.15 K or 306.65 K and then heated up to 311.15 K. The underlying heating/cooling rate was $\beta_u = \pm 0.02\ \mathrm{K/min}$. The amplitude was chosen as $a = 0.25\ K$. The figures depict the behaviour close to the melting temperature of the rotator phase.

In case of the measurements with the shortest pulse length $\Delta t_p = 20..40$s, the heat flux is not reaching its maximum before the next temperature step (see encircled data on the lower left side of figure 108). Generally there is not enough time left for the heat flux signal to properly going to the relaxing behaviour before the next temperature step.

For the other pulse lengths (right side figure 108 $\Delta t_p = 40..60$s and figure 109 $\Delta t_p = 60..80$s and $\Delta t_p = 80..120$s) there is time enough for the heat flux signal to start relaxing after reaching a maximum or minimum. Nevertheless even for the longest time range $\Delta t_p = 80..120$s the heat flux does not fully relax to the baseline. Figure 19 in section IV.1.1 already hints that the time scale for the processes which are investigated is rather in the range of several hundreds of seconds then decades.

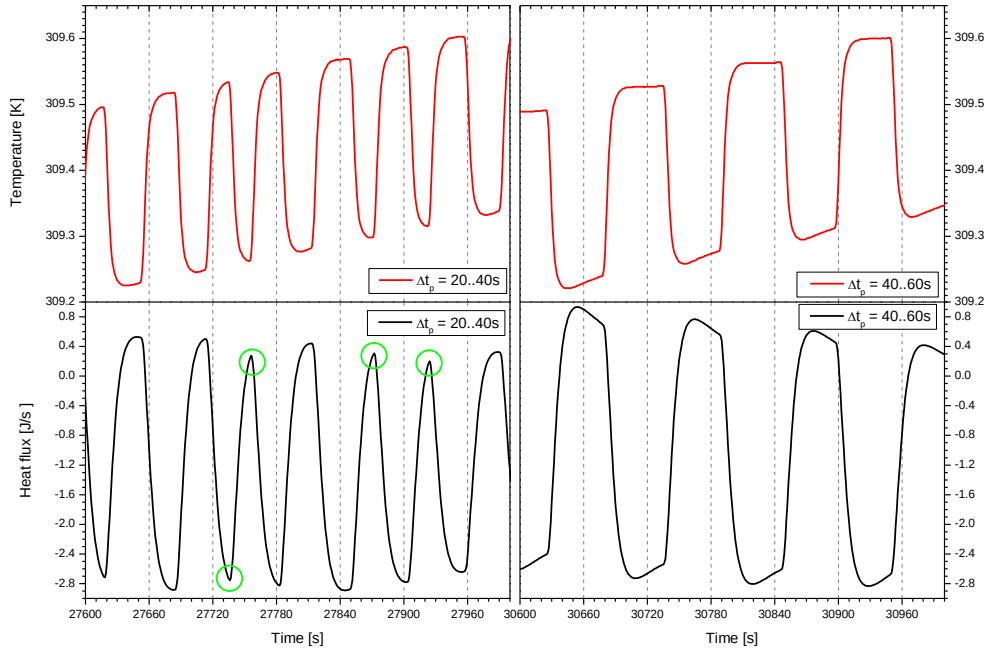

Figure 108: Temperature (top) and heat flux (bottom) for TOPEM measurements for experiments with different pulse lengths $\Delta t_p = 20..40s$ (left) and $\Delta t_p = 40..60s$ (right). Measurement were done with an amplitude a = 0.25 K and an underlying heating rate $\beta_u = 0.02$ K/min. The C20 sample has a mass of m = 8.5 mg and a purity of 99.0+%.

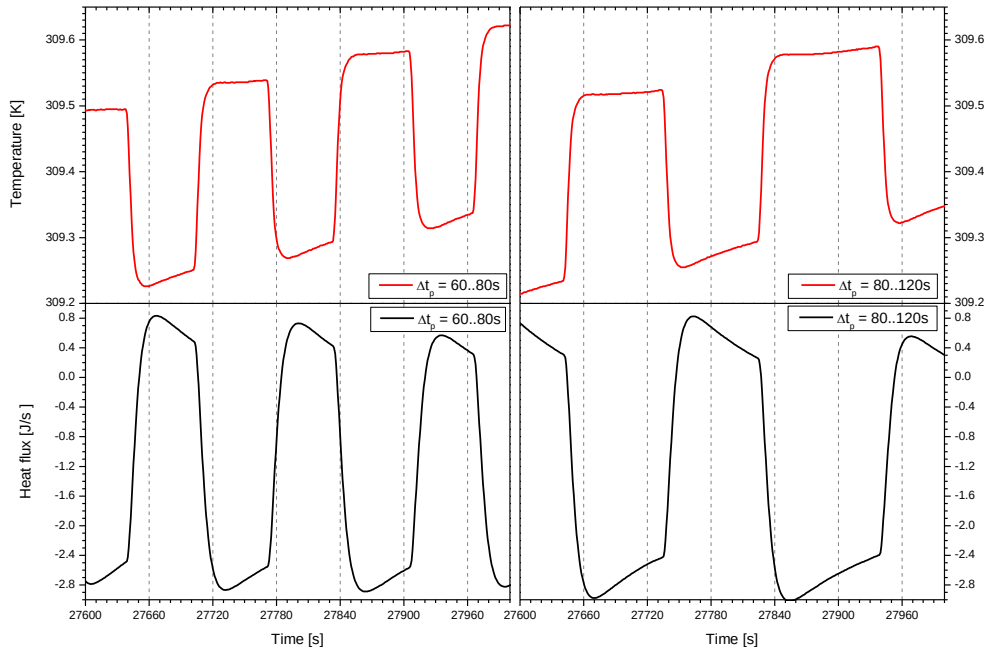

Figure 109: Temperature (top) and heat flux (bottom) for TOPEM measurements for experiments with different pulse lengths $\Delta t_p = 60..80s$ (left) and $\Delta t_p = 80..120s$ (right). Measurement were done with an amplitude a = 0.25 K and an underlying heating rate $\beta_u = 0.02$ K/min. The C20 sample has a mass of m = 8.5 mg and a purity of 99.0+%.

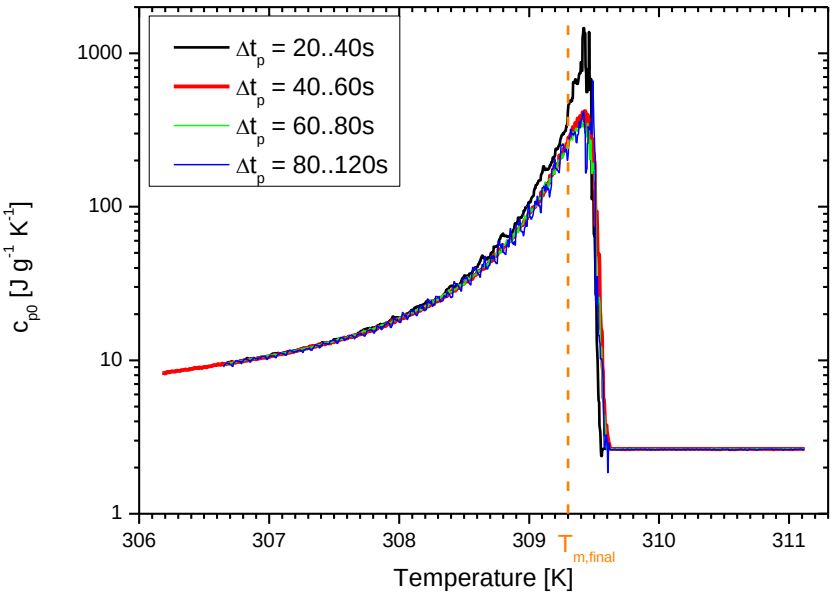

Figure 110: Quasi static heat capacity c_{p0} evaluated for measurements with different pulse length Δt_p for a C20 sample with mass of m = 8.5 mg and a purity of 99.0+%. A part of the raw data is depicted in figure 108 and figure 109.

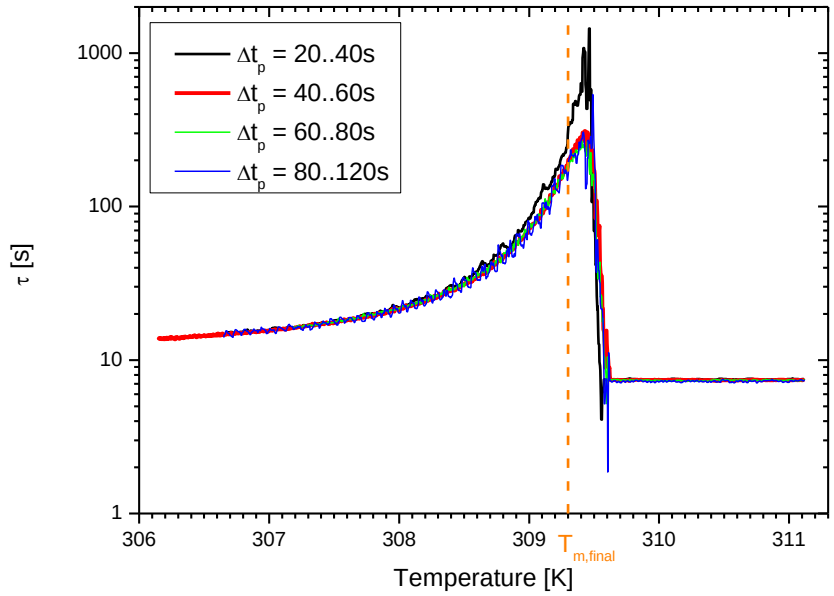

Figure 111: Relaxation time τ evaluated for measurements with different pulse length Δt_p for a C20 sample with mass of m = 8.5 mg and a purity of 99.0+%. A part of the raw data is depicted in figure 108 and figure 109.

In figure 110 and figure 111 show the evolution of the quasi-static heat capacity c_{p0} and the relaxation times τ respectively as a function of temperature are depicted for the different Δt_p. Data stem from measurement realized in the rotator phase of eicosane upon heating. For the shortest pulse lengths ($\Delta t_p = 20..40s$) both quantities c_{p0} and τ deviate from those obtained for the other ranges around the final melting temperature $T_{m,final}$. Although the deviation appears small on the graph it is considerable due to the logarithmic scaling. For the longer Δt_p there is no larger deviation visible; only the noise increases with the pulse length. This is mainly due to the interplay of modulation time and evaluation window (for these measurements 180s). It is interesting to note that the relaxation times are not dependent on the pulse length, if it is large enough. This means that in TOPEM experiments the range $\Delta t_p = 40..60$s can be used for the temperature pulse lengths to yield reliable data for the c_{p0} and τ. It has to be stressed that our evaluation relies on the hypothesis that the relaxation in C20 does not change its character at times larger than 120 s. Changes of the relaxation behaviour occurring beyond this time span cannot be detected with TOPEM.

For the part exceeding the final melting temperature one has to take into account the amplitude of the pulses which is a = 0.25 K. This means that for the reference temperature indicated a modulation of around ±0.14 K (see figure 10) has to be added. For this temperature range around the melting temperature 1st order reversible melting can be expected. For a high temperature pulse the sample is melting and for a low temperature pulse the sample is crystallising until the reference temperature is at least 0.14 K higher than the final melting temperature.

Underlying heating rate

As we are investigating the temperature dependent apparent heat capacity and relaxation behaviour close to a first order transition, it is important to investigate the influence of the underlying heating or cooling rate β_u on the measured quantities. Especially for the time-dependency it is necessary to separate it from the kinetics of the melting or crystallization process.

To assess the influence of β_u, a series of experiments with with different rates ($\beta_u = 0.01; 0.02; 0.05$ K/min) was performed. In each test the sample was cooled from 313.15 K to 306 K and subsequently heated to 311 K. A C20 sample with a mass of m = 19.09 mg and a purity of 99.0+% was chosen. Figure 112 and figure 113 show the temperature dependence of the quasi-static apparent heat capacity c_{p0} and the relaxation times τ respectively for the different rates β_u. Irrespective of the rate the data coincides at low temperatures in the rotator phase (T<309.3 K) and in the liquid phase (T>309.6 K) of C20. At the transition however the c_{p0} - and τ-peaks shift to lower temperatures with increasing cooling rate and to higher temperatures with increasing heating rate.

The trend set by the cooling rate clearly documents the influence of the kinetics of the 1st order transition from the liquid phase to the rotator phase As soon as this transition is completed the apparent heat capacity becomes rate independent.

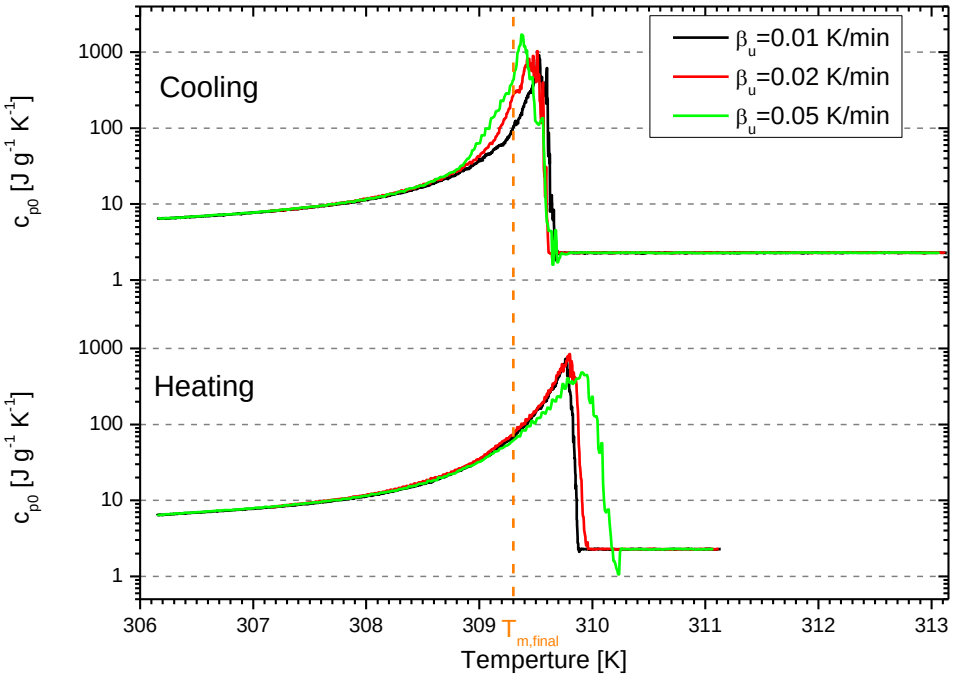

Figure 112: Quasi static apparent heat capacity c_{p0} for a C20 sample with mass m=19.09 mg and purity of 99.0+%. Measurements were done with different heating and cooling rates β_u indicated in the legend. Top: Cooling part of the measurement; Bottom: Heating part of the measurement. The indicated final melting temperature $T_{m,final}$ corresponds to the one of low purity samples.

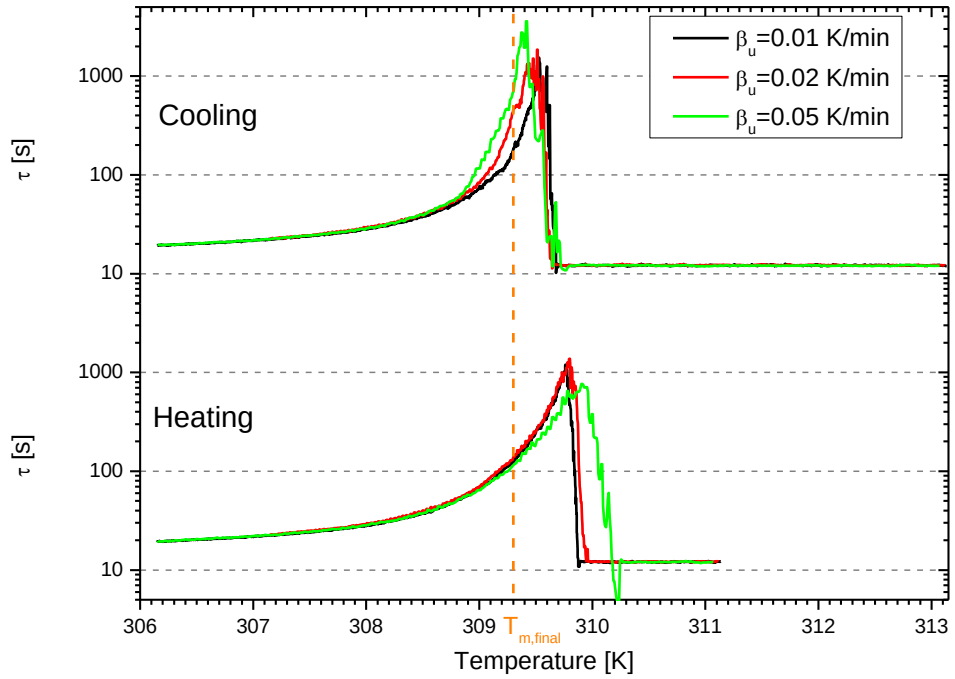

Figure 113: Relaxation time τ for a C20 sample with mass m=19.09 mg and purity of 99.0+%. Measurements were done with different heating and cooling rates β_u indicated in the legend. Top: Cooling part of the measurement; Bottom: Heating part of the measurement. The indicated final melting temperature $T_{m,final}$ corresponds to the one of low purity samples.

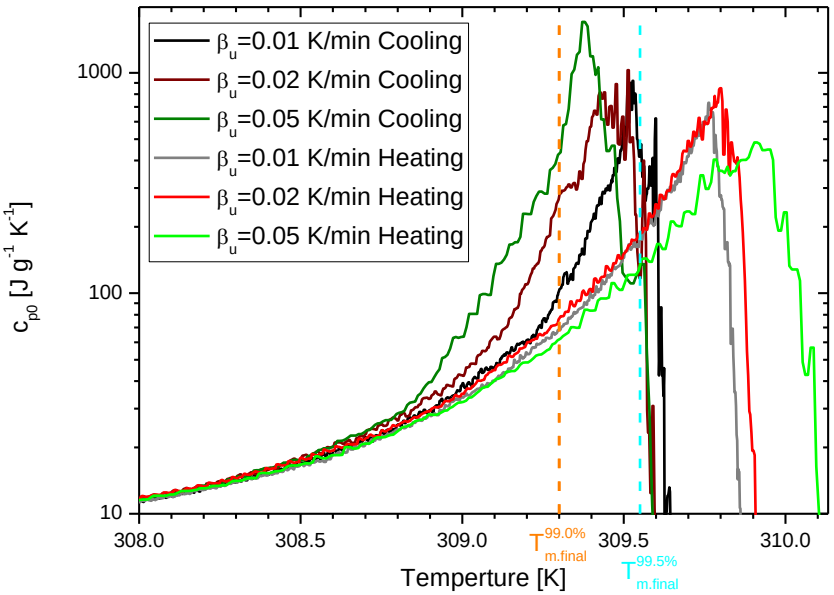

Figure 114: Comparison of the heating and cooling part for the quasi static apparent heat capacity c_{p0} of figure 112. Heating and cooling rates β_u are indicated in the legend. $T_{m,final}^{99.0\%}$ and $T_{m,final}^{99.5\%}$ correspond to the final melting temperatures of low and high purity samples respectively.

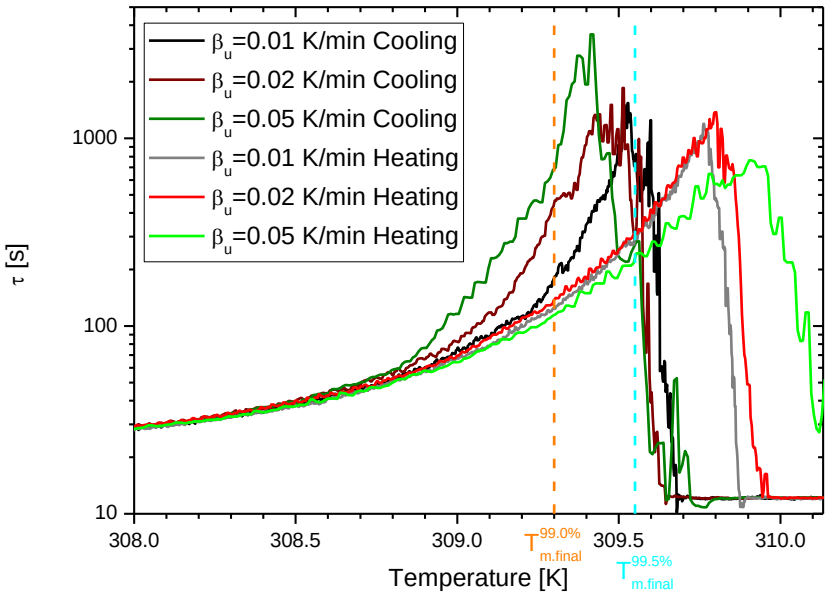

Figure 115: Comparison of the heating and cooling part for the relaxation times τ of Figure 113. Heating and cooling rates β_u are indicated in the legend. $T_{m,final}^{99.0\%}$ and $T_{m,final}^{99.5\%}$ correspond to the final melting temperatures of low and high purity samples respectively.

Another interesting behaviour is that for the measurements with heating rates $\beta_u = 0.01$ K/min and $\beta_u = 0.02$ K/min the data coincides until 309.8 K (see figure 114 and figure 115).

For a transition of first order one would expect faster kinetics the further one is away from the melting temperature. This on the other hand would result in shorter relaxing behaviour which is observable for the measurement with $\beta_u = 0.05$ K/min. The two other measurements on the other side suggest that the behaviour in the time domain are not of a kinetic origin but rather a static property dependent on temperature. This is comparable to what is found in the lattice structure at the transition (see section IV.4.2).

Starting temperature

N N-alkanes are known for having condis crystalline monolayers at surfaces to air or some metals [50] well above the melting temperature ($T_{m,ML} \approx T_m + 3\mathrm{K}$). So it is important to check if there is evidence for any memory effect emerging in melted C20 samples. To do so a series of experiments with different starting temperatures was carried out (see figure 116 for the temperature programs). The tests were realized in a single run, so that for each temperature program the DSC adjusted the temperature from 311.15 K to the respective starting temperature. The cooling and heating rate were set to $\beta_u = 0.05$ K/min in the rotator phase, the amplitude to a = 0.25 K and the pulse length range to $\Delta t_p = 40..60$s. To reduce the measuring time a higher cooling rat ($\beta_u = 1$ K/min) was used in the liquid phase (see figure 116).

In figure 117 the measured heat flux is shown as a function of the oven temperature. There is no direct difference detectable between the measurements with different starting temperatures. Similarly the evolution of the quasi-static apparent heat capacity and the relaxation times as a function of temperature does not depend on the choice of the starting temperature in the melt. (see figure 118 and figure 119 respectively). It follows that for starting temperatures exceeding 313.15 K, memory effects or extraordinary nucleation processes relating to the sample's thermal history cannot be observed. Nevertheless the nucleation in C20 is heterogeneous: the samples can only be undercooled very little [55]. The source can either be the above mentioned surface crystallisation or remaining dust particles which were not removed by the cleaning process.

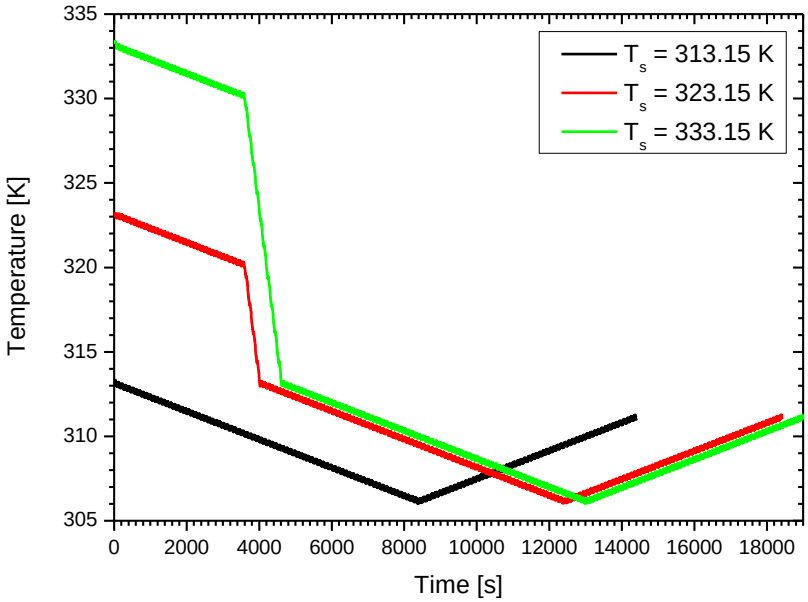

Figure 116: Temperature profile over time for TOPEM experiments to investigate the influence of the starting temperature.

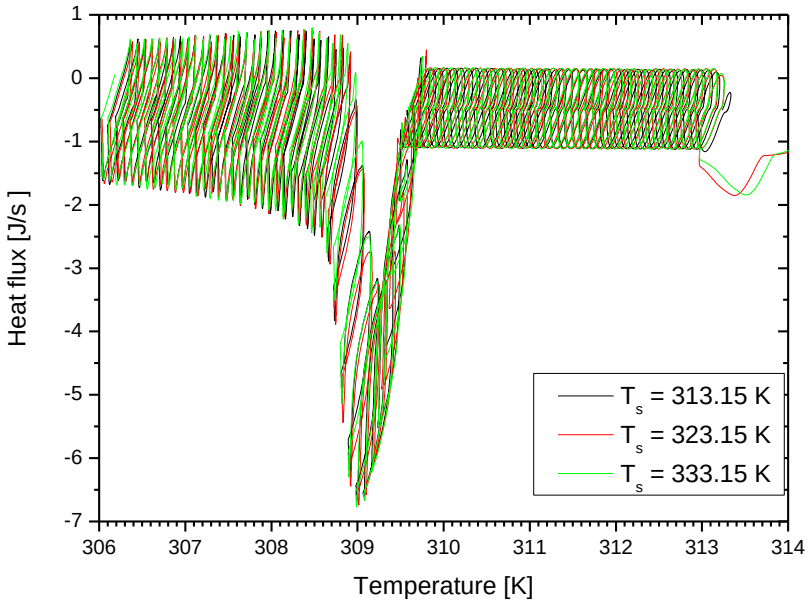

Figure 117: Heat flux for experiments starting at different temperatures for a C20 sample with mass m=19.09 mg and purity of 99.0+%. Starting temperatures are indicated in the legend.

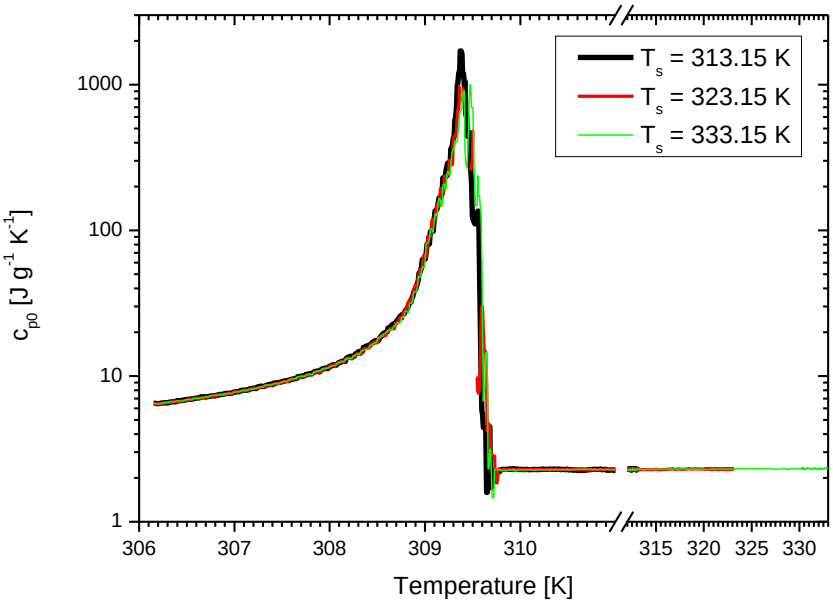

Figure 118: Quasi static apparent heat capacity c_{p0} for a C20 sample with mass m=19.09 mg and purity of 99.0+%. Measurements were done with different starting temperatures T_S indicated in the legend.

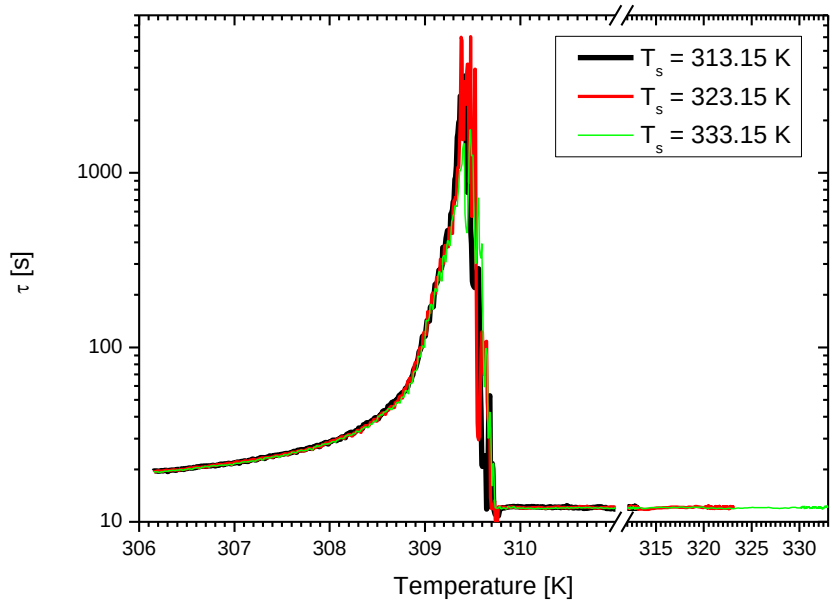

Figure 119: Relaxation times τ for a C20 sample with mass m=19.09 mg and purity of 99.0+%. Measurements were done with different starting temperatures T_S indicated in the legend.

Evaluation window

The evaluation window *w* describes the range in which the Z-transformation is applied to calculate the complex specific heat capacity. The suggestion by Mettler-Toledo is to take the triple of the duration of the longest pulse length to guarantee a large enough set of data points for the evaluation. We checked whether this criterion also applies to the measurements of C20 in its different phases. Figure 120 shows $c_{p0}(T)$ and $\tau(T)$ data obtained for a C20 sample with mass *m* = 9.23 mg and purity of 99.5+% by using different evaluation windows *w*. While the evaluations with *w* = 90 s (black squares in fig. 55) and *w* = 120 s (red pentagons in figure 120) yield data with important scattering those with *w* = 180 s (green triangles in figure 120)and *w* = 270 s (blue triangles in figure 120)) clearly show much more stable results. For the chosen pulse length range $\Delta t_p = 40..60$s, the evaluation window with width *w* = 180 s fulfils the above mentioned criterion. To further enhance the

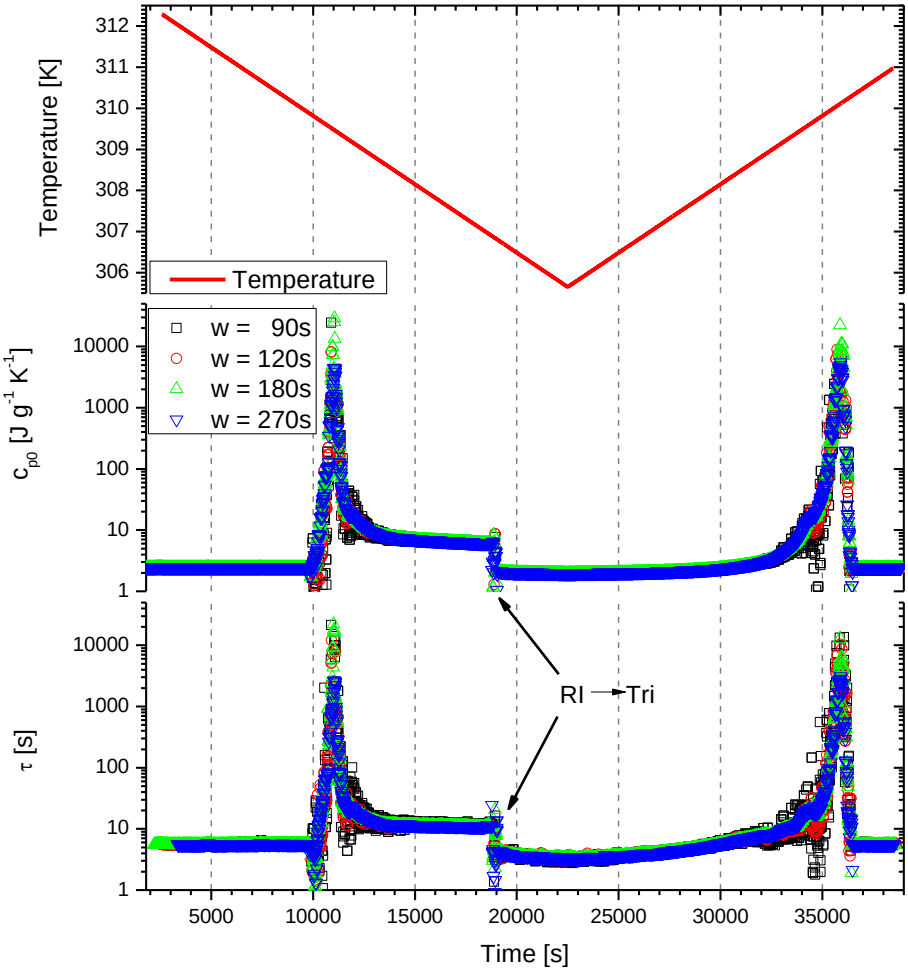

Figure 120: Reference temperature (top) quasit static apparent heat capacity (middle) and relaxation times (bottom) over time for a TOPEM measurement of a C20 sample with mass *m* = 9.23mg and purity of 99.5+%. The measurement was done with underlying cooling and heating rate of $\beta_u = 0.02$ K/min, an amplitude of a = 0.5 K and a pulse length of $\Delta t_p = 40..60s$. The values were calculated with different evaluation windows indicated in the legend in the Stare software by Mettler-Toledo.

stability of the results we chose the width $w = 180$ s for the evaluations in the present work.

Smoothing window

The last parameter under investigation is the width of the smoothing window. The smoothing algorithm which is implemented into the Stare software provided by Mettler-Toledo is applied after the calculation of the quasi-static specific heat capacity and before the Fourier transformation yielding the complex specific heat capacity. The suggestion by Mettler-Toledo is to use three-fourths of the width of the evaluation window. The question is whether smoothing conceals any effects.

In figure 121 and figure 122 show the temperature dependence of the quasi-static apparent heat capacity c_{p0} and the relaxation times τ respectively for different widths of the smoothing window. The TOPEM measurement was performed with a cooling and heating rate of $\beta_u = 0.02$ K/min, an amplitude of $a = 0.25$ K and a pulse length range $\Delta t_p = 40..60$ s. An evaluation window with a width of $w = 180$ s was chosen. Data scattering is practically independent of the width of the smoothing window at low temperatures in the rotator phase or in the melt. However, close to the phase transition, the broadening of the smoothing window slightly scales the data down and reduces the number of outliers. Nevertheless, as in the vicinity of a first order transition the outliers can result from fluctuations they are very useful for the detection of the process. For this reason the smoothing window will not be used.

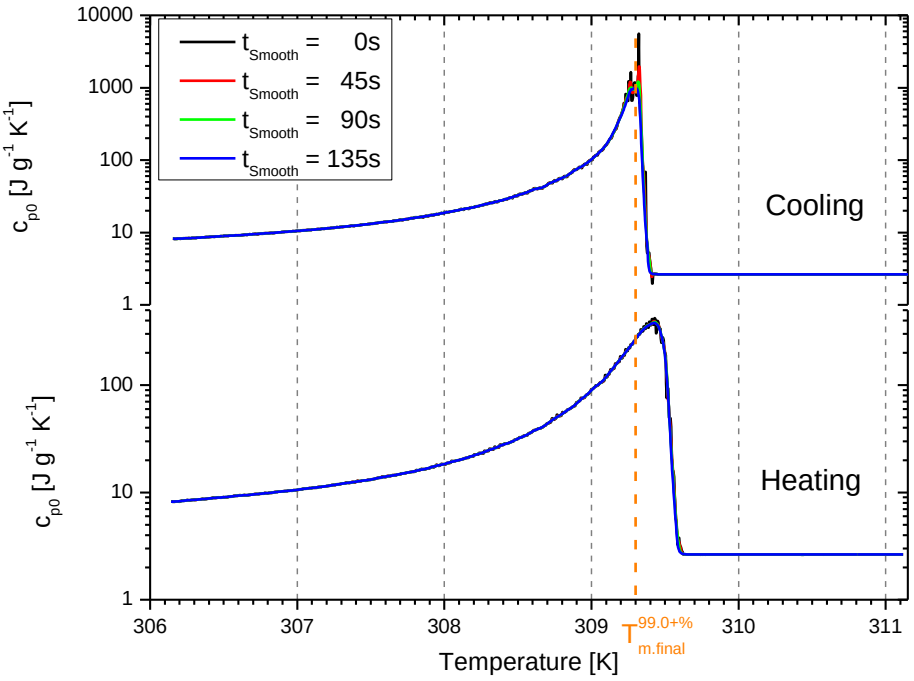

Figure 121: Quasi static apparent heat capacity c_{p0} for a C20 sample with mass m=8.5 mg and purity of 99.0+%. Evaluations were done with different smoothing windows t_{Smooth} indicated in the legend. Top: Cooling part of the measurement; Bottom: Heating part of the measurement. The indicated final melting temperature $T_{m,final}^{99.0+\%}$ corresponds to the one of low purity samples.

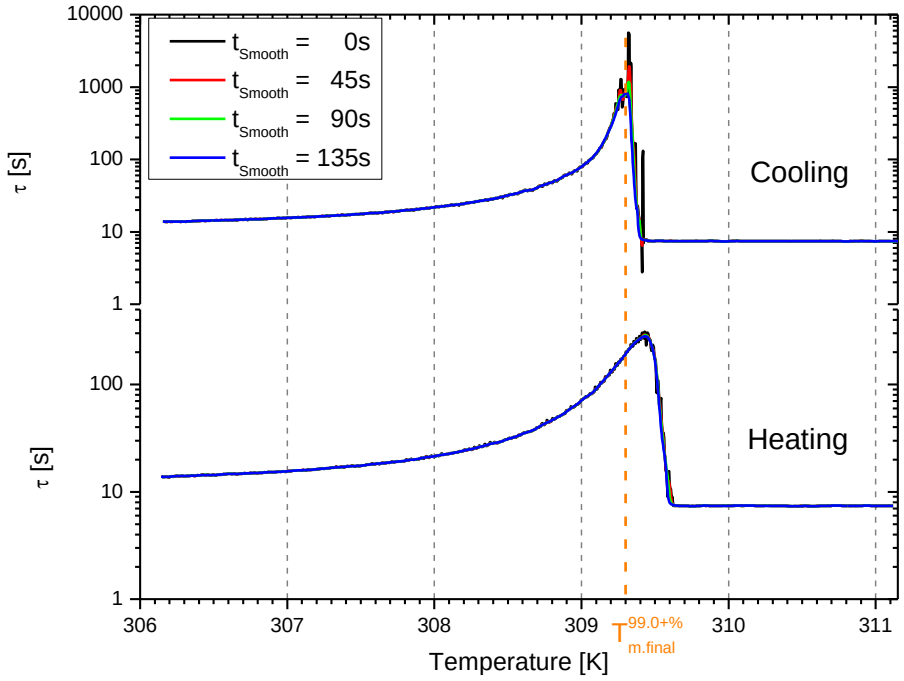

Figure 122: Relaxation times τ for a C20 sample with mass m=8.5 mg and purity of 99.0+%. Evaluations were done with different smoothing windows t_{Smooth} indicated in the legend. Top: Cooling part of the measurement; Bottom: Heating part of the measurement. The indicated final melting temperature $T_{m,final}^{99.0+\%}$ corresponds to the one of low purity samples.

Literature references

[1] A. Müller, Proceedings of the Royal Society of London. Series A **124**, 317 (1929).
[2] A. Müller, Proceedings of the Royal Society of London. Series A **138**, 514 (1932).
[3] A. Müller, Proceedings of the Royal Society of London. Series A, Mathematical and Physical Sciences **154**, 624 (1936).
[4] M. Anwar, J. T. Berryman, and T. Schilling, The Journal of Chemical Physics **141**, 124910 (2014).
[5] J. Pak and B. Wunderlich, Journal of Polymer Science Part B: Polymer Physics **38**, 2810 (2000).
[6] D. M. Small, *The Physical Chemistry of Lipids: From Alkanes to Phospholipids* (Plenum Press, 1986).
[7] E. Sirota, H. King Jr, D. Singer, and H. H. Shao, The Journal of Chemical Physics **98**, 5809 (1993).
[8] P. Espeau, L. Robles, D. Mondieig, Y. Haget, M. A. CuevasDiarte, and H. A. J. Oonk, J. Chim. Phys.-Chim. Biol. **93**, 1217 (1996).
[9] L. Robles, D. Mondieig, Y. Haget, and M. A. Cuevas-Diarte, J. Chim. Phys.-Chim. Biol. **95**, 92 (1998).
[10] M. Dirand, M. Bouroukba, A.-J. Briard, V. Chevallier, D. Petitjean, and J.-P. Corriou, The Journal of Chemical Thermodynamics **34**, 1255 (2002).
[11] A.-J. Briard, M. Bouroukba, D. Petitjean, N. Hubert, and M. Dirand, Journal of Chemical & Engineering Data **48**, 497 (2003).
[12] M. G. Broadhurst, J. Res. Natl. Bur. Stand. A **66**, 241 (1962).
[13] G. UNGAR, J. STEJNY, A. KELLER, I. BIDD, and M. C. WHITING, Science **229**, 386 (1985).
[14] G. Strobl, B. Ewen, E. Fischer, and W. Piesczek, The Journal of Chemical Physics **61**, 5257 (1974).
[15] B. Ewen, E. Fischer, W. Piesczek, and G. Strobl, The Journal of Chemical Physics **61**, 5265 (1974).
[16] B. Ewen, G. R. Strobl, and D. Richter, Faraday Discussions **69**, 19 (1980).
[17] E. Andrew, The Journal of Chemical Physics **18**, 607 (1950).
[18] R. G. SNYDER, M. MARONCELLI, S. P. QI, and H. L. STRAUSS, Science **214**, 188 (1981).
[19] M. Maroncelli, H. Strauss, and R. Snyder, The Journal of Chemical Physics **82**, 2811 (1985).
[20] J.-P. Ryckaert, I. R. McDonald, and M. L. Klein, Molecular Physics **67**, 957 (1989).
[21] I. Basson and E. C. Reynhardt, The Journal of Chemical Physics **93**, 3604 (1990).
[22] J. Pak, A. Boller, I. Moon, M. Pyda, and B. Wunderlich, Thermochimica Acta **357–358**, 259 (2000).
[23] M. Reading, D. Elliott, and V. Hill, Journal of thermal analysis and calorimetry **40**, 949 (1993).
[24] A. Wurm, M. Merzlyakov, and C. Schick, Journal of Thermal Analysis and Calorimetry **60**, 807 (2000).
[25] B. Wunderlich, A. Boller, I. Okazaki, K. Ishikiriyama, W. Chen, M. Pyda, J. Pak, I. Moon, and R. Androsch, Thermochimica Acta **330**, 21 (1999).

[26] A. Wurm, M. Merzlyakov, and C. Schick, Journal of Macromolecular Science-Physics **B38**, 693 (1999).
[27] C. Schick, A. Wurm, and A. Mohamed, Thermochimica Acta **392**, 303 (2002).
[28] B. Wunderlich, Thermochimica Acta **396**, 33 (2003).
[29] E. Sirota and A. Herhold, Polymer **41**, 8781 (2000).
[30] G. Ungar, The Journal of Physical Chemistry **87**, 689 (1983).
[31] J. Doucet, I. Denicolo, and A. Craievich, The Journal of Chemical Physics **75**, 1523 (1981).
[32] J. Doucet, I. Denicolo, A. Craievich, and A. Collet, The Journal of Chemical Physics **75**, 5125 (1981).
[33] I. Denicolo, A. F. Craievich, and J. Doucet, The Journal of Chemical Physics **80**, 6200 (1984).
[34] J. E. K. Schawe, T. Hütter, C. Heitz, I. Alig, and D. Lellinger, Thermochimica Acta **446**, 147 (2006).
[35] I. Fraga, S. Montserrat, and J. M. Hutchinson, Journal of thermal analysis and calorimetry **87**, 119 (2007).
[36] H. Höhne, Flammersheim, *Differential Scanning Calorimetry* (Springer, Berlin, 2003), 2nd edn., p.^pp. 115-146.
[37] M. Merzlyakov and C. Schick, Thermochimica Acta **380**, 5 (2001).
[38] Y. V. Mnyukh, Journal of Physics and Chemistry of Solids **24**, 631 (1963).
[39] P. S. Gill, S. R. Sauerbrunn, and M. Reading, Journal of Thermal Analysis **40**, 931 (1993).
[40] B. Wunderlich, *Thermal Analysis of Polymerci Materials* (Springer, Berlin, 2005), 1st edn.
[41] I. Okazaki and B. Wunderlich, Macromolecular Rapid Communications **18**, 313 (1997).
[42] R. Androsch and B. Wunderlich, Thermochimica Acta **333**, 27 (1999).
[43] J. Schawe, Thermochimica Acta **271**, 127 (1996).
[44] V. K. Pecharsky and P. Y. Zavalij, *Fundamentals of Powder Diffraction and Structural Characterization of Materials* (Springer, 2005).
[45] Y. Jin and B. Wunderlich, The Journal of Physical Chemistry **95**, 9000 (1991).
[46] I. Basson and E. C. Reynhardt, Journal of Chemical Physics **95**, 1215 (1991).
[47] J. Wettlaufer, Physical Review Letters **82**, 2516 (1999).
[48] Y. Imry and M. Wortis, Physical Review B **19**, 3580 (1979).
[49] B. Ocko *et al.*, Physical Review E **63**, 032602 (2001).
[50] A. Colussi, M. Hoffmann, and Y. Tang, Langmuir **16**, 5213 (2000).
[51] A. Schaerer, C. Busso, A. t. Smith, and L. Skinner, Journal of the American Chemical Society **77**, 2017 (1955).
[52] J. C. van Miltenburg, H. A. J. Oonk, and V. Metivaud, Journal of Chemical and Engineering Data **44**, 715 (1999).
[53] C. Rathgeber, L. Miró, L. F. Cabeza, and S. Hiebler, Thermochimica Acta **596**, 79 (2014).
[54] C. Castellón, E. Günther, H. Mehling, S. Hiebler, and L. Cabeza, International Journal of Energy Research **32**, 1258 (2008).
[55] H. Kraack, M. Deutsch, and E. Sirota, Macromolecules **33**, 6174 (2000).
[56] H. Kraack, E. B. Sirota, and M. Deutsch, Journal of Chemical Physics **112**, 6873 (2000).
[57] S. Weyer, A. Hensel, and C. Schick, Thermochimica Acta **305**, 267 (1997).
[58] S. Weyer, M. Merzlyakov, and C. Schick, Thermochimica Acta **377**, 85 (2001).
[59] A. Toda and M. Hikosaka, Thermochimica Acta **436**, 15 (2005).

[60] A. B. Herhold, H. E. King, and E. B. Sirota, Journal of Chemical Physics **116**, 9036 (2002).
[61] S. Craig, G. Hastie, K. Roberts, A. Gerson, J. Sherwood, and R. Tack, Journal of Materials Chemistry **8**, 859 (1998).
[62] A. Coelho, (Bruker AXS GmbH, Karlsruhe, Germany, 2007).
[63] H. Rietveld, Journal of Applied Crystallography **2**, 65 (1969).
[64] Crystallography Open Database (http://www.crystallography.net/), (Accessed March 2014).
[65] S. Nyburg and A. R. Gerson, Acta Crystallographica Section B: Structural Science **48**, 103 (1992).
[66] J. Teckoe and D. Bassett, Polymer **41**, 1953 (2000).
[67] B. Gruber, Acta Crystallographica Section A: Crystal Physics, Diffraction, Theoretical and General Crystallography **29**, 433 (1973).
[68] J. Crissman, E. Passaglia, R. Eby, and J. Colson, Journal of Applied Crystallography **3**, 194 (1970).
[69] P. Debye, Annalen der Physik **348**, 49 (1913).
[70] N. S. Murthy and H. Minor, Polymer **31**, 996 (1990).
[71] B. Goderis, H. Reynaers, R. Scherrenberg, V. B. Mathot, and M. H. Koch, Macromolecules **34**, 1779 (2001).
[72] R. Jimenez, J. K. Kruger, M. Prechtl, C. Grammes, and P. Alnot, Journal of Physics: Condensed Matter **6**, 10977 (1994).
[73] D. W. Noid, B. Sumpter, and B. Wunderlich, Macromolecules **23**, 664 (1990).
[74] A. Marx, J. Krüger, and H.-G. Unruh, Zeitschrift für Physik B Condensed Matter **75**, 101 (1989).
[75] R. Androsch and B. Wunderlich, Thermochimica Acta **364**, 181 (2000).
[76] T. Ozawa, Polymer **12**, 150 (1971).

Figure List

Table List